

15182

NATIONAL LIBRARY  
OTTAWA



BIBLIOTHÈQUE NATIONALE  
OTTAWA

NAME OF AUTHOR..... Bruce E. Ball.....  
 TITLE OF THESIS..... Pyrolytic Graphite Containing  
 Small Concentrations of  
 Transition Metals.....  
 UNIVERSITY..... of Alberta.....  
 DEGREE FOR WHICH THESIS WAS PRESENTED..... Ph.D.....  
 YEAR THIS DEGREE GRANTED..... 1973.....

Permission is hereby granted to THE NATIONAL LIBRARY  
 OF CANADA to microfilm this thesis and to lend or sell copies  
 of the film.

The author reserves other publication rights, and  
 neither the thesis nor extensive extracts from it may be  
 printed or otherwise reproduced without the author's  
 written permission.

(Signed)..... *B. Ball*.....

PERMANENT ADDRESS:

..... 5539-5 Ave. S.E.  
 ..... Calgary, Alberta  
 .....

DATED..... April 14, 1973

NL-91 (10-68)

THE UNIVERSITY OF ALBERTA

PYROLYTIC GRAPHITE CONTAINING  
SMALL CONCENTRATIONS OF TRANSITION METALS

by



BRUCE EVART BALL

A THESIS

SUBMITTED TO THE FACULTY OF GRADUATE STUDIES AND RESEARCH  
IN PARTIAL FULFILMENT OF THE REQUIREMENTS FOR THE DEGREE  
OF DOCTOR OF PHILOSOPHY IN METALLURGICAL ENGINEERING

DEPARTMENT OF MINING AND METALLURGY

EDMONTON, ALBERTA

SPRING, 1973

THE UNIVERSITY OF ALBERTA  
FACULTY OF GRADUATE STUDIES AND RESEARCH

The undersigned certify that they have read,  
and recommend to the Faculty of Graduate Studies and  
Research, for acceptance, a thesis entitled PYROLYTIC  
GRAPHITE CONTAINING SMALL CONCENTRATIONS OF TRANSITION  
METALS submitted by Bruce Evert Ball in partial fulfil-  
ment of the requirements for the degree of Doctor of  
Philosophy.

*Francis Pitore*  
.....  
Supervisor

*Michael A. Wayman*

*Samuel A. Bradford*

*Louise P. Pitt*  
.....

*A. J. Holman*  
.....

*Barclay*  
.....  
External Examiner

Date *October 4, 1972*  
.....

## ABSTRACT

Graphite alloys containing titanium, vanadium, manganese, and nickel were produced by pyrolytically decomposing propane and a metal-containing vapour onto a stationary graphite substrate. A deposition pressure less than 10 torr and a deposition temperature between 1500 and 2200°C were used in producing these alloys. The deposition kinetics of the alloy formation were examined by measuring the conductivity change of the alloy deposit with deposition time. Alloy formation was found to be linear with time under the deposition conditions employed.

The alloy density was measured using a sink float technique and crystallographic parameters were determined using X-ray diffraction. The microstructure of the alloys was examined by light microscopy, electron microscopy, electron diffraction, and by electron probe microanalyser. The mechanical properties of the alloys were examined by microhardness and bend testing. Some heat treating of the alloys was also conducted. A total of seventy-five deposits were investigated.

Titanium was found to enhance the pyrolytic deposition rate. The titanium containing alloys were found to be a two phase system down to the lowest concentration investigated (0.002 a/o Ti). The graphite phase was found to have

an enhanced density but smaller crystal size, than pure pyrolytic graphite. Titanium carbide particles, 2,000 Å in size, were preferentially aligned with their dense packed (111) planes parallel to the graphite basal planes. Evidence for dispersion hardening which reaches a maximum at 0.020 a/o titanium was found.

Vanadium increased the pyrolytic deposition rate to over four times that of pure pyrolytic graphite whereas nickel enhanced the rate by one and one half times. Manganese was found to have no effect. The alloys containing either vanadium or nickel were found to have an increased degree of graphitization with very little metal being incorporated into the alloy deposits. The enhancement of graphitization is significant in terms of codeposition being employed to perfect the crystallinity of graphite formed by the pyrolytic method.

In summary, the increased deposition rate, the enhanced graphitization, and the possibility of dispersion hardening are the most significant findings of this investigation. Furthermore, it appears that any solid solubility of transition metals in graphite is very low.

## ACKNOWLEDGEMENTS

I am indebted to Dr. F. H. Vitovec who first of all saw the need for the study and then spent much time discussing areas pertinent to it with me. His moral support and encouragement are greatly appreciated.

I would also like to thank the Department's technical staff; Mr. R. Scott, Mr. T. Forman, Mr. K. Hartung, and Mr. B. Snider, for their assistance in various aspects of the research program. Clerical assistance provided by Mrs. B. Hickey and Mrs. R. Mei is also appreciated. The construction of the deposition apparatus was in part done by Mr. G. Chaisson of Technical Services. Assistance on the electron microprobe from Mr. D. Tomlinson of the Geology Department is appreciated as is the assistance in conducting the propane analysis from Mr. J. Moser of the Department of Chemical and Petroleum Engineering.

Support for this research and myself was provided by the International Nickel Company of Canada, Limited, in the form of an INCO Graduate Research Fellowship. This support is greatly appreciated.

## TABLE OF CONTENTS

	Page
1. INTRODUCTION	1
1.1 Alloying Additions to Graphite	5
2. THE GRAPHITIC FORM OF CARBON	15
2.1 Graphite and its Crystal Lattice	15
2.2 Concept of Degree of Graphitization	16
3. EXPERIMENTAL PROGRAM	20
3.1 Alloy Production	20
3.2 Selection of Alloying Elements	21
3.3 Deposition Equipment	23
3.4 Methods of Deposit Evaluation	25
3.4.1 Deposition Kinetics	25
3.4.2 Chemical Composition	27
a. Titanium	27
b. Vanadium	28
c. Nickel	28
3.4.3 Density Measurement	28
3.4.4 Microstructure Examination	29
3.4.5 X-ray Structure	30
3.4.6 Bend Strength Evaluation	31
3.4.7 Deposit Microhardness	32
3.4.8 Distribution of Alloying Element	33
3.4.9 Stability of Alloying Element	33

	Page
4. EXPERIMENTAL RESULTS	34
4.1 Deposition Kinetics	34
4.1.1 Pyrolytic Graphite	34
4.1.2 Pyrolytic Graphite-Titanium Alloys	34
4.1.3 Pyrolytic Graphite-Vanadium Alloys	35
4.1.4 Pyrolytic Graphite-Nickel Alloys	36
4.2 Pyrolytic Graphite Deposition	36
4.2.1 Metallography of Pyrolytic Graphite	36
4.2.2 Property and Structure Variation of Pyrolytic Graphite	38
4.3 Pyrolytic Alloy Codeposition	39
4.3.1 Graphite-Titanium Alloy Codeposition	39
a. Metallography of Graphite- Titanium Alloy Codeposits	40
b. Properties and Structure of Graphite-Titanium Alloy Codeposits	40
c. Stability of Graphite-Titanium Alloy Codeposits	44
4.3.2 Graphite-Vanadium Alloy Codeposition	46
a. Metallography of Graphite- Vanadium Alloy Codeposits	46
b. Properties and Structure of Graphite-Vanadium Alloy Codeposits	47
4.3.3 Graphite-Manganese Codeposition	49



	Page
4.3.4 Graphite-Nickel Codeposition	49
a. Metallography of Graphite-Nickel Alloy Codeposits	50
b. Properties and Structure of Graphite-Nickel Alloy Codeposits	50
5. DISCUSSION	52
5.1 Evaluation of Pyrolytic Deposition	52
5.2 Discussion of Alloy Deposition Results	53
5.2.1 Graphite-Titanium Alloys	53
5.2.2 Graphite-Vanadium Alloys	59
5.2.3 Graphite-Manganese Alloys	60
5.2.4 Graphite-Nickel Alloys	61
5.3 Phase Relationships in Alloys	62
5.4 Engineering Significance of Alloys	65
5.4.1 Deposition Rate	65
5.4.2 Enhanced Graphitization	66
5.4.3 Second Phase Hardening	66
5.5 Summary	67
6. CONCLUSIONS	69
REFERENCES	71
TABLES	82
FIGURES	93
APPENDIX A	145
APPENDIX B	154

LIST OF TABLES

	Page
1. Analysis of Matheson Natural Grade Propane Used in Deposition Experiments	82
2. Pyrolytic Graphite Properties	83
3. Microhardness of Pyrolytic Graphite	84
4. Properties of Graphite-Titanium Alloys	85
5. Bend Strength Test Results for Sample #15PCTi	87
6. Properties of Heat Treated Titanium Alloy Codeposits	88
7. Chemical Analysis of Heat Treated Graphite-Titanium	89
8. Pyrolytic Carbon-Vanadium System Properties	90
9. Microhardness of Pyrolytic Graphite- Vanadium Alloys	91
10. Pyrolytic Graphite-Nickel System Properties	92

## LIST OF FIGURES

	Page
1. Speer RC4 Graphite.	93
2. Flow sheet for pyrolytic codeposition apparatus.	94
3. Pyrolytic codeposition equipment.	95
4. Graphite substrate design.	96
5. Conductance change of graphite deposit with time.	97
6. Growth rate of pyrolytic graphite as a function of deposition temperature and for a deposition pressure of $4.5 \pm 0.5$ torr.	98
7. Conductance of graphite-titanium alloy deposits formed at $1675 \pm 75^\circ\text{C}$ and $5 \pm 1$ torr.	99
8. Growth rate as a function of titanium concentration for alloys formed at $1675 \pm 75^\circ\text{C}$ and $5 \pm 1$ torr.	100
9. Effect of feed gas flow rate on the growth rate of pyrolytic graphite-vanadium alloys.	101
10. Conductance of graphite-nickel alloy deposits formed at $1600 \pm 40^\circ\text{C}$ and $6 \pm 0.5$ torr.	102
11. Substrate with top view of pyrolytic graphite deposit.	103
12. Singularly nucleated pyrolytic graphite.	104
13. Polynucleated pyrolytic graphite.	105
14. Deposition surface parallel to deposition substrate.	106
15. Apparent density of pyrolytic graphite as a function of deposition temperature.	107
16. Lattice constant, $C$ , as a function of deposition temperature for pyrolytic graphite formed at a pressure of $4.5 \pm 0.5$ torr.	108

	Page
17. Crystallite size, $L_c$ , as a function of deposition temperature.	109
18. Carbon titanium phase diagram.	110
19. Singularly nucleated alloy of pyrolytic graphite and 0.285 a/o titanium.	111
20. Singularly nucleated alloy of pyrolytic graphite and 0.002 a/o titanium.	112
21. Top view of basal plane growth cones in pyrolytic graphite-titanium alloys deposited at $1675 \pm 75^\circ\text{C}$ and $5 \pm 1$ torr.	113
22. Precipitate in pyrolytic graphite-0.012 a/o titanium alloy deposited at $1660 \pm 20^\circ\text{C}$ and 5 torr.	114
23. Pyrolytic graphite-0.285 a/o titanium alloy formed at $1625 \pm 25^\circ\text{C}$ and 4 torr.	115
24. Apparent density of alloy deposits as a function of titanium concentration.	116
25. Apparent density of alloy deposits as a function of titanium concentration.	117
26. Crystallite height, $L_c$ , as a function of composition.	118
27. Crystallite height, $L_c$ , as a function of titanium concentration.	119
28. Bend strength, $\sigma$ , as a function of composition for alloys formed at $1675 \pm 75^\circ\text{C}$ and $5 \pm 1$ torr.	120
29. Microhardness on planes perpendicular to basal planes for alloys formed at $1675 \pm 75^\circ\text{C}$ and $5 \pm 1$ torr.	121
30. Microhardness on planes perpendicular to basal planes for alloys formed at $1975 \pm 35^\circ\text{C}$ and $5.5 \pm 1.5$ torr.	122
31. Microhardness on basal planes for alloys formed at $1675 \pm 75^\circ\text{C}$ and $5 \pm 1$ torr.	123

	Page
32. Microhardness on basal planes for alloys formed at $1975 \pm 35^{\circ}\text{C}$ and $5.5 \pm 1.5$ torr.	124
33. Electron microprobe scan on planes perpendicular to basal planes of a pyrolytic graphite-0.036 a/o titanium alloy deposited at $1675 \pm 55^{\circ}\text{C}$ and 5 torr.	125
34. Electron microprobe scan on basal planes of a pyrolytic graphite-0.18 a/o titanium alloy deposited at $1650 \pm 20^{\circ}\text{C}$ and 5 torr.	126
35. (111) diffraction peak of titanium carbide.	127
36. Microhardness on planes perpendicular to basal planes for alloys formed at $1675 \pm 75^{\circ}\text{C}$ and heat treated at $1600 \pm 100^{\circ}\text{C}$ for 20 hours.	128
37. Microhardness on basal planes for alloys formed at $1675 \pm 75^{\circ}\text{C}$ and heat treated at $1600 \pm 100^{\circ}\text{C}$ .	129
38. Electron microprobe scan of titanium distribution.	130
39. Electron microprobe scan of titanium distribution.	131
40. Carbon-vanadium phase diagram.	132
41. Singularly nucleated pyrolytic graphite- $<0.001$ a/o vanadium alloy formed at $1800 \pm 20^{\circ}\text{C}$ and 5 torr.	133
42. Non-basal planes of a pyrolytic graphite- $<0.001$ a/o vanadium alloy formed at $1700 \pm 30^{\circ}\text{C}$ and 8+ torr.	134
43. Carbon plume growths on substrate formed at $1700 \pm 30^{\circ}\text{C}$ and 8+ torr.	135
44. Top view of basal planes of graphite-vanadium alloys.	136
45. Apparent density as a function of deposition temperature for pyrolytic graphite alloys containing $<0.001$ a/o vanadium and formed at 5 torr.	137

	Page
46. Singularly nucleated pyrolytic graphite- 0.003 a/o nickel alloy formed at $1620 \pm 20^\circ\text{C}$ and 6.5 torr.	138
47. Electron microprobe scan of nickel in a pyrolytic graphite alloy containing 0.003 a/o nickel.	139
48. Results taken from Marinkovic et al, Carbon <u>8</u> , 1970, p. 283.	140
49. The standard free energies of formation of carbides per mole of graphite.	141
50. Precipitate in pyrolytic graphite-titanium alloy with [110] zone planes parallel to graphite basal planes.	142
51. Semi-coherent interface between titanium carbide and graphite.	143
52. Properties of pyrolytic carbon-niobium alloys.	144

## 1. INTRODUCTION

The use of graphite as an engineering material is rapidly expanding. This is due in part to the properties inherent to graphite and in part to a better understanding, achieved through research, of the structure-property relations which has led to the development of graphites with improved engineering properties. Graphite has the ability to retain its strength to approximately 2500°C. In fact, its tensile strength at 1400°C can be 75 percent higher than at room temperature.<sup>1</sup> This strength retention plus a relatively high conductivity (in the vicinity of  $10^6$  (ohm-cm)<sup>-1</sup>)<sup>2</sup> are utilized in electrical applications such as electrodes and brushes. Good machinability plus an excellent resistance to thermal shock make graphite a desirable material for some machine components. A low neutron absorption cross-section makes graphite useful as a nuclear reactor moderator and structural material. Aerospace applications make use of graphite's anisotropy and high temperature stability. Hot pressing dies made from graphite make high density and high strength ceramics possible. These are only a few of the more recent uses that research and development have contributed to for graphite materials.

Factors which have restricted a more wide spread use of bulk graphite are its permeability, low ductility and relatively low strength. These limiting factors are caused by imperfections of the crystal lattice, the presence of voids, and the weak bonds between crystallographic layer planes. Before examining possible means of improving or altering graphite's properties, a review of the natural and man made forms of graphite is in order.

Natural graphite is found in various locations throughout the world and occurs as either single crystals or crystal aggregates, generally possessing a low degree of perfection. The primary source of industrial graphite is not these natural crystals but commercially made graphite which comes in two forms: that made by the Acheson Process, and that made by a pyrolytic decomposition and deposition process. The Acheson Process begins with a carbonaceous material such as petroleum coke, anthracite or lampblack. This material is calcinated and then crushed and screened to produce a range of particle sizes and a flour material. The particles and flour are mixed with coal tar pitch, formed into shapes, and then baked. This resulting "green" material is impregnated with pitch and subsequently graphitized at a temperature of approximately 3000°C. The final graphitized product has a very complex structure consisting of graphite particles held together



by a semi-graphitic binder. There are many shrinkage cracks and voids present in this product. Figure 1 shows a typical microstructure of an Acheson graphite.

Pyrolytically formed graphite is more dense and contains fewer voids than the Acheson graphite. Pyrolytic graphite also is highly anisotropic and displays a range of crystallinity. This form of graphite can be made by thermally decomposing a carbonaceous gas or liquid to give a graphite deposit on a heated substrate.

Graphite single crystals can be made using a pyrolytic process also, but it is more common to obtain single crystals by growing them in a molten metal or carbide bath.<sup>3</sup> The crystals so produced display structural defects such as twins. Thus, regardless of the source of the graphite, it contains a number of different defects which affect its properties.

Improvement in properties may be achieved by the following techniques:

1. Infiltration of graphite.

This involves introducing a second phase (metallic or nonmetallic) into the graphite pores resulting in

- (a) an increased density,
- (b) an increased load-bearing cross-section,
- (c) a second phase which may hinder crack propagation.

2. Graphite-metal combinations (cermets).

This is essentially a powdered graphite matrix held together by a metal binder. The binder is more ductile than the graphite and should:

- (a) form a strong bond between the graphite particles,
- (b) reduce stresses resulting from anisotropy,
- (c) serve as a hinderance to crack propagation.

3. Alloying of graphite.

Both solid solution and multiphase alloys are theoretically feasible. Such alloying may:

- (a) increase the degree of graphitization and perfection of the crystal lattice,
- (b) increase the crystallographic layer plane bonding strength,
- (c) increase the ductility,
- (d) conceivably result in segregation of solute atoms to boundaries causing relaxation in boundary areas and an increase of the bonding between particles,
- (e) reduce submicroscopic porosity,
- (f) possibly cause precipitation hardening or dispersion hardening.

The alloying behaviour has implications for the formation of both infiltrated graphite and cermets. It is for this reason that alloying will be investigated in this

thesis and that phase relationships will be of importance.

### 1.1 Alloying Additions to Graphite.

Natural graphite is known to contain a number of metallic impurities. The presence of these metallic elements in artificial graphites possibly promotes crystallization of the graphite as well as modifying other properties. In most cases, additions of metal to graphite have been investigated only at large metal concentrations. However, in recent years there has been an increasing interest in graphite-metal relationships for small metal concentrations. Studies of graphite-metal systems are more complex than metal-metal systems because graphite begins to sublime at approximately 2500°C and can only be melted above 100 atmospheres and 3800°C and, therefore, cannot be readily equilibrated in the liquid state.

There are, however, four methods of adding metals or compounds to graphite to facilitate graphite-metal phase studies. These methods are: powder blending and sintering, molten bath mixtures, graphite infiltration, and pyrolytic codeposition.

The cermet forming technique of powder blending and sintering results in a multi phase system--graphite with one or more phases bonding graphite particles together. Electrical brushes are commercially made by this process

to give brush material which is high in conductivity and wear resistance. Common bonding materials are copper, copper oxide and silver. Graphite electrodes for various uses can also be made in this manner. Other graphite base materials with iron and cobalt have been found to have improved mechanical properties over graphite.<sup>4</sup> No phase studies have been conducted with alloys produced using the technique of powder blending and sintering.

The method used to produce graphite single crystals in molten metal baths has, however, been employed in graphite-metal phase studies. Commonly, nickel or iron melts are used as these molten metals are capable of dissolving sufficient amounts of carbon for precipitation as graphite. Other melts such as tungsten, chromium, rhodium, molybdenum, zirconium carbide and titanium boride have also been used.<sup>5</sup> Austerman<sup>3</sup> reports that entrapment of the solvent can readily occur in graphite crystals grown from a melt and the degree of such entrapment varies directly with the crystal growth rate. Micrographs produced by Austerman show graphite cleavage planes decorated with iron and nickel beads. No information on the mechanical properties of the graphite so produced is available as this technique has been employed to produce highly crystallized but very small single crystals for electronic studies.

Using the method of growing crystals from solution,

Strong and Hanneman<sup>6</sup> were among the first investigators to suggest that there is any sort of measureable solid solubility of metallic elements in graphite. In their investigation of the nickel-carbon phase diagram, they employed an electron probe micro-analyser for chemical analysis of small graphite crystals frozen into a nickel matrix. They found that the distribution of nickel was uniform throughout each graphite crystal. The temperature at which the graphite crystals were grown ranged between 1350°C and 1510°C. Pressures of 1 atmosphere and 26 or 54 kilobars were employed. The concentration of nickel possibly corresponding to the solubility limit in the graphite phase was found to be  $0.3 \pm 0.1$  atomic percent (a/o) nickel. The graphite crystals were observed in an electron microscope and were found to be uniform to a resolution of at least 100 Å. Pressure effects on solubility could not be detected within experimental error. Carbide formation and high melting temperatures have restricted further use of this technique.

The graphite infiltration technique has been used to form mixtures and alloys between graphite and other materials viz. elements, compounds, and radicals. Infiltration can usually be achieved by exposing graphite to the appropriate medium (either liquid or gas) and allowing the reactant material to diffuse into the graphite. In some

cases a catalyst has been found necessary to obtain any infiltration. Using the infiltration technique, a wide range of crystal compounds called intercalation or lamellar compounds have been formed with graphite. Intercalation compounds contain an element or compound in the interstitial space in the graphite lattice while the basic lattice structure of the graphite is preserved. Compounds are formed between graphite and one or more of the following chemical forms:

bisulphates	halides
nitrates	metal oxides
perchlorates	metal sulphides
arsenates	metal amides
halogens	alkali metals
phosphates	

Not all derivatives of the above form intercalation compounds as it is necessary for a transfer of electrons between the graphite and the reactant to occur before a compound is formed.<sup>7,8</sup> An intercalation compound can exist in several concentration stages which differ in the number of carbon layers alternating in a periodic sequence with single layers of reactant. A large number of these compounds are stable only in the presence of excess reactant. A considerable amount of work has been done with these systems; primarily to determine the electronic behavior of

the intercalation compounds.<sup>7,9,10,11</sup>

When the intercalation compound is heated to drive out the reactant, an equilibrium concentration of the reactant remains. The system achieved in this manner is called a residual compound, although this is probably a misnomer as the compound aspect no longer exists. The reactant is probably trapped at crystal defects in the graphite.<sup>7</sup>

The infiltration-diffusion technique was employed by Lowell to determine the extent of boron solid solution in graphite.<sup>12</sup> Natural graphite crystals were heat treated in a boron atmosphere between 1800°C and 2500°C. Analysis by X-rays of the resultant graphite showed a maximum solubility of 2.35 a/o at an eutectic temperature of 2350°C. The solid solution was shown to be substitutional. Enhancement of strength, density and crystallinity over ordinary graphite have been achieved by the formation of graphite-boron materials.<sup>13,14</sup>

Fitzer and Kegel<sup>15</sup> also employed infiltration (or diffusion) to determine vanadium solubility in graphite. An electron probe microanalyzer was used to study glassy carbon and graphite samples upon which vanadium carbide had been melted. They found that between 2650°C and 3000°C, the solubility of vanadium in well ordered graphite

is  $0.088 \pm 0.007$  a/o vanadium. Vanadium also enhanced the crystallinity of the graphite.

The technique of pyrolytically codepositing graphite and an element or compound has become prominent in the last twenty years. Originally, codeposition was used to enhance the properties of pyrolytic graphite used as a protective coating material<sup>16</sup> but it can now be used to form free standing alloys. That is, it is no longer necessary to retain a back up substrate or skeleton frame for the final graphite form.

Codeposition usually involves the thermal decomposition of two gas phases or, alternatively, the thermal decomposition of a single gas phase over an appropriate substrate, to give the desired product. This technique has been the basis of forming the alloys described in some patents<sup>17,18</sup> and alloy studies.<sup>19-25</sup>

Most of these studies were concerned with the strong carbide-forming transition metals and their effects on graphite strength and oxidation resistance. This work has been oriented towards heat shielding and nozzle materials for rocketry applications.<sup>19,20</sup> Other researchers<sup>21-25</sup> have employed the codeposition technique to improve the crystallinity of the graphite formed by pyrolysis. In most of the aforementioned work, the metal additive concentration has been greater than one weight percent. This



often results in a two phase system: a carbide and graphite. Generally, it has been found that the carbide is uniformly distributed throughout the graphite matrix.<sup>24</sup>

There have also been some studies using the pyrolytic codeposition method to study solid solubility in graphite. By far the largest number of these studies has been on the boron-carbon system. Katz and Gazzara<sup>13</sup> studied graphite-boron deposits by light microscopy, X-ray diffraction, and flexural strength measurements. They proposed that on the basis of all available evidence, the solubility limit of boron in graphite lies between 0.44 and 1.1 a/o boron. Structural changes observed at higher concentrations were explained by a coherent/noncoherent boron carbide deposition mechanism. Marinkovic et al<sup>26</sup> evaluated deposits of graphite and boron formed at 1400, 1500 and 1600°C. Deposits were evaluated by X-ray diffraction, oxidation behavior, density and microscopy. They concluded that boron can occupy both substitutional and interstitial positions in the graphite lattice. The limit of boron solubility at the temperatures previously cited was thought to be in the vicinity of 1 percent. The bend strength of the alloys was found to be a maximum of 23 KSI compared to 15 KSI for pyrolytic graphite.<sup>13</sup> The oxidation rate of the alloys was found to be lower than that of graphite and the density greater.<sup>26</sup>

The silicon-carbon system has also been investigated by the pyrolytic codeposition technique. At silicon concentrations of 0.006 to 0.30 a/o, silicon carbide particles having a dimension of approximately  $1000 \text{ \AA}$  have been identified.<sup>27</sup> Yajima and Hirai<sup>28,29,30</sup> produced siliconated pyrolytic graphite alloys containing 0.001 to 1.8 a/o silicon over the temperature range of 1400 to 2000°C. Based on data from X-ray analysis, surface oxidation, electron diffraction and electron microscopy, they concluded that the major portion of the silicon is present as  $\beta$ -SiC which is uniformly distributed throughout the graphite.<sup>29</sup> No evidence of the carbide was found in samples of low silicon concentration (below approximately 0.015 a/o silicon).

Marinkovic et al<sup>31</sup> analyzed carbon-silicon deposits formed between 1340 and 1630°C in the same manner as they evaluated the carbon-boron system.<sup>26</sup> They found that silicon enters the graphite lattice only in the substitutional mode and the limit of this solid solution is 0.065 - 0.085 a/o silicon. Silicon above this concentration forms  $\beta$ -SiC. In addition, they found<sup>32</sup> that with a silicon concentration of up to 0.085 a/o, the microhardness of the deposit was unaffected but at higher silicon concentrations and higher deposition temperatures, areas could be found where the hardness corresponded to that of silicon carbide.

Marinkovic et al<sup>33</sup> have also applied their vapor codeposition technique<sup>26,31</sup> to the uranium-carbon system. Uranium was found to be nonuniformly distributed throughout the deposit. No solid solubility was detected. Alloys containing less than 0.015 a/o uranium were not studied. The presence of uranium was found to promote crystallization of the graphite.

Other studies which are of significance in phase relationships and thus in property development, are those concerning the distribution of impurities in graphite. Both natural and commercial graphites contain impurities such as sulphur derivatives, pure metals or metal compounds as well as boron and silicon and their compounds.<sup>34</sup> The distribution of these impurities in graphite electrodes has been examined using radiography, ash patterns and sulphur prints.<sup>35</sup> This distribution was found to be nonuniform with clustering in the interstices of coke grains. The release energies of some metallic impurities from graphite were studied by George.<sup>36</sup> For the metallic elements calcium, barium, strontium, and aluminum, the release energies were found to be greater than the known vaporization energies of the same atoms from their parent metals. These energies, however, are lower than the release energy for carbon atoms from graphite. The alkali metals are known intercalation compound formers and it appears that bonding

in such compounds is reasonably strong. Aluminum is not known to form an intercalation compound and thus its high release energy could indicate strong metal-carbon bonds being formed in a possible solid solution of aluminum in graphite.

In summary, the preceding has shown that some work has been done on phase relationships with graphite. Most of the published data deals with compound formation, two-phase studies (graphite plus a carbide), and solid solubility of boron and silicon. The two reported metal solid solubilities in graphite of 0.088 a/o vanadium and 0.3 a/o nickel are large enough to be of commercial manufacturing importance. These reported solubilities are of even more significance when the solid solution effects of boron and silicon are examined. Such solid solution alloys display higher flexural strength<sup>13</sup>, better erosion resistance<sup>20</sup>, and better oxidation resistance<sup>26</sup> than pure graphite. This leads to the possibility that transition metals might also enhance the properties of graphite. It is, therefore, of interest to extend the knowledge of transition metal-graphite systems and associated property changes particularly at small metal concentrations.

## 2. THE GRAPHITIC FORM OF CARBON

### 2.1 Graphite and its Crystal Lattice.

Graphite has been found to exist in two crystal structures. The hexagonal form is the normal structure, but a rhombohedral structure has been identified in severely cold-worked graphite.<sup>38</sup> This rhombohedral structure readily transforms to hexagonal graphite upon heat treatment.

In graphite, carbon is  $sp_2$  hybridized. The electronic configuration of the carbon atoms is  $1s^2 sp_2^1 sp_2^1 sp_2^1 p^1$ . Sigma bonding between the  $sp_2$  hybrid orbitals results in a hexagonal planar network of covalently bonded carbon atoms. The remaining electron in the unhybridized p orbital is also available for bonding. As this orbital is at right angles to the planar net, these planar networks are bonded together by the formation of van der Waals type pi bonds between the p orbitals. The result is a highly anisotropic, layered structure.

Within the layer planes, the carbon-carbon distance is  $1.415 \text{ \AA}$ , while the distance between layer planes is  $3.354 \text{ \AA}$ . The unit cell is hexagonal with a c dimension of  $6.708 \text{ \AA}$  and an a parameter of  $1.415 \text{ \AA}$ . The theoretical density is  $2.265 \text{ gm/cc}$ .

## 2.2 Concept of Degree of Graphitization.

Carbon is an extraordinary element in that it exists in a number of metastable forms under standard conditions. Graphite is the stable form of carbon. Chars and soots are amorphous solids displaying various degrees of crystalline properties. Other carbons vary in crystallinity from amorphous to crystalline graphite. Metastable diamond is a highly crystalline carbon solid. This ability to exist in various states of crystallinity has resulted in terminology confusion, particularly between the carbons and graphite. Graphite is the material with the hexagonal lattice discussed previously. Most materials that are called graphite are actually carbons which exhibit a crystallinity approaching that of graphite. In fact, true graphite is a rare material. However, in this text and as is commonly accepted, we shall refer to graphite as any carbon material having a  $c$  lattice spacing between  $6.71 \text{ \AA}$  and  $6.90 \text{ \AA}$ .

With an increase in the lattice parameter of graphite comes a decrease in the bond strength which is almost certain to have an effect on alloying behavior. Thus the degree of graphitization (crystallinity) and the actual graphitization process is fundamentally different from recrystallization in metals since in graphite the nucleation and growth of new perfect crystals does not generally occur

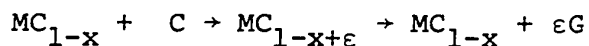
below the melting temperature. Fischbach<sup>39</sup> discusses graphitization in terms of a progressive improvement in an initially very defective structure. Thus the existence of a layer plane structure and the concentration and distribution of defects in the original structure are of importance.

The structure of disordered carbons is readily studied by X-rays. X-ray examination of a poorly crystallized graphite shows the presence of  $(00l)$  peaks and  $(hko)$  peaks. No three dimensional  $(hkl)$  peaks appear. The peaks that are present are quite broad and, in such cases, the lattice spacing,  $c$ , is larger than that of true graphite. The size of the semi-crystallized regions, called crystallites, can be estimated from Scherrer's line broadening formula.<sup>40,41</sup> At a higher degree of graphitization (crystallization), X-ray peaks sharpen and three-dimensional ordering peaks appear. A model in which poorly crystallized graphites are called turbostratic carbons was proposed by Warren.<sup>42</sup> The turbostratic term was coined to cover the manner in which the layer planes are displaced relative to each other by small translations or rotations about the  $c$  axis of the layered region.

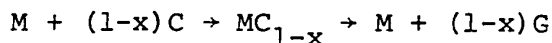
There has been a considerable number of studies<sup>39,43,44</sup> on the graphitization process and how it is affected by heat treatment, pressure application, plastic deformation and catalyst addition. To graphitize, a temperature greater

than 2000°C is generally required (although carbons formed at temperatures as low as 1500°C by the pyrolytic method do display some crystallinity). High temperature plastic deformation<sup>45</sup> and high pressures are found to be effective in increasing the rate and the degree of graphitization.

Enhancement of the rate and degree of graphitization by the use of metals as catalysts is important in phase studies of graphite-metal systems. Schwartz and Bokros<sup>24,25</sup> studied the catalytic effect of titanium on pyrolytic graphite by codepositing titanium and graphite. They found 5 to 7 weight percent titanium was necessary to cause catalysis. Fitzer and Kegel<sup>15</sup> proposed a mechanism for the catalytic effect of metals on graphite. They felt that the reaction proceeded via one of the following paths as the metal diffused through the carbon:



or



Derbyshire et al<sup>46</sup> experimented with graphite films deposited on nickel and found that the above diffusion-precipitation model explained the observed enhanced graphitization.

In a study of the formation of pyrolytic carbon on metal substrates between 870 and 1030°C,<sup>23</sup> an enhancement of



deposition and graphitization was found. The metals used were iron and nickel and the aforementioned 'diffusion-carbide mechanism was employed to explain the enhanced graphitization. In a similar study at 1000°C,<sup>47</sup> carbon films showed an increasing crystallinity with the order of the following metal substrates: molybdenum, tungsten, platinum, and tantalum. In yet another study,<sup>48</sup> metals were assumed responsible for promoting graphitization of artificial resins between 1400 and 2300°C. Thus in a study of metal-graphite phase relations, the concept of catalyzed graphitization is important as most graphites are actually carbons which display some graphitic character and the presence of metal atoms affects this degree of graphitization.

### 3. EXPERIMENTAL PROGRAM

The experimental program of this study concerns the production of graphite-metal alloys, and the evaluation of their structure and properties.

#### 3.1 Alloy Production.

Alloys were formed by the pyrolytic codeposition technique. This method was selected in preference to the liquid metal-graphite methods as it was felt that melt techniques could involve extremely high pressures which may significantly affect any possible solid solubility.<sup>49</sup> This was substantiated by Walker and Imperial,<sup>50</sup> who concluded that graphite crystals grown in an iron melt are subjected to pressures in the order of 100 Kg/cm<sup>2</sup>. With melt techniques, there is also the problem of wettability of graphite by molten metals.<sup>4</sup>

Pyrolytic deposition can be achieved either from a liquid phase or a gaseous phase. Gas phase deposition, which is considerably better documented,<sup>51-61</sup> was selected to minimize the amount of necessary work on pure pyrolytic carbon. Pyrolytic deposition can be done on a fluidized bed substrate or on a stationary substrate.<sup>62</sup> A stationary substrate was selected for this experimental program. Although a variety of carbon source gases can be employed,

propane was chosen as it is reported to have a high deposition rate<sup>20</sup> relative to other readily available gases. The high deposition rate was required to minimize alloy formation time which was in excess of three hours. An analysis of the Matheson Natural Grade propane used in the deposition experiments is given in Table 1. To achieve a carbon deposit that resembled graphite according to the earlier stated limits, a deposition temperature greater than 1500°C and a deposition pressure less than 10 torr were generally employed.

Two series of deposition experiments were run: one series was straight graphite deposition and the other a graphite-metal codeposition. Pure graphite was formed as it was felt necessary to characterize graphite deposited with the equipment design employed and also to form a comparison base from which alloy deposits could be evaluated.

### 3.2 Selection of Alloying Elements.

The choice of metals that could be employed was limited by the following considerations:

1. The vapor pressure of the metal in the graphite must be less than the deposition pressure at the employed deposition temperature. That is, the product of the equilibrium vapor pressure of the metal times its activity must be less than the existing vapor pressure

of the codeposited metal.

2. A volatile compound which would be economically feasible to use had to exist for the metal to give the required metal vapor. Furthermore, this compound must be thermally unstable at the deposition temperature involved. The compound should also contain no oxygen, nitrogen or other elements which might interfere in such a manner as to give an unwanted phase.
3. The selection of metals employed should be such that a general indication of phase and property trends for transition metals might be achieved.

Not all of the above criteria could be met in the selection of metals and metal compounds. Top priority was given to Condition Three and the resultant metal choices were: titanium, vanadium, manganese, and nickel. These metals are all from the fourth row of the periodic table and should indicate any trend related to the increasing atomic number. Titanium and vanadium are strong carbide formers. Manganese forms a variety of metastable carbides and nickel possibly forms only a very unstable carbide,  $\text{Ni}_3\text{C}$ . Solubilities of 0.088 a/o for vanadium in graphite<sup>15</sup> and 0.3 a/o for nickel in graphite<sup>6</sup> have been reported. No solubility data for titanium and manganese in graphite is available.

Titanium tetrachloride, vanadium tetrachloride, methylcyclopentadienyl manganese tricarbonyl, and nickel carbonyl were the chemical compounds selected for the codeposition experiments.

### 3.3 Deposition Equipment.

Figure 2 is a schematic representation of the equipment which was designed, constructed, and employed in the pyrolytic codeposition experiments. Figure 3 is a photograph of this equipment. In essence, the equipment consisted of a feed gas train, a deposition chamber in which an electric resistance heated substrate was located, and an exhaust gas train.

The feed gas train is the equipment between the propane source (A) and the inlet orifice (H). Here, the pressure was maintained at approximately 760 mm Hg by a low pressure regulator (B). The temperature of the water bath (E) could be varied to control the vapor pressure of the metal compound and thus the pressure of the propane. The inlet orifice (H) controlled the flow rate of the gases entering the deposition chamber.

The pressure in the deposition chamber and the exhaust gas train was kept at 10 torr or less. The deposition chamber was constructed from a Balzer's stainless steel vacuum cross-piece which was immersed in a water bath. At

right angles to the gas stream in the chamber was a graphite substrate whose approximate dimensions are given in Figure 4. The substrate was made from Speer RC4 graphite (Fig. 1) and was designed such that thermal gradients would be minimized. The design is given in Figure 4, where it is shown that the actual deposition surface was cut at different lengths on opposite sides of the substrate. Only alloy deposits formed in the centre region of the substrate were used for examination.

The temperature of the substrate was monitored through a quartz glass window by a Latronics Infrared Pyrometer (L). In addition to temperature monitoring by the pyrometer, a stainless steel sheathed, chromel-alumel thermocouple was inserted into the deposition chamber to within 20 mm of the deposition substrate. On some occasions, despite a protective shutter covering the sight glass, the glass became coated with soot and the thermocouple had to be used to maintain a constant substrate temperature. This increased the error in temperature control which is discussed in Appendix A. A Hobart-Electric-Motor-Driven welding generator capable of producing 36 kilowatts of d.c. power was used as a power source for the electrical resistance heated substrate. Controls on the welder were quite coarse and only a temperature tolerance of  $\pm 50^{\circ}\text{C}$  could be achieved in most deposition experiments.

In the exhaust gas stream, a water cooled condensing tower (J) was used to condense any volatiles passing from the deposition chamber. In addition, the condensing tower was packed with glass wool which acted as a solids filter for any gas-born soot particles. A sodium hydroxide solution (M) was used as a chlorine gas scrubber in the titanium and vanadium codeposition experiments. This was done to protect the vacuum pump from the chlorine gas generated by the decomposing chlorides.

### 3.4 Methods of Deposit Evaluation.

#### 3.4.1 Deposition Kinetics

Information on the variation of the deposition rate as a function of time or stage of deposition was obtained by measuring the electrical resistance change of the substrate and deposit.<sup>63</sup> In a first approximation, it was assumed that the deposition is uniform over the test length and that prolonged heating of the deposit has no effect on its electrical resistance. Measurements indicating the order of the deposition and whether the kinetics of the reaction changed as deposition progressed were then obtained by considering the following development.

It was assumed that a power relation exists between the total weight of the deposit and time, thus

$$W^n = Ct \quad (1)$$

where  $W$  = weight of the deposit

$C$  = a constant

$t$  = deposition time

$n$  = weight exponent

The following symbols are further defined:

$\ell, w, s$  = length, width and thickness of deposit

$\rho$  = resistivity of deposit

$d$  = density of deposit

$R_D$  = resistance of deposit

$R_S$  = resistance of substrate

$R_T$  = resistance of substrate plus deposit

Now,

$$W = \ell w s d \quad (2)$$

and

$$R_D = (\ell \rho) / (w s) \quad (3)$$

hence

$$W = (\rho \ell^2 d) / R_D = C_2 / R_D .$$

Substituting (3) in (1) gives

$$W^n = R_D^{-n} C_3 = C_1 t$$

where  $C_3 = C_2^n$ .

Further simplifying gives

$$(1/R_D)^n = C_4 t = (1/R_T - 1/R_S)^n$$

where  $C_4 = C_1 / C_3$ .



The effect of changing deposition surface condition was thus obtained by measuring the resistance of the substrate plus deposit and plotting the changing conductance of the substrate plus deposit on a logarithmic scale against time; the slope of this plot being the weight exponent.

#### 3.4.2 Chemical Composition

The chemical composition of the deposit was determined by using different techniques for different alloy deposits. Only manganese concentrations were determined by a commercial laboratory. In all other cases, approximately 100 milligrams of the powdered alloy deposit was placed in a platinum crucible and ashed at 750°C in air. From here, the treatment for different metals varied.

##### a. Titanium

The spectrophotometric method outlined by Weessler<sup>64</sup> was approximately followed to determine titanium concentrations as low as 20 ppm by weight. Approximately 50 mg of ammonium sulphate and 5 cc of concentrated sulphuric acid were added to the ashed graphite. This mixture was gently heated for one hour to dissolve all oxide matter. Five millilitres of 70% perchloric acid was then added and the total solution diluted to 25 cc. To 5 cc of this solution were added two drops of 30% hydrogen peroxide and

the intensity of the solution measured at a wavelength of 410 m $\mu$  in a spectrophotometer. The results were compared against a calibration curve prepared as outlined by Weissler.

b. Vanadium

The 3,3'-dimethylnaphthidine colorimetric method as outlined in ASTM specifications C560, Chemical Analysis of Carbon and Graphite,<sup>65</sup> was followed. However, only approximately 10 mg of ash was used instead of the specified 50 mg. The photometric measurements were done at a wavelength of 550 m $\mu$  and calibration curves were prepared as specified in the standard.

c. Nickel

Nickel analysis was done by dissolving the ashed graphite in 2 ml of 1:1 HNO<sub>3</sub>. This solution was diluted to 10 ml and the nickel content determined by atomic absorption spectrometry. Analysis<sup>66</sup> was done at 2,320 Å on a Perkin Elmer Model 290B atomic absorption spectrometer. Standards were prepared from Fisher Certified Atomic Absorption Standard for Nickel.

### 3.4.3 Density Measurements

The apparent density of the deposit was measured by the sink-float technique. A mixture of carbon tetrachloride and tetrabromoethane or carbon tetrachloride and methanol was used. A piece of the deposit was allowed to remain in

the liquid for 45 minutes before the final balance was made in order to standardize penetration of the liquid into the graphite's pores.<sup>67</sup>

#### 3.4.4 Microstructure Examination

The microstructures of the deposits were studied both by light and electron microscopy. For light microscopy, samples were prepared by cutting sections of the deposit plus substrate from the parent substrate and mounting the resulting section in bakelite. As different alloy deposits exhibited different degrees of ease of polishing, a variety of standard metallographic polishing techniques had to be employed to achieve a satisfactory polished surface. The specimen was generally observed under polarized light to obtain contrast between different structures.

Samples for the electron microscope were prepared by two different methods. One method was to glue acetate tape to the deposit, allow it to dry and then peel off the tape along with some of the deposit. The acetate tape was subsequently dissolved in acetone to leave behind the thin specimens peeled from the deposit. The other method was to grind the deposit until pieces were thin enough to be transparent to electrons. Due to the anisotropy of graphite, all specimens formed in the preceding two ways were basal plane specimens and no non-basal plane samples were examined.

A Hitachi HU11 microscope was used in the investigations and an accelerating voltage of 75 KV was found to be the most useful for examining the graphite. Some electron diffraction was also done on the microscope.

#### 3.4.5 X-ray Structure

The structure of the deposit was examined using both an X-ray diffractometer and a Debye Scherrer camera. In most cases copper radiation was used; however, chromium radiation was also used to examine those deposits which contained vanadium in order to avoid the problem of excess absorption of copper radiation by vanadium.<sup>68</sup> Diffractometry was done on a Philips model PW1380 horizontal goniometer.

The lattice parameter,  $c$ , was obtained wherever possible from the (004) peak of a powdered sample obtained by filing the deposit. If the deposit was too thin to be powdered, a solid piece of the deposit was analyzed. The (004) peak position was not corrected for polarization and absorption as such corrections would be very small for a flat specimen at a two theta angle of  $53^\circ$ .<sup>69</sup> The degree of ordering or the crystallite size in the C direction,  $L_c$ , was determined using Scherrer's formula for line broadening:<sup>40</sup>

$$L_c = \frac{K \lambda}{B \cos \theta}$$

where  $K = 0.94$  for the (002) peak of graphite,<sup>70</sup> and  $\lambda$  is the radiation wavelength,  $B$  is the peak broadening at half peak height, and  $\theta$  is the diffraction angle. Peak broadening due to lattice strain was not separated from crystallite size broadening as it was found to be very small. The root mean square lattice strain perpendicular to the basal planes,  $(\overline{\epsilon_c^2})^{1/2}$ , was evaluated for some of the deposits by considering the broadening of both the (004) and the (002) peaks<sup>71</sup> of a solid specimen. A change in the crystallite height and the root mean square lattice strain has been used as an indication of solid solubility limits in the graphite-boron system<sup>13,26</sup> and the graphite-silicon system.<sup>31</sup>

#### 3.4.6 Bend Strength Evaluation

Bend strength measurements were conducted on an Instron testing machine. Deposit samples approximately 4 mm long X 1.5 mm wide X 1 mm thick were removed from the substrate and tested in three point bending. The samples were tested with the top surface of the deposit facing the single point load. The results were analyzed by the relationship:<sup>72</sup>

$$\sigma = \frac{3P\ell}{2wt^2}$$

where  $\sigma$  is the bend rupture stress (rupture modulus),  $P$  is the applied load at failure and  $\ell$ ,  $w$  and  $t$  are the sample length, width and thickness respectively. Teflon was used

on the stationary end supports to reduce sticking friction. Bend strength measurements were used by Katz and Gazzara<sup>13</sup> to indicate microstructural changes in the boron-graphite system. These changes were interpreted by other investigators<sup>26</sup> as the limit of solid solubility of boron in graphite.

#### 3.4.7 Deposit Microhardness

Microhardness is a well known technique for determining phase limits and structural changes in metal systems and in many cases is more reliable than X-rays.<sup>73</sup> Previously, abrupt changes in bend strength have been interpreted as indicating solid solubility limits<sup>13,26</sup> and as microhardness varies in an identical manner as bend strength in pyrolytic alloy codeposits,<sup>17</sup> microhardness should also be useful to indicate any solid solubility limits. Furthermore, microhardness results can be used to complement bend strength findings as an indication of mechanical properties.

The previously prepared metallographic samples were vapor coated with a coating of aluminum thick enough to enable hardness indentations to be seen yet thin enough that the graphite structure was still visible. A 100 gm load applied for 5 seconds on a Reichert microhardness tester was used.

#### 3.4.8 Distribution of Alloying Element

The distribution of the alloying additions was determined by examining deposits of various compositions and orientations using an ARL electron probe microanalyzer which has a resolution of slightly less than 1 micron.<sup>74</sup>

#### 3.4.9 Stability of Alloying Element

The stability of the alloying element was examined by heat treating deposits of various concentrations at the temperature of deposition for twenty hours in a Brew vacuum furnace. Heat treated deposits were subsequently examined as to density, microstructure, X-ray structure, microhardness, and alloy element distribution. Chemical analysis was also carried out on some of the heat treated samples.

## 4. EXPERIMENTAL RESULTS

### 4.1 Deposition Kinetics.

#### 4.1.1 Pyrolytic Graphite

Figure 5 shows that for pyrolytic graphite deposited at  $5 \pm 1$  torr, the growth rate is constant. Values for  $n$  ( $W^n = kt$ ) vary from 0.9 to 1.2 indicating that the deposition growth is, to a good approximation, a linear function of time at a given constant pressure. For this reason, the deposition growth rate perpendicular to the substrate was also determined by measuring the actual thickness of the deposit and dividing this by the deposition time. Figure 6 shows that the growth rate of pyrolytic graphite increases with increasing deposition temperature for a deposition pressure of  $5 \pm 1$  torr. Other researchers<sup>62</sup> have found similar trends for other carbonaceous gases and different deposition conditions. Graphical analysis in Figure 5 was done by linear regression.

#### 4.1.2 Pyrolytic Graphite-Titanium Alloys

Figure 7 shows that the addition of titanium does not produce changing deposition surface conditions which change the linearity of the deposition growth as values of  $n$  are found to be between 0.9 and 1.0. Data for alloys formed at  $1975 \pm 35^\circ\text{C}$  and  $5.5 \pm 1.5$  torr also show an  $n$  value of



approximately one. The presence of titanium tetrachloride or its derivatives in the deposition gas, immediately results in a growth rate approximately one and one half times that of pure pyrolytic graphite. In addition, the growth rate further increases with increasing titanium concentration in the alloy deposit. Figure 8 indicates that with increasing titanium concentration in alloy deposits formed at  $1675 \pm 75^\circ\text{C}$ , the growth rate increases from  $54 \times 10^{-4}$  mm/min at 0.001 a/o titanium to  $96 \times 10^{-4}$  mm/min at 0.280 a/o titanium.

#### 4.1.3 Pyrolytic Graphite-Vanadium Alloys

Vanadium additions cause the growth rate to be at least four times the growth rate of pyrolytic graphite. Figure 9 shows that the growth rate in the presence of vanadium increases with an increasing propane flow rate. This is not the case in pyrolytic graphite and graphite-titanium deposits where the same propane flow rates were used as in the graphite-vanadium experiments. In these experiments, propane flow rates were sufficient so that carbonaceous gas supply did not control the deposition rate. Temperature effects on the deposition rate for the vanadium alloys can not be singled out from combined temperature and flow rate effects.

#### 4.1.4 Pyrolytic Graphite-Nickel Alloys

The deposition rate of graphite-nickel alloys is constant and the deposition growth linear with time as is seen in Figure 10. Evaluation of a 0.003 a/o nickel alloy shows a growth rate of approximately 0.005 mm/min at  $1590 \pm 30^\circ\text{C}$  and 5.5 torr. This growth rate is approximately one and one half times that of pyrolytic graphite formed under similar conditions.

### 4.2 Pyrolytic Graphite Deposition

#### 4.2.1 Metallography of Pyrolytic Graphite

The top view of a pyrolytic graphite deposit and its substrate is shown in Figure 11. The centre of the deposit is smooth and has a grey metallic lustre. In the cooler regions of the deposition surface (end sections), the pyrolytic graphite is often bumpy as is shown in the figure.

Figures 12 and 13 present two types of microstructure observed in the deposits. These micrographs were taken of cross sections with the direction of deposit growth vertical. Figure 12 shows what is commonly called a singularly nucleated pyrolytic growth, while the growth in Figure 13 is called polynucleated. Growth cones are visible in both figures and it is from the appearance of these growth cones that the microstructures are so named. In Figure 12, the apexes (nucleation point) of the majority of these cones

are on the deposition substrate. Subsequent growth stems in a continuous manner from the cone apex. The pyrolytic growth in Figure 13 contains areas which are rougher in appearance due to the presence of larger secondary growth nuclei. These nuclei are thought to be less graphitic than the rest of the deposit.<sup>62</sup> The larger growth cones are also seen in Figure 13. In extreme cases of polynucleated microstructure, these larger cones are not visible.<sup>62</sup> Both of the figures represent different graphites that were formed at 1650°C and 5 torr. The difference in the microstructure is understandable when the work of Yajima et al on pyrolytic graphite microstructure<sup>63</sup> is consulted. The conditions previously cited are in a transition region between singularly nucleated and polynucleated microstructures and thus either polynucleated, singularly nucleated, or a combination of both microstructures is possible.

Figure 1 shows the substrate material for comparison with the pyrolytic graphite. The substrate graphite is made by the Acheson Process and consists of cylindrical filler grains (which were pyrolytically formed in a fluidized bed) bonded together to give a resultant porous structure. No growth cones are visible in the filler grains.

Growth cones are readily seen in Figure 14 which shows the polished surface taken at right angles to Figures 12

and 13, or parallel to the deposition plane. These cones are of various sizes with the larger cones being visible as bumpy growths on unpolished deposits as was seen in Figure 11.

X-ray examination of the deposits shows that the basal planes of the pyrolytic graphite are aligned parallel to the plane of the deposition substrate. Some curvature of the basal planes does occur as can be seen from the cracks parallel to the basal plane in Figure 12.

#### 4.2.2 Property and Structure Variation of Pyrolytic Graphite

Table 2 lists the deposition conditions and some of the properties of the pyrolytic graphite deposits that were examined. Figure 15 shows that from 1490 to 1650°C, the apparent density of the deposit increases rapidly from 1.65 to 2.17 gm/cc. Beyond 1650°C the density levels off at approximately 2.195 gm/cc and then remains relatively constant. Results by Yajima et al<sup>63</sup> from similar deposition conditions are included in Figure 15. These results show a similar trend to the experimental values obtained. The slight differences are due to different propane flow rates. Yajima et al<sup>63</sup> found that different propane flow rates produced a slight shift in the density curve.

In Figure 16, the lattice constant,  $c$ , of the graphite is shown to remain constant at a value of 6.86 Å up to a

deposition temperature of 2200°C. This compares with a value of 6.71 Å for true graphite and a value of approximately 6.85 Å found by Hirai and Yajima.<sup>69</sup> Figure 17 shows that the crystallite size follows a trend similar to that observed in the density. The range of ordering of the basal plane stacks (crystallite size,  $L_c$ ) rapidly increases from approximately 100 angstroms to 300 angstroms over the temperature range 1500°C to 1650°C. The size then slowly increases to approximately 350 Å at 2000°C. These findings are comparable to those found by other researchers.<sup>63,69,75</sup>

Table 3 presents the microhardness results. The microhardness of the planes perpendicular to the basal plane remains relatively constant at an average value of approximately 73 Kgm/mm<sup>2</sup> with a scatter of  $\pm$  11%. Data on basal plane microhardness are inconsistent.

#### 4.3 Pyrolytic Alloy Codeposition.

##### 4.3.1 Graphite-Titanium Alloy Codeposition

The known phase diagram<sup>76</sup> for the carbon-titanium system is given in Figure 18. At a concentration of greater than 50 a/o carbon, a two phase system is indicated-- titanium carbide and graphite. No information on the phase system is given beyond 80 a/o carbon.

a. Metallography of Graphite-Titanium Alloy Codeposits.

The alloys prepared of pyrolytic graphite and titanium all have singularly nucleated microstructures. Very little structural difference can be detected among alloys of different concentrations and different forming conditions. This is seen in Figures 19 and 20. Figure 21, however, shows that the frequency of occurrence of the larger cones increases with increasing metal concentration. It is more difficult to obtain a scratch-free surface for metallographic examination with the graphite-titanium alloys than with pure graphite.

Electron microscopy was performed on a wide range of alloy compositions. Hexagonal shaped precipitates were found distributed throughout all specimens. Figure 22 shows that the precipitates are approximately  $2,000 \text{ \AA}$  across. A diffraction pattern and the area from which it was obtained are presented in Figure 23. Analysis of the diffraction pattern shows that it is compatible with the precipitate being titanium carbide (TiC) and that the diffraction spots are from planes belonging to the [111] zone.

b. Properties and Structure of Graphite-Titanium Alloy Codeposits.

Table 4 lists some of the alloys examined and their properties. Alloys were formed at  $1675^{\circ}\text{C}$  containing from 0.007 to 0.285 a/o titanium (0.029 to 1.127 w/o), at  $1975^{\circ}\text{C}$  containing from 0.002 to 0.012 a/o titanium (0.009 to 0.046 w/o), and at  $2200^{\circ}\text{C}$  containing 0.001 a/o titanium

(less than 0.005 w/o). As the deposition temperature was increased, the amount of titanium that could be introduced into the codeposit decreased because of the increase in the titanium vapor pressure with increasing temperature.

Figures 24 and 25 indicate that the density of the alloy increases with increasing titanium concentration at deposition temperatures of 1675°C and 1975°C. This increase is at a rate many times greater than a calculated density increase for direct titanium addition to graphite. Data from Figures 24 and 25 were analyzed by linear regression. The maximum deviation is only  $\pm 0.5\%$  and the scatter on the graphs appears large because of the scale used on the ordinate. Four figure reliability was found to be reasonable for densities determined by the sink-float technique.

The lattice parameter and the root mean square of the lattice strain in the c direction, as determined by X-ray analysis, are relatively constant as can be seen in Table 4-- the lattice parameter at  $6.86 \overset{\circ}{\text{Å}}$  and the strain at 0.003 to 0.004 for deposits formed at 1675°C. The lattice strain is approximately 0.001 for the higher temperature deposits. Figures 26 and 27 show that the crystallite height,  $L_c$ , immediately decreases with the introduction of the titanium and then remains constant with increasing titanium concentration. The experimental scatter is quite large with some values being  $\pm 10\%$  of the mean.

X-ray diffractometry shows a peak corresponding to the (111) peak of titanium carbide. Detection is possible at a concentration as low as 0.012 a/o titanium in the alloys. Such detection requires the use of solid samples so that preferred orientation effects can be employed to best advantage. That is, in the extremely low concentration alloys no non-graphite peaks are detected in powdered samples. In solid samples, however, alignment of second phase particles makes diffraction from (111) carbide peaks strong enough to be detectable. No other peaks are detected and the (111) planes of the carbide are aligned with the basal planes of graphite because this peak can only be detected when the basal plane orientation of the graphite is examined.

The size of the titanium carbide particles in the [111] direction is estimated to be 2,000 Å using the Scherrer formula. This compares with the 2,000 Å diameter of the precipitates' (111) planes observed by electron microscopy (Fig. 22).

Flexural strength tests were done on most of the alloy deposits, but the technique was abandoned due to the inconsistency of the results achieved from tests conducted on any one specimen. Table 5 gives some indication of the variation in strengths obtained from an alloy containing 0.014 a/o titanium. It is thought that the presence of micro cracks prevents a true bend rupture strength from being determined.



Figure 28 presents the rupture strengths where only the highest values or average of highest values are plotted for each alloy. This was done to avoid consideration of pre-cracked alloy samples. Very little difference between the alloyed and the unalloyed graphite is indicated. It should be noted that microhardness results were more consistent than bend strength data. These results are presented in Figures 29 through 32.

In Figure 29, the microhardness of the planes at right angles to the basal planes increases from 75 to approximately  $90 \text{ kgm/mm}^2$  between pure graphite and a titanium concentration of 0.020 a/o. The microhardness then rapidly decreases to  $70 \text{ kgm/mm}^2$  where it remains constant with increasing titanium. In higher temperature deposits, the microhardness on the non-basal planes remains relatively constant although a linear regression analysis of the points indicates a decrease in hardness with an increasing titanium concentration (Fig. 30). For the alloy deposits formed at  $1675^\circ\text{C}$ , the microhardness on the basal plane decreases from  $85 \text{ kgm/mm}^2$  to approximately  $61 \text{ kgm/mm}^2$  where it remains constant with increasing titanium additions beyond 0.03 a/o. The deposits formed at  $1975^\circ\text{C}$  (Fig. 32), however, show a slight increase in basal plane hardness with increasing titanium. In Figure 31, as in Figure 29, a higher hardness is indicated at a concentration of approximately 0.020 a/o titanium.

The electron microprobe showed the titanium in the deposits to be distributed throughout the alloy. Figure 33 does show some slight clustering of the titanium as does Figure 34. Figure 33 also shows a band of higher concentration along the right hand side of the figure. This band occurs in an area very close to the bottom of the deposits; i.e., the apex area of the growth cones. Fluorescent radiation pictures from the electron microprobe analyzer represent a metal distribution in three dimensions as the probe excites radiation from a depth of approximately  $1\mu$  below the sample surface.<sup>77</sup>

c. Stability of Graphite-Titanium Alloy Codeposits.

A series of alloy deposits was heat treated in a vacuum of  $10^{-5}$  torr at  $1600 \pm 100^\circ\text{C}$  for 20 hours. The heat treated samples were then evaluated as to density, X-ray structure, microhardness, microstructure, and titanium distribution. Table 6 indicates that the density remains approximately unchanged with the heat treatment. The alloy does, however, appear to have become more graphitic with the lattice parameter showing a slight decrease and the mean crystallite height possibly showing a slight increase. Chemical analysis of samples after heat treatment showed that a maximum loss of 15% titanium can be expected as is indicated in Table 7. Both light and electron microscopy indicate no detectable structure changes. The carbide

particles are still found to be aligned with the (111) planes parallel to the graphite basal planes and the size of the particles are unchanged at  $2,000 \text{ \AA}$ . X-rays picked up a stronger (111) peak of titanium carbide than was detected in the unheat-treated deposits. Figure 35 shows that the (111) peak is stronger in a heat treated sample of lower titanium concentration than a sample which is of higher titanium concentration but which had received no heat treatment.

Figures 36 and 37 show that the microhardness of the samples which were heat treated has changed slightly. The microhardness on the planes perpendicular to the basal planes increased from  $70 \text{ kgm/mm}^2$  in the unheat-treated samples to  $76 \text{ kgm/mm}^2$  in the heat treated samples. The increase in hardness peak observed in the unheated deposits at a composition around 0.020 a/o titanium is not as obvious in the heat treated samples. This is because there are fewer data points at an approximate concentration of 0.020 a/o titanium in Figure 36 (heat treated alloys) than in Figure 29 (as-deposited alloys). For this reason, and also because other microhardness plots of alloys deposited at  $1675 \pm 75^\circ\text{C}$  (Figs. 29 and 31) show higher hardness readings in the vicinity of 0.020 a/o titanium, the high hardness value in Figure 36 should not be dismissed as experimental scatter. The microhardness on the basal planes

shows an increase from 61 kgm/mm<sup>2</sup> to 78 kgm/mm<sup>2</sup> in the heat treated samples over the as-deposited samples.

Figures 38 and 39 show that there is no change in the titanium distribution during heat treatment. Figure 38 was obtained from the same alloy deposit as that of Figure 33 and can therefore be compared directly with it. As in Figure 33, a band of higher titanium concentration appears in an area which was formed in the initial stages of the alloy deposit. Figure 39 is of a lower concentration alloy and indicates uniform distribution of the titanium with no isolated areas of high concentration.

#### 4.3.2 Graphite-Vanadium Alloy Codeposition

The phase diagram for the carbon-vanadium system<sup>78</sup> is presented in Figure 40. Beyond a composition of 47 a/o carbon, a two phase system exists--vanadium carbide (VC) and graphite. A solubility of 0.088 a/o vanadium in graphite is reported.<sup>15</sup>

Difficulties occurred in preparing alloys of pyrolytic graphite with vanadium. The deposit growth rate is very high as discussed previously. It was not possible to form alloys containing more than 0.001 a/o vanadium under the range of deposition conditions investigated.

##### a. Metallography of Graphite-Vanadium Alloy Codeposits.

Figure 41 shows a singularly nucleated pyrolytic

graphite-vanadium alloy. This alloy is somewhat different in appearance than other singularly nucleated deposits as there is no pronounced "stringy" substructure. (See Figures 12, 13, 19, and 20.) The structure in the lower region of the deposit is also different from that in the upper region as indicated by the appearance of a band in the lower region when the deposit is examined under polarized light. The microstructure shown in Figure 42 is more characteristic of pure graphite formed at a higher deposition pressure.<sup>63</sup> It has large growth cones which contain many smaller cones. Figure 43 shows a plume-like carbon growth on the deposition substrate. Such plume growths are found at higher deposition pressures in pure pyrolytic graphite.<sup>63</sup> Figure 44 shows that minute vanadium or vanadium compound additions result in an increase in the diameter of the growth cones. The presence of a vanadium addition along with a slight pressure increase results in the appearance of secondary growth cones inside larger ones.

b. Properties and Structure of Graphite-Vanadium Alloy Codeposits.

The results of some of the alloy codeposition experiments are given in Table 8 which indicates that the alloy deposits are more graphitic than pyrolytic graphite formed under similar conditions. The lattice parameters for the alloys average  $6.85 \text{ \AA}$  compared with  $6.86 \text{ \AA}$  for

pyrolytic graphite. The table also indicates that the crystallite height,  $L_c$ , is on the average 320 Å with some lower values being observed.

Although the alloy deposits are more graphitic than pure pyrolytic graphite, the alloys exhibit lower anisotropy. This is evident from the strengthening of  $(hko)$  peaks and the weakening of  $(ool)$  peaks in diffractometer scans. This increase in isotropy is due to a higher deposition rate. Figure 45 indicates that the higher deposition rate also produces a decrease in apparent density with a density of 2.195 gm/cc only being achieved at a deposition temperature of 1850°C. This density (2.195 gm/cc) is reached at approximately 1700°C in pyrolytic graphite. Figure 45 further shows that the apparent density of pyrolytic graphite-vanadium alloys varies linearly with temperature between 1770°C and 1850°C. At 1770°C, the alloy deposit has a density of 1.71 gm/cc.

Although it was expected that second phase particles would not be detectable even if they were present, chromium radiation was used in X-ray diffractometer scans for precipitates in solid alloy specimens. As anticipated, no additional peaks were found.

Microhardness results are presented in Table 9 from which it can be seen that hardness values on the non basal planes are approximately 76 kgm/mm<sup>2</sup> for alloys formed at

5 torr. The alloys formed at higher pressure show a significant increase in hardness (as much as 230%). This increase in hardness is also evident when filing the deposits to obtain powder samples.

#### 4.3.3 Graphite-Manganese Codeposition.

One alloy of pyrolytic graphite and manganese was formed at  $1500 \pm 30^\circ\text{C}$  and 5 torr. Formation of an alloy at  $1200^\circ\text{C}$  was also attempted but the graphite formation rate was so slow that a sample of sufficient size for examination could not be produced.

Manganese has an equilibrium vapor pressure of 10 mm Hg at  $1510^\circ\text{C}$ .<sup>2</sup> This vapor pressure is greater than the deposition pressure, nevertheless, the alloy deposit at  $1500^\circ\text{C}$  contains  $1 \times 10^{-4}$  a/o manganese.\* This alloy has a density of 1.701 gm/cc and a crystallite height of  $156 \text{ \AA}$ . The c lattice spacing is not determinable as the (004) peak cannot be resolved. This indicates a very low degree of graphitization.

#### 4.3.4 Graphite-Nickel Alloy Codeposits.

The carbon-nickel phase diagram has not been established with certainty. Difficulties arise around the

---

\* Analysis done by Chicago Spectro Service Laboratory, Inc., Chicago, Illinois.

existence and stability of the carbide phase  $\text{Ni}_3\text{C}$ . Most researchers agree that this compound exists but the stability of it and its crystal structure are not definite.

a. Metallography of Graphite-Nickel Alloy Codeposits.

Alloys formed between pyrolytic graphite and nickel have a very high metallic lustre. In addition, the deposit surface is very smooth and contains few growth cone bumps. Figure 46 shows the alloy deposit microstructure to be singularly nucleated. Also, as with vanadium but even more so with nickel alloys, there is no "stringy" substructure present in the growth cones. The metallographic specimens are relatively easy to polish.

Examination of the graphite-nickel alloys in the electron microscope showed the possible existence of precipitates. One diffraction pattern was observed which contained spots that did not correspond to diffraction from graphite planes. However, the area from which the diffraction pattern was obtained was too thick to be resolved for precipitates.

b. Properties and Structure of Graphite-Nickel Alloy Codeposits.

It was found that alloys containing more than 0.003 a/o nickel could not be formed with the range of deposition techniques being used. Table 10 gives some of the properties of the alloys formed. The trend to a decreasing density with a lower deposition temperature is similar



to that found for pyrolytic graphite over this temperature range. (See Figure 15.) The lattice parameter,  $c$ , and the crystallite height,  $L_c$ , also show values similar to those found in pure graphite. The lattice parameters, however, appear to be somewhat smaller than those of pure graphite but more data is required to state with certainty that this is so. Microhardness on the planes perpendicular to the basal planes is  $78.9 \pm 4.2 \text{ kgm/mm}^2$ . This is slightly higher than values obtained for pyrolytic graphite formed under similar conditions.

Debye-Scherrer diffraction patterns were obtained using copper radiation to examine two powdered samples obtained from alloy deposit #2PCNi. Exposure times of approximately 140 hours are required to detect second phase materials. In patterns obtained from both samples, a very faint diffraction ring corresponding to an unknown with a  $d$  value of  $2.50 \pm 0.01 \text{ \AA}$  is detected. All other rings present can be associated with graphite diffracting planes.

Electron microprobe examination of the nickel distribution in one of the alloys (#2PCNi) shows nickel to be distributed throughout the area examined. Figure 47 shows a band of higher concentration near the top face of the deposit.

## 5. DISCUSSION

### 5.1 Evaluation of Pyrolytic Deposition.

The deposition growth of all deposited materials is concluded to be linear with time; i.e.,  $n = 1$  for the assumed power growth law  $W^n = kt$ . Deposition temperature and alloy additions do not affect deposition surface conditions such that the surface changes the linearity of the deposition for deposition pressures of  $5.5 \pm 1.5$  torr.

The alloy additions, however, do enhance the rate of deposition. The deposition rate was shown to increase with increasing titanium concentration in the alloy. Whether or not any of the enhancement is due to the presence of the titanium in the deposition chamber is not clear as  $TiCl_4$  was used in the codeposition and the presence of chlorine is known to increase the deposition rate of pyrolytic graphite.<sup>79</sup> However, in the vanadium alloys, the enhancement of the deposition rate is several times that of the titanium alloys and since vanadium tetrachloride is very similar to titanium tetrachloride, the pronounced enhancement is concluded to be caused by the presence of the vanadium.

To test the catalytic effect of vanadium on graphite deposition further, vanadium was melted onto part of a

substrate on which pyrolytic graphite was subsequently deposited. No deposit formed on the molten vanadium. Furthermore, as very little vanadium was found incorporated in the pyrolytic alloy deposits, the catalytic effect of vanadium must occur in the gaseous phase. This would also help explain why the characteristics of vanadium alloy deposition were similar to those of pyrolytic graphite formed at a higher pressure. The effect of vanadium must therefore be such that it catalyses the gas phase reaction in a manner similar to increased pressure.<sup>56</sup> This finding differs somewhat from those of other researchers<sup>21,61,80,81</sup> studying different metals where the deposition rate over metal substrates has been found to be increased by as much as five times.<sup>80</sup> The substrates employed were nickel, iron, platinum, molybdenum, tungsten, titanium and tantalum. This indicates that both gas phase and surface reactions can be of importance in controlling the pyrolytic deposition rate.

## 5.2 Discussion of Alloy Deposition Results.

### 5.2.1 Graphite-Titanium Alloys

The presence of chlorine in a pyrolytic deposition chamber is known to enhance the density of the resultant graphite.<sup>79</sup> This enhancement occurs as a shift in the density minimum to a lower temperature, (see Figure 15)

the density at higher formation temperatures remaining unchanged, and hence it is concluded that the density increase displayed in Figures 24 and 25 is a result of the presence of titanium. This must be a catalytic effect as the density increase in the deposit is greater than a calculated density increase for direct titanium addition. The density increase is greater in deposits formed at 1975°C than those formed at 1675°C indicating that the catalytic effect of the titanium is a function of temperature. Just exactly how this enhanced densification has taken place is not clear. The lattice parameter,  $c$ , remains constant and the crystallite height decreases. This could possibly mean that the crystallite diameter is greater in a graphite-titanium alloy as compared to pure graphite deposits. No measurement of the crystallite diameter could be obtained as the (110) and (100) peaks of the deposits were not strong enough to allow measurements to be taken. However, if the perfection of the graphite lattice was extended in the radial direction, some enhancement of the (110) and (100) peaks should have been observed. This was not found to be the case.

Alternatively, the enhanced densification could be a result of the forming characteristics of the deposit. Diefendorf<sup>52</sup> concludes that the structure of a pyrolytic

graphite is largely controlled by gas phase reactions and surface mobility. He further states that with a temperature increase, the deposition rate increases and the density of the deposit decreases until such a temperature that surface mobility would allow rearrangement of the deposit and thus a density increase. It is quite possible that the presence of titanium enhances surface mobility and allows for a more dense packing of graphite crystals. It is known<sup>24,25</sup> that during heat treatment, the presence of titanium at concentrations greater than 5 w/o enhances graphitization and induces structural changes. However, the density is affected only slightly, any change in density being less than the change in density of pure graphite given an identical heat treatment.<sup>25</sup> Thus, density must be most strongly affected by crystallite arrangement, and titanium must enhance this arrangement upon deposition.

The presence of second phase particles whose electron diffraction and X-ray patterns correspond to reflecting planes of titanium carbide leads to the conclusion that any solid solubility of titanium in graphite must be below 0.002 a/o titanium which is the lowest concentration examined in this program. In codeposition, the carbide forms so as to have its dense packed planes ( (111) planes ) parallel to the dense packed basal planes of the graphite. The titanium carbide particles are approximately  $2,000 \text{ \AA}$

in size and appear to be equiaxed. It is thought that the presence of these carbide particles also explains why it was difficult to obtain a scratch free surface for metallographic examination. The carbide particles are removed from the deposit during polishing operations and thus are available to abrade the softer graphite sample.

The other results of the investigation along with the observation of precipitates, indicates that there has been no extensive solid solution alloy formed. The structure of the alloy deposits appears to be very similar to the structure of singularly nucleated pyrolytic graphite. The root mean square of the lattice strain in the c direction remains unchanged from that of pyrolytic graphite as does the lattice c parameter. The decrease in the crystallite height can be viewed as a consequence of an enhanced deposition rate.

Figure 48 presents some of the results of Marinkovic et al<sup>31</sup> on the silicon-graphite system where changes in crystallite size and density have been interpreted as indicating the extent of solid solubility of silicon in graphite. In this instance, property changes increase to a maximum--the solubility limit, and then decrease. Both the density and crystallite size showing maximization at the same silicon concentration. Changes or lack of changes observed in density and structural parameters of graphite-

titanium alloys are not consistent as in the graphite-silicon case and thus property changes are not interpreted as phase changes.

Although a change in microhardness values as shown in Figures 29, 31, and 36 could be taken to indicate that the limit of solid solubility of titanium in graphite is 0.020 a/o, the previously discussed data do not support this interpretation. Instead, it is proposed that dispersion strengthening accounts for the microhardness peak. A two phase system--titanium carbide and graphite, is thus believed to exist down to concentrations as low as 0.002 a/o titanium. Figure 49 shows that the free energy of formation for titanium carbide is highly negative (-40 Kcal/mole C) which indicates that the carbide formation is energetically favourable at the temperatures under consideration, pressure effects being neglected. It is also feasible that the free energy of formation would be essentially unchanged if the pressure effect was known as the pressure is not thought to be a significant variable at the 5 torr pressure involved.

The theory that the alloy is dispersion strengthened is supported by a number of facts. Titanium has a relatively large atomic radius (1.458 Å) and hence its diffusivity in graphite at 1600°C is expected to be low. The carbide is also particularly stable at this temperature.

Thus, heat treatment of a 0.020 a/o titanium alloy should result in little loss of dispersion hardening which was found to be the case (Figure 36). The electron microprobe analysis confirmed the stability of the titanium distribution. The dispersion strengthening is thought to occur in part by coherency effects. An enhancement of (111) peaks of the carbide in the heat treated alloys was observed. The size of the carbide particles was found to be unchanged in the heat treated samples which was confirmed by electron microscopy and diffraction peak broadening. Some reorientation of carbide particles in the graphite, possibly altering coherency effects, is thought to have occurred with heat treatment. A diffraction pattern of a carbide crystal in which the planes of the [110] zone were at right angles to the basal planes of graphite was observed for a non-heat treated sample. This pattern is presented in Figure 50. Heat treatment could allow this particle to become reoriented so that the (111) carbide planes become parallel to the graphite basal planes.

Titanium carbide has a rock salt lattice structure and hence the (111) plane can be thought of as a dense packed plane of titanium atoms as is seen in Figure 51. Figure 51 further shows how the interface between the carbide and the graphite may be considered semi coherent. The hexagonal shape of the carbide is also accounted for in this two



dimensional mode. Similarly, spacings of approximately 2.5 Å between (111) carbide planes and 3.4 Å between graphite basal planes could lead to a highly strained semi coherent interface. (Basal plane spacings of 2.5 Å have previously been found in graphite.<sup>83</sup>) Semi coherent interfaces are known to be responsible for strengthening in metal-metal systems.<sup>84</sup> Also size and distribution of precipitates affect strength<sup>84</sup> and the subsequent decrease in hardness of alloys with a titanium concentration greater than 0.020 a/o could be due to these factors. A more detailed study is, however, required to verify the proposed hardening mechanism in graphite-titanium alloys.

#### 5.2.2 Graphite-Vanadium Alloys

The results of the codeposition experiments using vanadium clearly indicate that vanadium catalyzes pyrolytic deposition. Also, it appears that the alloy formed is more highly graphitized than pyrolytic graphite formed under comparable conditions. The increase in the isotropy of the alloys does not mean that the deposit is less graphitic. The enhancement of graphitization by vanadium has been studied previously and the carbide diffusion mechanism was used to explain the observed behavior.<sup>15</sup>

Under the experimental conditions, no alloys containing more than 0.001 a/o vanadium were formed. Vanadium carbide has previously (1931) been formed by vapor phase

deposition from the tetrachloride and toluene at 1500 to 2000°C.<sup>85</sup> The deposition conditions, however, were different from those used in this study.

The soot formed in the deposition chamber was examined by X-rays and no evidence of the carbide was found there; however, X-ray diffraction peaks from a vanadium oxychloride complex were present.<sup>86</sup> The concentration of vanadium in the soot was found to be 0.5 w/o. This supports the theory that alloys are most readily formed from materials of low graphite character. As the degree of graphitization in the vanadium alloys is reasonably high, positions for vanadium or vanadium carbide in the alloy deposit are limited. This results in alloy deposits with a low vanadium concentration.

### 5.2.3 Graphite-Manganese Alloys

Little can be said about the one pyrolytic graphite-manganese alloy formed other than that no obvious catalyzation of deposition or enhancement of graphite properties could be seen. It is surprising that any manganese at all was found to be present in the alloy as the vapor pressure of manganese at 1500°C far exceeds the total deposition pressure. Possibly the manganese has been trapped or a strong bond has been formed within the graphite. Manganese which has an outer electronic configuration of  $3p^6 3d^5 4s^2$  could be a good candidate for forming bonds with the pi electrons of carbon in graphite. A number of manganese

carbides are thought to exist although numerous contradictory results are reported<sup>76,78,87</sup> indicating highly metastable conditions in the carbon-manganese system. The concentration of manganese in the alloy formed was too low for X-ray diffraction to detect any possible carbide peaks if they had been present.

#### 5.2.4 Graphite-Nickel Alloys

Nickel is well documented as being a graphitizing catalyst.<sup>24,46,48,88</sup> The uniformity and metallic-like appearance of the graphite codeposited with nickel seem to bear this out. However, other parameters examined do not provide sufficient evidence of enhanced graphitization.

The evidence for the presence of a second phase material in the alloy deposit is strong. The spots observed in the electron diffraction pattern did not fall on existing graphite rings and therefore are due to the presence of a second phase material. The extra ring observed in the Debye-Scherrer patterns could be due to nickel-iron oxide ( $\text{NiFe}_2\text{O}_4$ ).<sup>86</sup> The purity of the nickel carbonyl used to form this alloy is not known; furthermore, the carbonyl was supplied in a steel pressure vessel and thus the possibility of iron carbonyl being present is strong.

As with vanadium, nickel alloy deposits which contained greater than a certain percentage (0.003 a/o) of nickel

would not be formed. In the case of nickel, the low metal concentration could be due to the premature decomposition of the carbonyl to give nickel and carbon monoxide and leave the decomposing gas in the vicinity of the substrate deficient in nickel. Significant amounts of nickel, nickel oxide and possibly some nickel carbide were found in an X-ray analysis of soot formed in the deposition chamber during graphite-nickel alloy formation.

Alternatively, we can again assume that alloy formation or solid trapping is greatest in graphite of low perfection and as nickel enhances graphitization, very little metal would be expected in deposits of graphite formed in the presence of nickel. Figure 47 shows the nickel concentration is greatest at the top surface of the deposit. It is probable that the outer surface of the deposit will be the least graphitized. For comparison, the density of surface layers of a pyrolytic graphite-titanium deposit was found to be 2.140 gm/cc compared with a middle layer density of 2.146 gm/cc. (See Appendix A, Item 3.)

### 5.3 Phase Relationships in Alloys.

The alloys formed in these experiments appear to be two phase systems even though the metal concentration in the alloys is quite low and there is a possibility of solid solutions existing at these concentrations. This

conclusion is supported by the presence of precipitates in the titanium-graphite and nickel-graphite systems. Other work concerned with different transition metal and graphite systems also tends to support this conclusion. The two reported solubilities of 0.088 vanadium<sup>15</sup> and 0.3 nickel<sup>6</sup> in graphite are probably too high and this point is discussed in Appendix B.

Wolf et al<sup>89</sup> studied diffusion of silver, nickel, uranium, thorium, and radium in various types of graphite. These researchers felt that substitutional and interstitial diffusion are negligible and that all mass transport proceeds via subgrain boundaries. This was shown by examining diffusion in a number of graphites, each presenting a different degree of crystal perfection, and finding that diffusion is the least in graphites having the smaller subgrain boundary area. Hummond<sup>90</sup> and Riedinger et al<sup>91</sup> also found that diffusing species do not use substitutional or interstitial diffusion mechanisms but rather diffuse primarily via grain boundaries and pores. The Hummond study was an examination of niobium diffusion in pyrolytic graphite while Riedinger et al studied the diffusion of cesium and barium through graphites of low helium permeability. All three of the above studies indicate or state that the solubilities of foreign atoms within the graphite lattice are small.

In a study of carbon deposited on metal substrates at 650 to 750°C, Robertson,<sup>92</sup> using the microprobe, found no evidence of nickel, cobalt, or iron in regions of high crystal perfection. Oxidation studies, however, did indicate that possibly these elements were present. This led Robertson to conclude that metal concentrations in crystalline regions of graphite were too small to be detected by the electron microprobe. Such concentrations must certainly be below 0.001 a/o, for absorption effects will be small when detecting a heavy metal in a light matrix like carbon. The work of Courtney and Duliere<sup>93</sup> also showed no iron present in a highly crystalline area of graphite; however, iron was present in adjacent carbon material.

The existence of two phase alloy systems can be explained by examination of alloying principles for metal-metal systems where the solubility limit is reached in cases when the Fermi surface makes contact with the Brillouin zone boundaries.

The band model developed for graphite is a simplified two band approach which neglects layer plane interactions. It is found that there is a band overlap of 0.03 to 0.04 eV<sup>94</sup> between the conduction and the valence bands.

The Brillouin zone of graphite is hexagonal in k space. Theoretical calculations<sup>94,95</sup> indicate that the Fermi surfaces will be located at the corners of the Brillouin zone.

Thus there is little chance that any extensive solid solutions can be formed between graphite and transition metals.

The Hume Rothery electronegativity rule<sup>96</sup> which states that the extent of solid solution is limited where large electronegativities exist between solute and solvent, also helps explain the limited solubility. Carbon has a Pauling electronegativity of 2.5 eV<sup>97</sup> while that of transition metals is 1.3 to 2.4 eV with the majority of the elements having an electronegativity around 1.6 eV. An electronegativity difference of more than 0.3 eV is quite large and thus solid solutions become more restricted.

#### 5.4 Engineering Significance of Alloys.

##### 5.4.1 Deposition Rates

The formation of alloys has been shown to enhance the rate of pyrolytic deposition. In some instances, this enhancement has been at the expense of preferred orientation which could be of advantage or undesirable depending on the degree of anisotropy wanted in the final alloy. In the case of the vanadium alloys formed using  $VCl_4$ , highly enhanced deposition rates can be achieved with limited contamination of the graphite while with titanium alloys, higher rates of enhancement can only be achieved by the incorporation of more titanium in the deposit. Nickel was found to enhance the deposition rate by 1.5 times which is

not as significant an enhancement as that produced by titanium and vanadium. Moreover, this rate is only one third that reported for deposition over the metal foil. This higher rate was, however, achieved at a lower deposition temperature.<sup>80</sup>

#### 5.4.2 Enhanced Graphitization

Alloy additions by the pyrolytic codeposition method have been shown to enhance graphitization. Such a realization allows for the formation of massive, highly graphitic forms of carbon at lower formation temperatures. Titanium enhances the densification of graphite markedly. This enhancement is a function of titanium concentration in the alloy.

Vanadium additions to graphite give a lower  $c$  lattice spacing and a higher  $L_c$  crystallite size thus indicating a higher degree of graphitization. However, the overall density of vanadium-containing alloys is somewhat less than that of pyrolytic graphite; probably as a result of the enhanced deposition rate. Nickel also appears to promote a smaller lattice spacing.

#### 5.4.3 Second Phase Hardening

The results of the microhardness tests on graphite-titanium alloys show the possibility for dispersion hardening in graphite-transition metal systems. Data plotted in



Figure 52 also indicates the possibility of an alloy hardening and strength improving mechanism occurring in the graphite-niobium system. Such findings are of significance in improving the relatively low strength of graphite.

### 5.5 Summary.

The pyrolytic codeposition process was used to form graphite alloys at 5 torr pressure and between 1500 and 2200°C. The findings of the alloy studies are summarized below.

1. Titanium carbide was found in graphite alloys at concentrations as low as 0.002 a/o titanium.
2. Evidence of solid solubility of vanadium in graphite was not found for alloys which contained 0.001 or less atomic percent vanadium.
3. Graphite-nickel alloys containing 0.003 a/o nickel were found to contain precipitates.
4. Carbide particles cause dispersion hardening in graphite-titanium alloys up to a concentration of 0.020 a/o titanium.
5. Pyrolytic deposition growth is linear with time and alloy additions do not change the linearity of the deposition for deposits formed at  $5.5 \pm 1.5$  torr.

6. The deposition rate in pyrolytic graphite-titanium alloys increases with increasing titanium concentration in the alloy.
7. The presence of vanadium tetrachloride in the vapour phase enhances the rate of pyrolytic deposition by a factor of at least four times the rate of pure pyrolytic graphite deposition.
8. The rate of pyrolytic deposition was not affected by manganese.
9. Nickel increases the rate of pyrolytic deposition by 1.5 times that of the pure pyrolytic graphite deposition rate.
10. Titanium, vanadium, and nickel promote graphitization in pyrolytic codeposition.
11. Titanium enhances densification of pyrolytic graphite.

## 6. CONCLUSIONS

From the experimental data presented in this report, it is concluded that improvement of pyrolytic graphite properties can be achieved by codeposition of graphite and an appropriate transition metal. Areas of property improvement are the degree of graphitization and the microhardness. It is probable that the strength of the codeposited material can also be improved.

Changes in the rate of pyrolytic deposition can be achieved by codepositing graphite and a transition metal. Different metals have different effects on the deposition rate. It is also not necessary for large metal concentrations to be taken into the graphite for a highly enhanced deposition rate to occur.

Any solid solubility of transition metals in graphite is very limited. Even though large interstitial spaces are present in the graphite lattice, interstitial solubility is very low. In some cases, large electronegativity differences between transition metals and carbon mean that competition between the carbide phases and the solid solution phase results in a very restricted solid solution. Theoretical calculations of the electronic structure of graphite indicate that solubility may be limited because of the possibility of the Fermi surface making contact with

the Brillouin zone boundary with the addition of solute metal atoms.

It is further concluded that the uptake of metals in graphite is a function of the degree of graphitization (crystallinity). Excess bonding electrons are available at crystal defects in graphite. These electrons can be used to form bonds with foreign metal atoms and thus solubility will increase with an increasing defect concentration. This is not true matrix solid solubility but it must be considered in a material which displays a range of crystallinity as does graphite.

REFERENCES

1. J. Rappeneau and G. Jouquet, Les Carbones, Tome I, A. Pacault (ed.), Masson et C<sup>ie</sup>, Paris, 1965, p. 527.
2. Handbook of Chemistry and Physics, 50th Edition, R.C. Weast (ed.), The Chemical Rubber Company, Cleveland, Ohio, 1969.
3. S. B. Austerman, Chemistry and Physics of Carbon, Vol. 4, P.L. Walker, Jr. (ed.), Marcel Dekker Inc., New York, 1968.
4. M. Humenik, Jr., D. W. Hall and R. L. Van Alsten, "Graphite-Base Cermets", Metal Prog., April 1962, p. 101.
5. P. C. Li, "Preparation of Single Crystal Graphite from Melts", Nature 192, 1961, p. 864.
6. H. M. Strong and R. E. Hanneman, "Crystallization of Diamond and Graphite", J. Chem. Phys. 46, 1967, p. 3668.
7. G. R. Henning, Progress in Inorganic Chemistry 1, 1959, p. 125.
8. R. C. Croft, Proceedings of the Third Conference on Carbon, Pergamon Press, 1957.
9. A. R. Ubbelohde and F. A. Lewis, Graphite and Its Crystal Compounds, Oxford University Press, London, 1960.

10. R. C. Croft, "Lamellar Compounds of Graphite", *Quart. Revs. London* 14, 1960, p. 1.
11. W. Rudolf, Advances in Inorganic Chemistry and Radiochemistry 1, 1959, p. 233.
12. C. E. Lowell, "Solid Solution of Boron in Graphite", *J. Am. Ceram. Soc.* 50, 1967, p. 142.
13. R. N. Katz and C. P. Gazzara, "The Influence of Boron Content on the Fine Microstructure of Pyrolytic Graphite", *J. Mat. Sc.* 3, 1968, p. 61.
14. F. Tombrel, "Effet du Bore sur la Structure et les Propriétés Mécaniques a Haute Température du Pyro-carbone", *Rev. Hautes Tempér. et Réfract.*, t. 3, 1966, p. 79.
15. E. Fitzer and B. Kegel, "Reaktionen Von Kohlenstoffgasattigter Vanadiumcarbidschmelze met Ungeordnetem Kohlenstoff", *Carbon* 6, 1968, p. 433.
16. C. F. Powell, J. H. Oxley and J. M. Bocher, Vapor Deposition, J. Wiley and Sons, New York, 1966.
17. U.S. Patent #3,464,843; Sept. 2, 1969.
18. British Patent #967,565; 1964.
19. Raytheon Company, Final Progress Report, U.S. Navy Contract NORD 19135, Nov. 1959 - Jan. 1963.
20. R. Francis, Arthur D. Little Inc., Final Progress Report, Contract DA 19-020-ORD-5490, June 1961 - June 1962.

21. A.E.B. Presland and P. L. Walker, Jr., "Growth of Single Crystal Graphite by Pyrolysis of Acetylene over Metals", Carbon 1, 1969, p. 1.
22. A. E. Karu and M. Beer, "Pyrolytic Formation of Highly Crystalline Graphite Films", J. Appl. Phys. 37, 1966, p. 2179.
23. Y. Tamai, Y. Nishiyana and M. Takahashi, "Carbon Deposition on Iron and Nickel Sheets from Light Hydrocarbons", Carbon 6, 1968, p. 593.
24. A. S. Schwartz and J.C. Bokros, "Catalytic Graphitization of Carbon by Titanium", Carbon 5, 1967, p. 325.
25. R. J. Price and J. C. Bokros, "Isochronal Annealing Kinetics and Neutron-Induced Dimensional Changes of Titanium Doped Pyrolytic Carbons", Carbon 9, 1971, p. 205.
26. S. Marinkovic, C. Suznjevic and I. Dezarov, "Simultaneous Pyrolytic Deposition of Carbon and Boron", Carbon 7, 1969, p. 185.
27. J. L. Kaae and T. D. Gulden, "Structure and Properties of Codeposited Pyrolytic C-SiC Alloys", J. Am. Ceram. Soc. 54, 1971, p. 605.
28. S. Yajima and T. Hirai, "Siliconated Pyrolytic Graphite, Part 1", J. Mat. Sc. 4, 1969, p. 416.
29. S. Yajima and T. Hirai, "Siliconated Pyrolytic Graphite, Part 2", J. Mat. Sc. 4, 1969, p. 424.

30. S. Yajima and T. Hirai, "Siliconated Pyrolytic Graphite, Part 3", *J. Mat. Sc.* 4, 1969, p. 685.
31. S. Marinkovic, C. Suznjevic, I. Dezarov, A. Mihajlovic and D. Cerovic, "Simultaneous Chemical Vapour Deposition of Carbon and Silicon", *Carbon* 8, 1970, p. 283.
32. A. Tukovic and S. Marinkovic, "Microhardness of Silicon-containing Pyrolytic Carbon", *J. Mat. Sc.* 5, 1970, p. 541.
33. S. Marinkovic, C. Suznjevic and I. Dezarov, "Simultaneous Chemical Vapor Deposition of Carbon and Uranium", *J. Nuc. Mat.* 33, 1969, p. 103.
34. M. Millet, Les Carbones, Tome 1, A. Pacault (ed.), Masson et C<sup>ie</sup>, Paris, 1965.
35. M. Inagaki and T. Noda, "Distribution of Inorganic Impurities in Graphite Electrodes", *Japan Chem. Soc. Bull.*, Vol. 36, 1963, p. 112.
36. D. W. George, "On the Release of Metallic Impurities from Graphite at Temperatures Above 1750°C", *Carbon* 3, 1965, p. 43.
37. S. Sklarew and M. J. Albom, "Pyrolytically Derived Refractory Materials", *Met. Prog.*, Feb. 1965, p. 102.
38. W. N. Reynolds, Physical Properties of Graphite, Elsevier Publishing Company, London, 1968.
39. D. B. Fischbach, Chemistry and Physics of Carbon, Vol. 7, P. L. Walker, Jr. (ed.), Marcel Dekker Inc., New York, 1971.



40. P. Scherrer, *Nachr. Ges. Wissensch Gottingen* 2, 1918, p. 98.
41. M. A. Short and P. L. Walker, Jr., "Measurement of Interlayer Spacings and Crystal Size in Turbostratic Carbons", *Carbon* 1, 1963, p. 3.
42. B. E. Warren, *Phys. Rev.* 59, 1941, p. 693.
43. A. Pacault, *Chemistry and Physics of Carbon*, Vol. 7, P. L. Walker, Jr., (ed.), Marcel Dekker Inc., New York, 1971.
44. J. Maire and J. Mering, *Chemistry and Physics of Carbon*, Vol. 6, P. L. Walker, Jr. (ed.), Marcel Dekker Inc., New York, 1970.
45. D. B. Fischbach, "The Influence of High Temperature Plastic Deformation on the Kinetics of Graphitization of Pyrolytic Carbons", *J. Chem. Phys.*, 1969, p. 121.
46. F. J. Derbyshire, A.E.B. Presland and D. L. Trimm, "The Formation of Graphite Films by Precipitation of Carbon and Nickel Foils", *Carbon* 10, 1972, p. 114.
47. S. M. Irving and P. L. Walker, Jr., "Interaction of Evaporated Carbon with Heated Metal Substrates", *Carbon* 5, 1967, p. 399.
48. C. Yokokawa, K. Hosokawa and Y. Takegami, "Low Temperature Catalytic Graphitization of Hard Carbon", *Carbon* 4, 1966, p. 459.
49. L. Kaufman, *Solids Under Pressure*, W. Paul and D. M. Warschauer (eds.), McGraw Hill Co., 1963.

50. P. L. Walker and G. Imperial, "Structure of Graphites", Nature 180, 1957, p. 1184.
51. A.R.G. Brown and W. Watt, "The Preparation and Properties of High-Temperature Pyrolytic Carbon", Industrial Carbon and Graphite, Soc. of Chem. Ind., 1958, p. 86.
52. R. J. Diefendorf, "The Deposition of Pyrolytic Graphite", J. Chim. Phys. 57, 1960, p. 817.
53. J. C. Bokros, "The Structure of Pyrolytic Carbon Deposited in a Fluidized Bed", Carbon 3, 1965, p. 17.
54. R. O. Grisdale, "The Formation of Black Carbon", J. App. Phy. 24, 1953, p. 1082.
55. B. Banerjee, T. Hirt and P. Walker, "Pyrolytic Carbon Formation from Carbon Suboxide", Nature 192, 1961, p. 450.
56. S. Yajima, T. Satow and T. Hirai, "Mechanism of the Pyrolytic Graphite Formation", J. Nuc. Mat. 17, 1965, p. 116.
57. T. J. Hirt and A. B. Palmer, "Kinetics of Deposition of Pyrolytic Carbon Films from Methane and Carbon Suboxide", Carbon 1, 1964, p. 65.
58. D. B. Murphy, H. B. Palmer and C. R. Kinney, "A Kinetic Study of the Deposition of Pyrolytic Carbon Films", Industrial Carbon and Graphite, Soc. of Chem. Ind., 1957, p. 77.

59. K. W. Carley-Macaulay and M. MacKenzie, "Studies on the Deposition of Pyrolytic Carbons", Proceedings of the 5th Conference on Carbon, Pergamon Press, 1961.
60. S. Marinkovic, C. Suznjevic, M. Gasic and I. Dezarov, "Aparatura za Dobijanje Pirolitickog Karbona", Hemijski Industrija 2, 1967, p. 326.
61. A. E. Karu and M. Beer, "Pyrolytic Formation of Highly Crystalline Graphite Films", J. Appl. Phys. 37, 1966, p. 2179.
62. F. Tombrel and J. Rappeneau, Les Carbones, Tome II, A. Pacault (ed.), Masson et C<sup>ie</sup>, Paris, 1965.
63. S. Yajima, T. Satow and T. Hirai, "Microstructure and Density of Pyrolytic Graphite", J. Nuc. Mat. 17, 1965, p. 127.
64. A. Weissler, "Simultaneous Spectrophotometric Determination of Titanium, Vanadium, and Molybdenum", Ind. and Eng. Chem., 1945, p. 695.
65. Annual Book of ASTM Standards, Part 13, American Society for Testing and Materials, Philadelphia, Pa., 1970.
66. Perkin-Elmer, "Analytical Methods for Atomic Absorption Spectrophotometry", Perkin-Elmer Corp.
67. R. E. Franklin, "A Study of the Fine Structure of Carbonaceous Solids by Measurement of True and Apparent Densities", Trans. Faraday Soc. 45, 1949, p. 274.

68. B. D. Cullity, Elements of X-ray Diffraction, Addison-Wesley Publishing Co., Reading, Mass., 1956.
69. T. Hirai and S. Yajima, "Structural Features of Pyrolytic Graphite", *J. Mat. Sc.* 2, 1967, p. 18.
70. J. C. Bokros, Chemistry and Physics of Carbon, Vol. 5, P. L. Walker, Jr., (ed.), Marcel Dekker Inc., New York, 1969.
71. G. K. Williamson and W. H. Hall, "X-ray Line Broadening from Filled Aluminum and Wolfram", *Acta Met.* 1, 1953, p. 22.
72. E. R. Maurer and M. O. Withey, Strength of Materials, 2nd ed., John Wiley and Sons, Inc., New York, 1940.
73. E. R. Petty, Techniques of Metals Research, Vol. 2, pt. 2, R. F. Bunshah (ed.), Interscience Publishers, New York, 1971.
74. Personal communication with D. Tomlinson, Department of Geology, University of Alberta.
75. J. C. Bokros and R. J. Price, "Deformation and Fracture of Pyrolytic Carbons Deposited in a Fluidized Bed", *Carbon* 3, 1966, p. 503.
76. R. P. Elliot, Constitution of Binary Alloys, First Supplement, McGraw Hill Co., New York, 1965.
77. I. Adler, X-ray Emission Spectrography in Geology, Elsevier Publishing Co., New York, 1966.

78. F. A. Shunk, Constitution of Binary Alloys, Second Supplement, McGraw Hill Co., New York, 1969.
79. P. H. Higgs, R. L. Finicle, R. J. Bobko, E. J. Seldin and K. J. Zeitsch, WADD Tech. Report 61-72, Vol. 37, May 1964, Wright-Patterson AFB.
80. Y. Tamai, Y. Nishiyama and M. Takahashi, "Carbon Deposition on Iron and Nickel Sheets from Light Hydrocarbons", Carbon 6, 1969, p. 593.
81. S. M. Irving and P. L. Walker, "Interaction of Evaporated Carbon with Heated Metal Substrates", Carbon 5, 1967, p. 399.
82. L. H. Van Vlack, Elements of Materials Science, 2nd ed., Addison-Wesley Publishing Co., Reading, Mass., 1964.
83. G. Mathews, Philips Electronics Industries Ltd., Scientific and Electronic Equipment Department, EM 300 Micrograph.
84. J. W. Martin, Precipitation Hardening, Pergamon Press, 1968.
85. C. F. Powell, I. E. Campbell and B. W. Gonser (eds.), Vapor Plating, John Wiley and Sons, New York, 1955.
86. J. V. Smith (ed.), Index to the Powder Diffraction File 1967, American Society for Testing and Materials, Philadelphia, Pa., 1967.

87. M. Hansen, Constitution of Binary Alloys, 2nd ed., McGraw Hill Co., New York, 1958.
88. V. R. Dietz and E. F. McFarlane, "Hydrogen Reaction with Carbon and Nickel Evaporated Films", Carbon 1, 1964, p. 117.
89. J. R. Wolf, D. R. McKenzie and R. J. Borg, "The Diffusion of Non Volatile Metallic Elements in Graphite", Lawrence Radiation Laboratory, Contract Number W-7405-eng-48, April 1964.
90. M. L. Hummond, "Diffusion of Nb-95 in Pyrolytic Graphite", Paper presented 7th Conference on Carbon, Case Institute of Technology, Cleveland, 21-25 June 1965.
91. A. B. Riedinger, C. E. Milstead and L. R. Zumwalt, "Experiments on the Diffusion of Cesium and Barium Through Graphites of Low Helium Permeability", Proc. of the 5th Conf. on Carbon 2, Pergamon Press, London, 1963, p. 405.
92. S. D. Robertson, "Carbon Formation from Methane Pyrolysis Over Some Transition Metal Surfaces", Carbon 8, 1970, p. 365.
93. R. L. Courtney and S. F. Duliere, "The Catalytic Graphitization of Naphthalenediol and a Urethane Foam--A Feasibility Study", Carbon 10, 1972, p. 65.

94. J. W. McClure, "Energy Band Structure of Graphite", I.B.M. Journal of Research and Development 8, 1964, p. 255.
95. M. S. Dresselhaus and J. G. Mavroides, "The Fermi Surface of Graphite", I.B.M. Journal of Research and Development 8, 1964, p. 262.
96. W. Hume Rothery and G. V. Raynor, The Structure of Metals and Alloys, 4th ed., Institute of Metals, London, 1962.
97. B. E. Douglas and D. H. McDaniel, Concepts and Models of Inorganic Chemistry, Blaisdell Publishing Co., Waltham, Mass., 1965.

TABLES



TABLE 1

Analysis of  
Matheson Natural Grade Propane  
Used in Deposition Experiments\*

<u>Gas</u>	<u>Weight Percent</u>	<u>Mole Percent</u>
Propane	91.15	90.88
Propylene	7.88	8.25
Isobutane	0.88	0.66
Neon	0.08	0.17
Methane	0.02	0.04

\* Analysis done by gas chromatography.

TABLE 2

Pyrolytic Graphite Properties

<u>Sample Number</u>	<u>Deposition Temperature (°C)</u>	<u>Deposition Pressure (torr)</u>	<u>Density (gm/cc)</u>	<u>C (Å)</u>	<u>L<sub>c</sub> (Å)</u>
1PC	1670 ± 50	5	2.163	6.860	284
2PC	1670 ± 50	5	2.179	6.868	299
4PC	1650 ± 25	4.5	2.183	6.852	279
8PC	2200 ± 40	4	2.202	6.858	334
9PC	1970 ± 30	4	2.184	6.863	348
10PC	1970 ± 30	4	2.194	6.862	355
11PC	1875 ± 45	4	2.200	6.864	275
12PC	1890 ± 20	4	2.199	6.857	316
13PC	1490 ± 50	5	1.662	6.846	119

TABLE 3Microhardness of Pyrolytic Graphite

<u>Sample Number</u>	<u>Deposition Temperature (°C)</u>	<u>Microhardness</u>	
		<u>On Basal Plane (Kgm/mm<sup>2</sup>)</u>	<u>Perpendicular To Basal Plane (Kgm/mm<sup>2</sup>)</u>
1PC	1670 ± 50		72.7 ± 5.8
2PC	1670 ± 50	85.4 ± 11.9	
4PC	1650 ± 25		76.6 ± 7.8
8PC	2200 ± 40		71.6 ± 3.5
9PC	1970 ± 30	52.6 ± 5.3	64.8 ± 2.7
11PC	1875 ± 45		78.9 ± 4.5

TABLE 4

Properties of Graphite-Titanium AlloysDeposition Temperature  $1675 \pm 75^\circ\text{C}$ Deposition Pressure  $5 \pm 1$  Torr

<u>Sample Number</u>	<u>a/o Titanium</u>	<u>Density (gm/cc)</u>	<u>C (Å)</u>	<u>L<sub>c</sub> (Å)</u>	<u>(<math>\bar{\eta}^2</math>)<sup>1/2</sup></u>
1PC	0.000	2.163	6.860	284	0.0033
2PC	0.000	2.179	6.868	299	0.0041
4PC	0.000	2.183	6.852	279	0.0034
6PCTi	0.007	2.171	6.844	258	0.0043
37PCTi	0.012	2.184	---	---	---
19PCTi	0.013	2.193	6.866	262	0.0032
15PCTi	0.015	2.180	6.865	243	0.0033
32PCTi	0.016	2.161	---	---	---
14PCTi	0.018	2.170	6.867	251	0.0038
36PCTi	0.034	2.184	---	---	---
39PCTi	0.037	2.182	6.846	---	---
38PCTi	0.049	2.181	---	---	---
18PCTi	0.078	2.185	6.876	254	0.0032
34PCTi	0.095	2.178	---	---	---
7PCTi	0.110	2.176	6.860	270	0.0032
13PCTi	0.128	2.172	6.870	230	0.0042
9PCTi	0.152	2.191	6.871	237	0.0033
35PCTi	0.157	2.180	---	---	---
33PCTi	0.172	2.179	---	---	---
16PCTi	0.178	2.184	---	---	---
17PCTi	0.187	2.171	---	---	---
11PCTi	0.241	2.192	6.869	275	0.0037
12PCTi	0.260	2.189	6.898	270	0.0042
8PCTi	0.285	2.193	6.884	254	0.0034

( $\bar{\eta}^2$ )<sup>1/2</sup> is the root mean squared of the lattice strain.

TABLE 4 (Continued)

Properties of Graphite-Titanium AlloysDeposition Temperature  $1975 \pm 35^\circ\text{C}$ Deposition Pressure  $5.5 \pm 1.5$  Torr

<u>Sample Number</u>	<u>a/o Titanium</u>	<u>Density (gm/cc)</u>	<u>C (Å)</u>	<u>L<sub>c</sub> (Å)</u>	<u><math>(\bar{\eta}^2)^{\frac{1}{2}}</math></u>
9PC	0.000	2.184	6.863	348	0.0005
10PC	0.000	2.174	6.862	355	0.0011
27PCTi	0.002	2.192	6.860	341	0.0008
25PCTi	0.002	2.195	6.863	294	0.0013
28PCTi	0.003	2.196	6.860	332	0.0003
29PCTi	0.004	2.193	6.863	334	0.0015
30PCTi	0.007	2.195	---	---	----
24PCTi	0.009	2.204	6.861	363	0.0004
26PCTi	0.011	2.198	6.860	334	0.0007
31PCTi	0.012	2.188	---	---	----

Deposition Temperature  $2200 \pm 100^\circ\text{C}$ 

Deposition Pressure 4 Torr

<u>Sample Number</u>	<u>a/o Titanium</u>	<u>Density (gm/cc)</u>
8PC	0.000	2.202
20PCTi	0.001	2.200
21PCTi	0.001	2.198

$(\bar{\eta}^2)^{\frac{1}{2}}$  is the root mean squared of the lattice strain.

TABLE 5

Bend Strength Test Results  
for Sample #15PCTi

<u>Sample</u>	<u>Length (mm)</u>	<u>Width (mm)</u>	<u>Thickness (mm)</u>	<u>Failure Load (Kgm)</u>	<u>Rupture Stress (Kgm/mm<sup>2</sup>)</u>
A	4.01	1.152	0.753	1.56	14.37
B	4.01	1.005	0.737	0.98	10.80
C	4.01	1.040	0.724	2.12	23.39
D	4.01	1.208	0.745	2.58	23.15

TABLE 6

Properties of Heat Treated  
Titanium Alloy Codeposits

<u>Sample Number</u>	<u>A/o Titanium</u>	<u>Density (gm/cc)</u>	<u>C (Å)</u>	<u>L<sub>c</sub> (Å)</u>
1PC	(0.000)	2.162 (2.163)	6.850 (6.860)	299 (284)
37PCTi	(0.012)	2.187 (2.184)	-----	-----
19PCTi	(0.013)	2.180 (2.193)	6.849 (6.866)	262 (262)
32PCTi	(0.016)	2.159 (2.161)	-----	-----
39PCTi	(0.037)	2.194 (2.182)	6.831 (6.846)	255
34PCTi	(0.095)	2.182 (2.178)	6.854	254

Brackets ( ) denote values of deposit prior to heat treatment.

TABLE 7Chemical Analysis of Heat Treated  
Graphite-Titanium Alloys

<u>Sample Number</u>	<u>A/o Titanium Before HT</u>	<u>A/o Titanium After HT</u>	<u>Apparent Loss</u>
19PCTi	0.013	0.011	15.4%
39PCTi	0.037	0.032	13.5%



TABLE 8Pyrolytic Carbon-Vanadium System Properties

<u>Sample Number</u>	<u>Deposition Temperature (°C)</u>	<u>Deposition Pressure (Torr)</u>	<u>Apparent Density (gm/cc)</u>	<u>ζ (Å)</u>	<u>L<sub>c</sub> (Å)</u>
1PCV	1770 ± 30	5	1.710	6.845	216
2PCV	1800 ± 20	5	2.020	6.847	310
3PCV	1790 ± 50	5	1.748	6.862	328
4PCV	1850 ± 50	5	2.197	6.852	322
7PCV	1550 ± 100	14	1.400	---	---
8PCV	1700 ± 30	8+	1.263	---	174

All alloy samples contain less than 0.001 a/o Vanadium.

TABLE 9Microhardness of Pyrolytic  
Graphite-Vanadium Alloys

<u>Sample Number</u>	<u>Deposition Temperature (°C)</u>	<u>Deposition Pressure (Torr)</u>	<u>Microhardness on Planes Perpendicular to Basal Planes (Kgm/mm<sup>2</sup>)</u>
1PCV	1770 ± 30	5	84.6 ± 7.9
2PCV	1800 ± 20	5	73.4 ± 3.4
4PCV	1850 ± 50	5	71.4 ± 4.0
7PCV	1550 ± 100	14	166.9 ± 9.8
8PCV	1700 ± 30	8+	103.2 ± 3.6

All samples contain less than 0.001 a/o Vanadium.

TABLE 10

Pyrolytic Graphite-Nickel System Properties

<u>Sample Number</u>	<u>Deposition Temperature (°C)</u>	<u>Deposition Pressure (Torr)</u>	<u>a/o Nickel</u>	<u>Apparent Density (gm/cc)</u>	<u>C (Å)</u>	<u>L<sub>c</sub> (Å)</u>
1PCNi	1620 ± 20	6.5	0.000	2.186	6.849	275
2PCNi	1590 ± 30	5.5	0.003	2.155	6.843	299
3PCNi	1500 ± 30	5	0.003	1.539	---	---

**FIGURES**



FIGURE 1. Speer RC4 graphite.  
80X

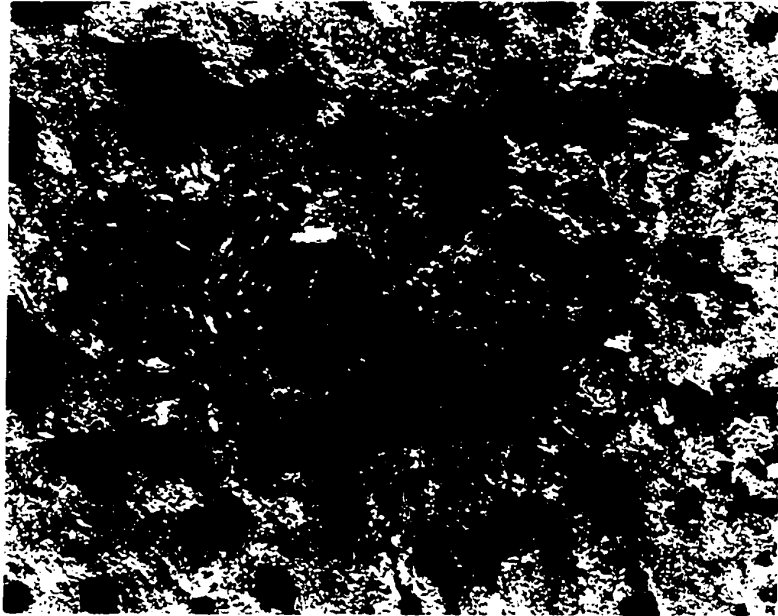


FIGURE 1. Speer RC4 graphite.  
80X

- |                           |                             |                   |
|---------------------------|-----------------------------|-------------------|
| A. propane                | F. water bath               | K. air inlet      |
| B. low pressure regulator | G. metal compound container | L. pyrometer      |
| C. dessicant              | H. inlet orifice            | M. NaOH           |
| D. manometer              | I. deposition chamber       | N. control valves |
| E. flowmeter              | J. condensing tower         | P. vacuum pump    |

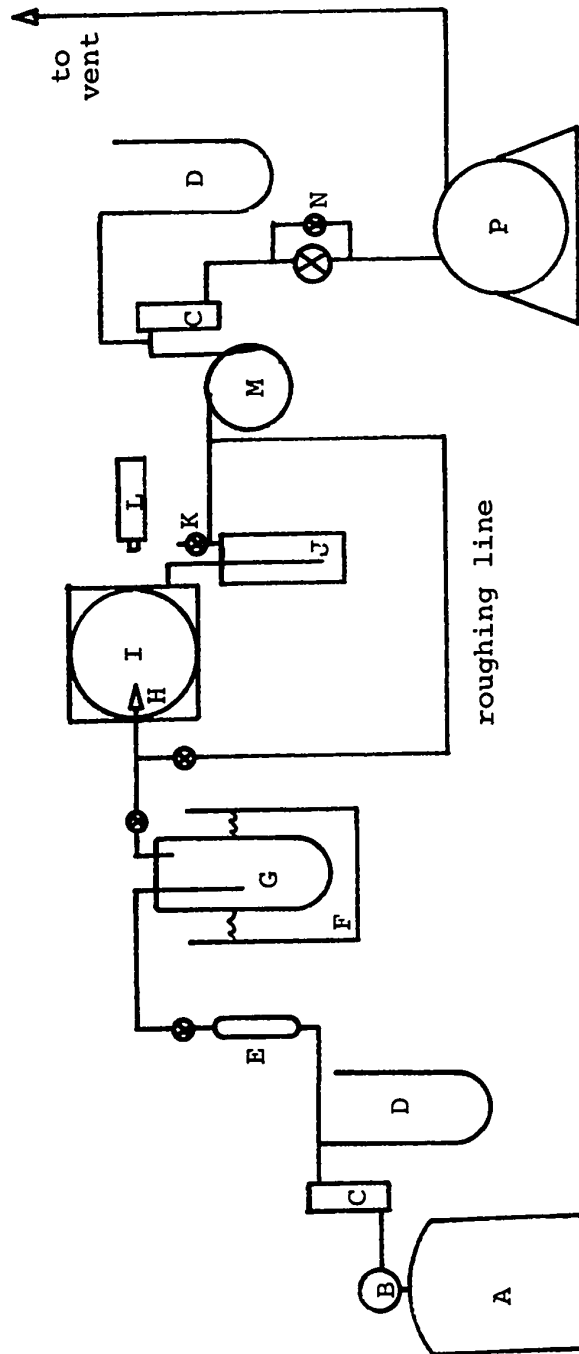


FIGURE 2. Flow sheet for pyrolytic codeposition apparatus.



FIGURE 3. Pyrolytic codeposition equipment.  
L to R: D.C. welder, pyrometer,  
deposition chamber, vacuum pump,  
constant temperature bath, mano-  
meters, propane.



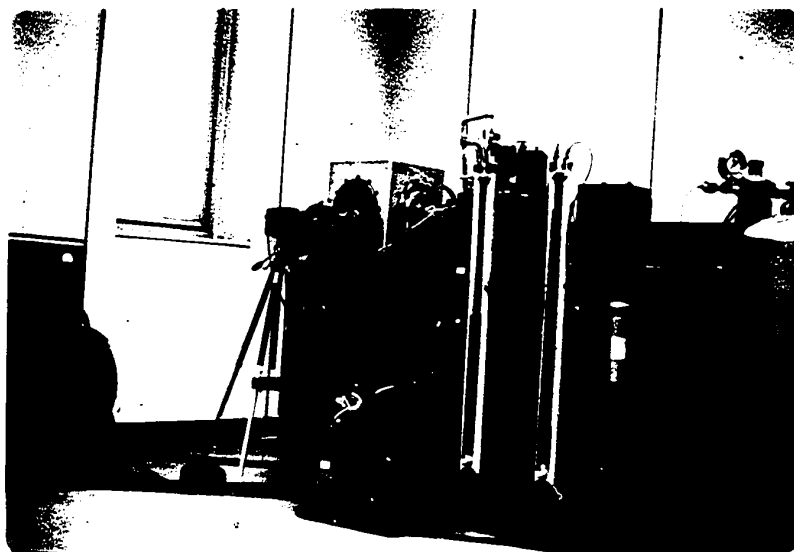


FIGURE 3. Pyrolytic codeposition equipment.  
L to R: D.C. welder, pyrometer,  
deposition chamber, vacuum pump,  
constant temperature bath, mano-  
meters, propane.

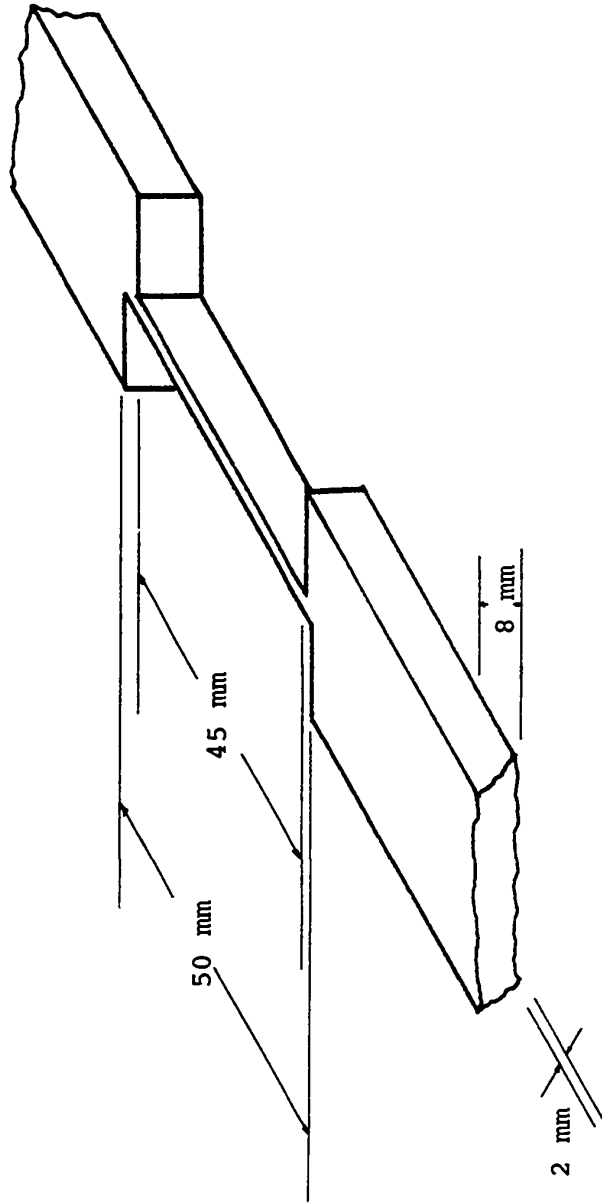


FIGURE 4. Graphite substrate design.

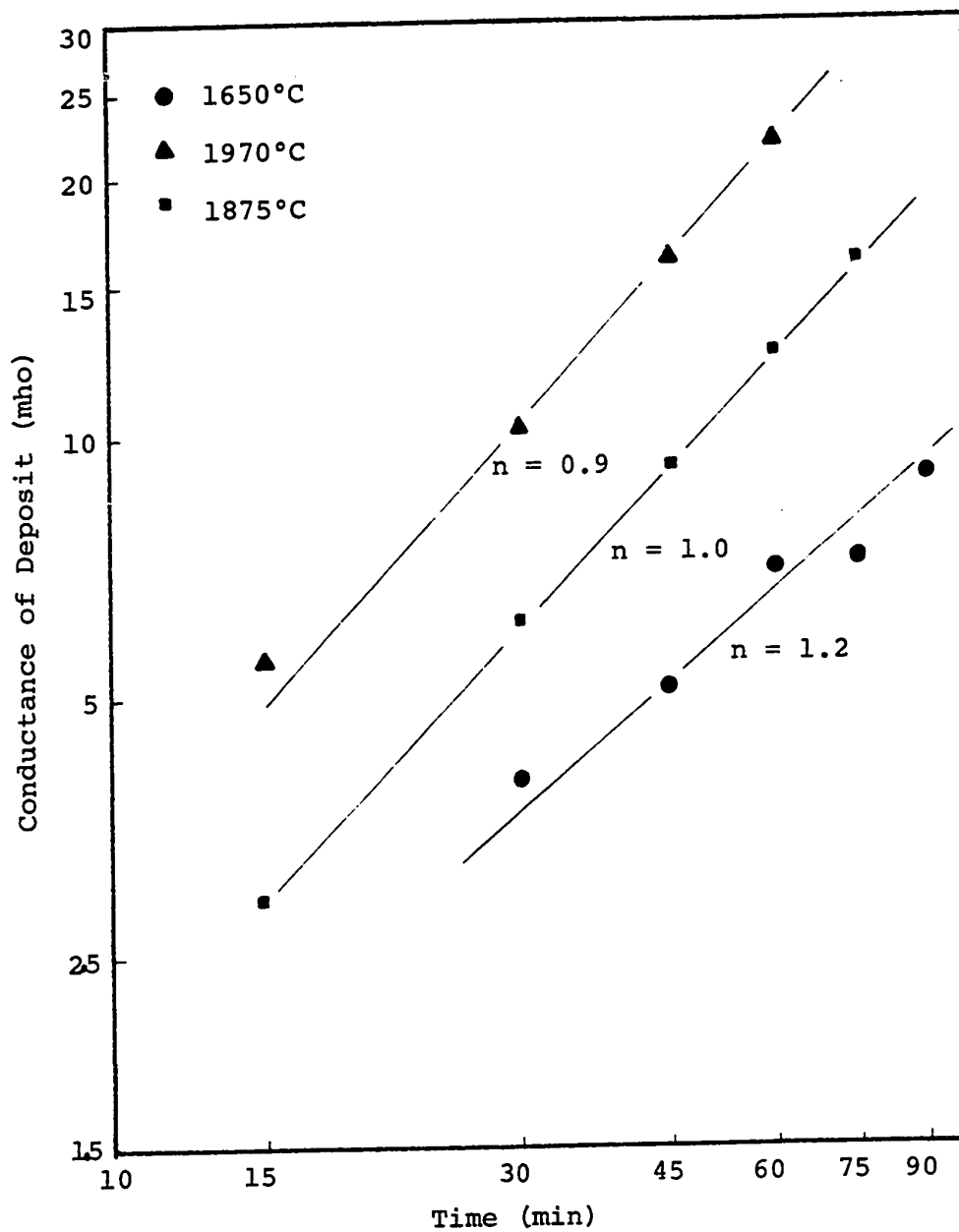


FIGURE 5. Conductance change of graphite deposit with time. Pyrolytic graphite deposited at  $5 \pm 1$  torr.

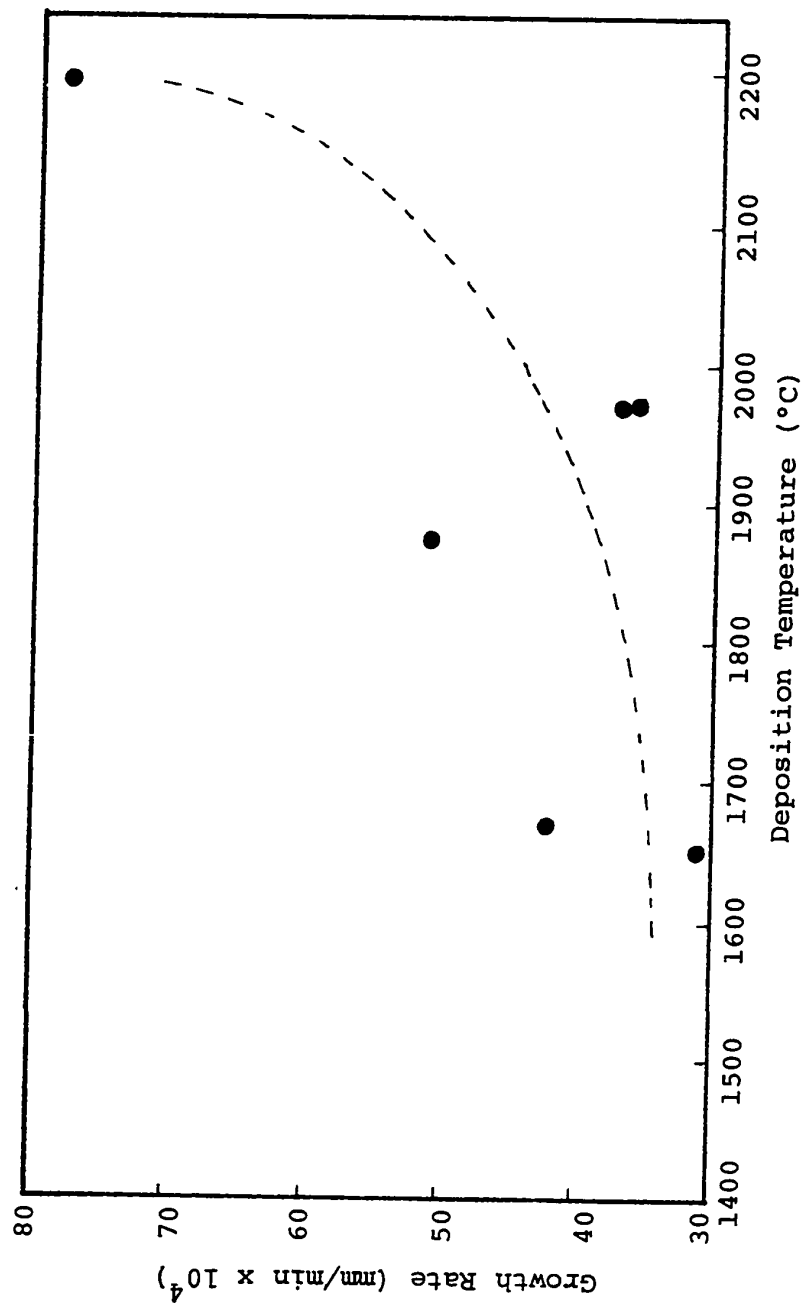


FIGURE 6. Growth rate of pyrolytic graphite as a function of deposition temperature for a deposition pressure of  $4.5 \pm 0.5$  torr.

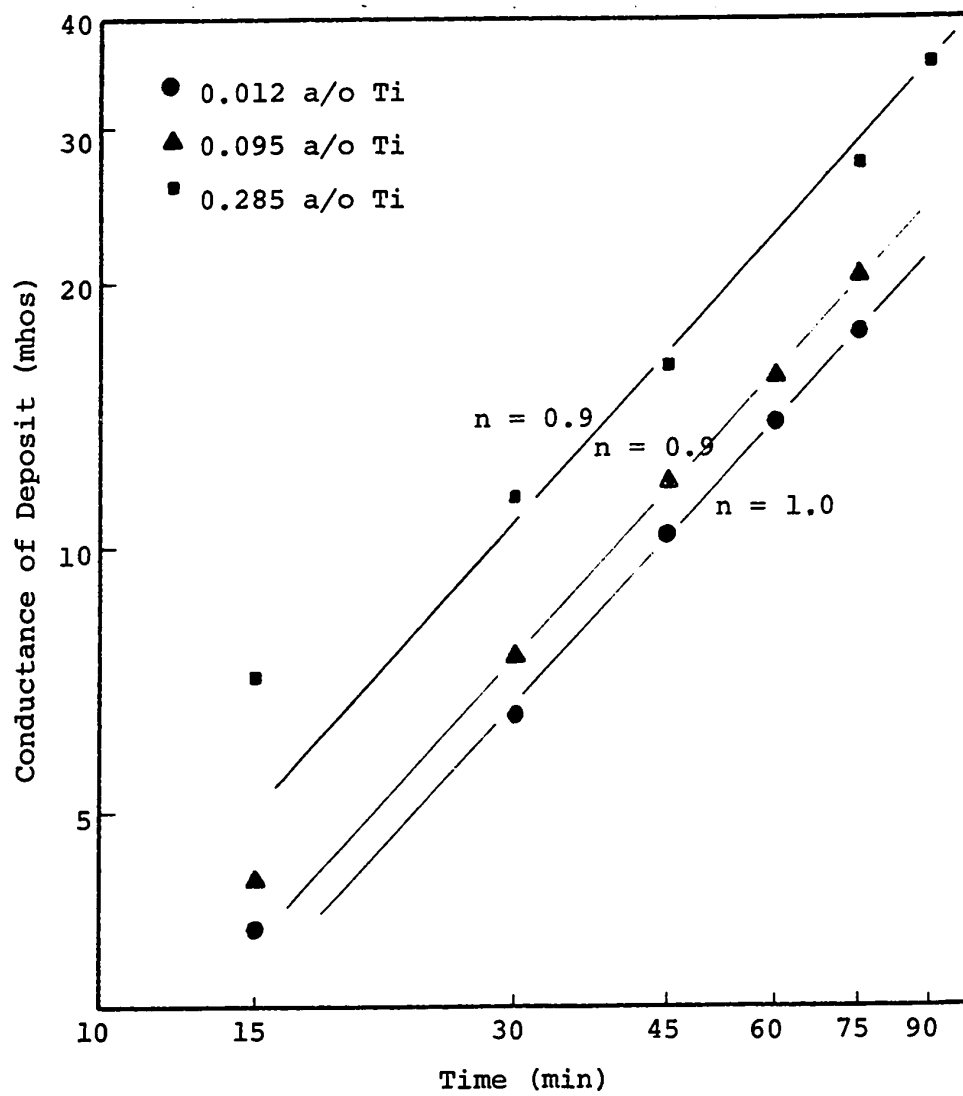


FIGURE 7. Conductance of graphite-titanium deposits formed at  $1675 \pm 75^\circ\text{C}$  and  $5 \pm 1$  torr.

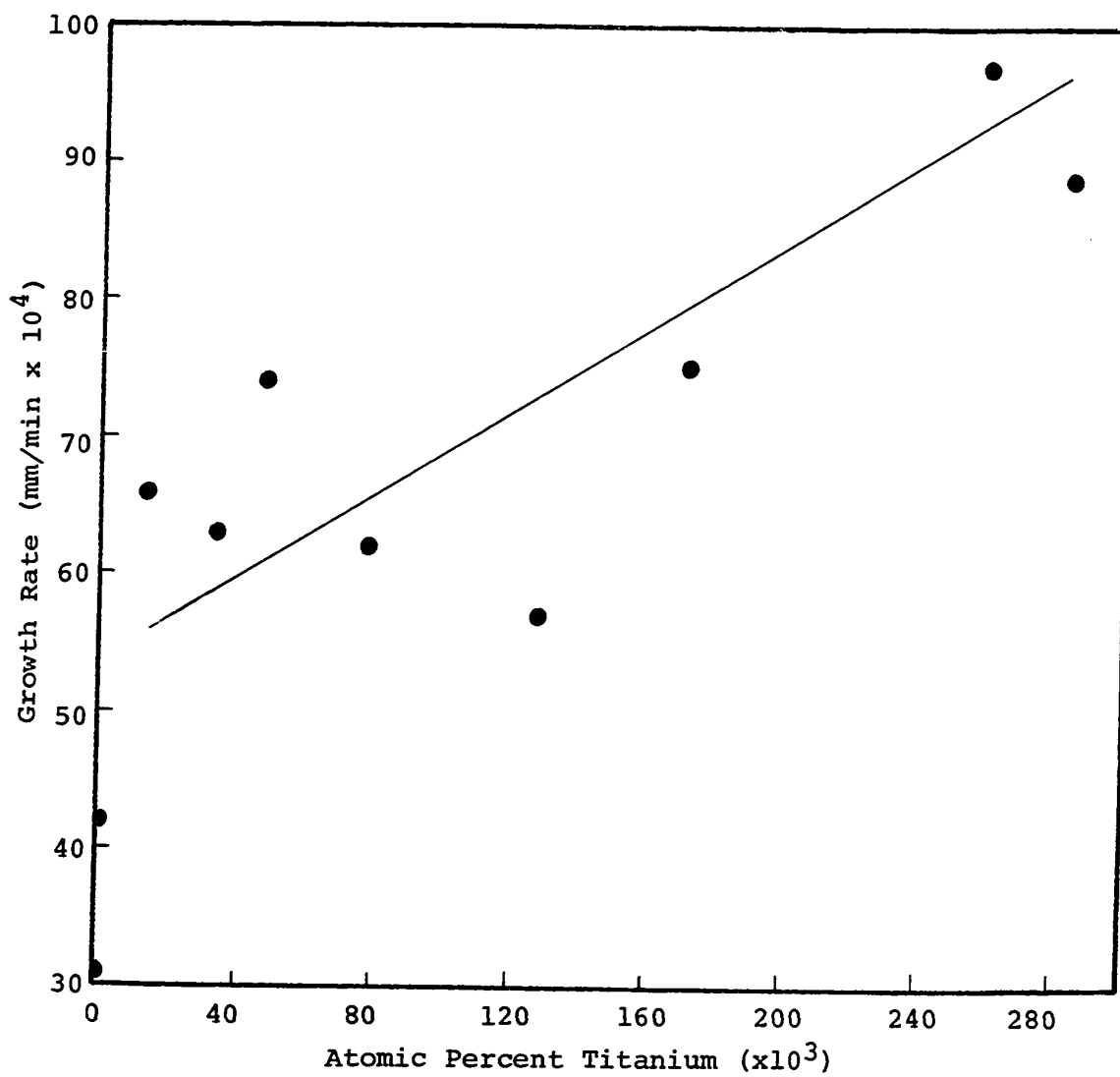


FIGURE 8. Growth rate as a function of titanium concentration for alloys formed at  $1675 \pm 75^\circ\text{C}$  and  $5 \pm 1$  torr.

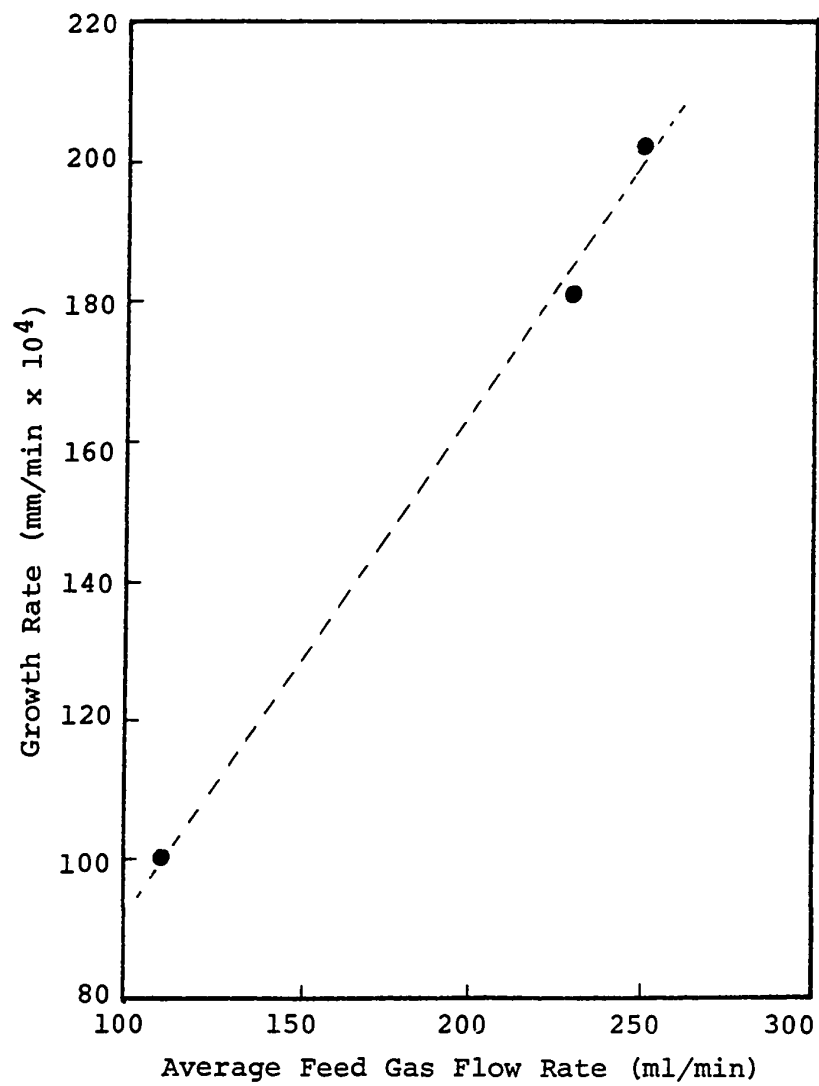


FIGURE 9. Effect of feed gas flow rate on the growth rate of pyrolytic graphite-vanadium alloys.

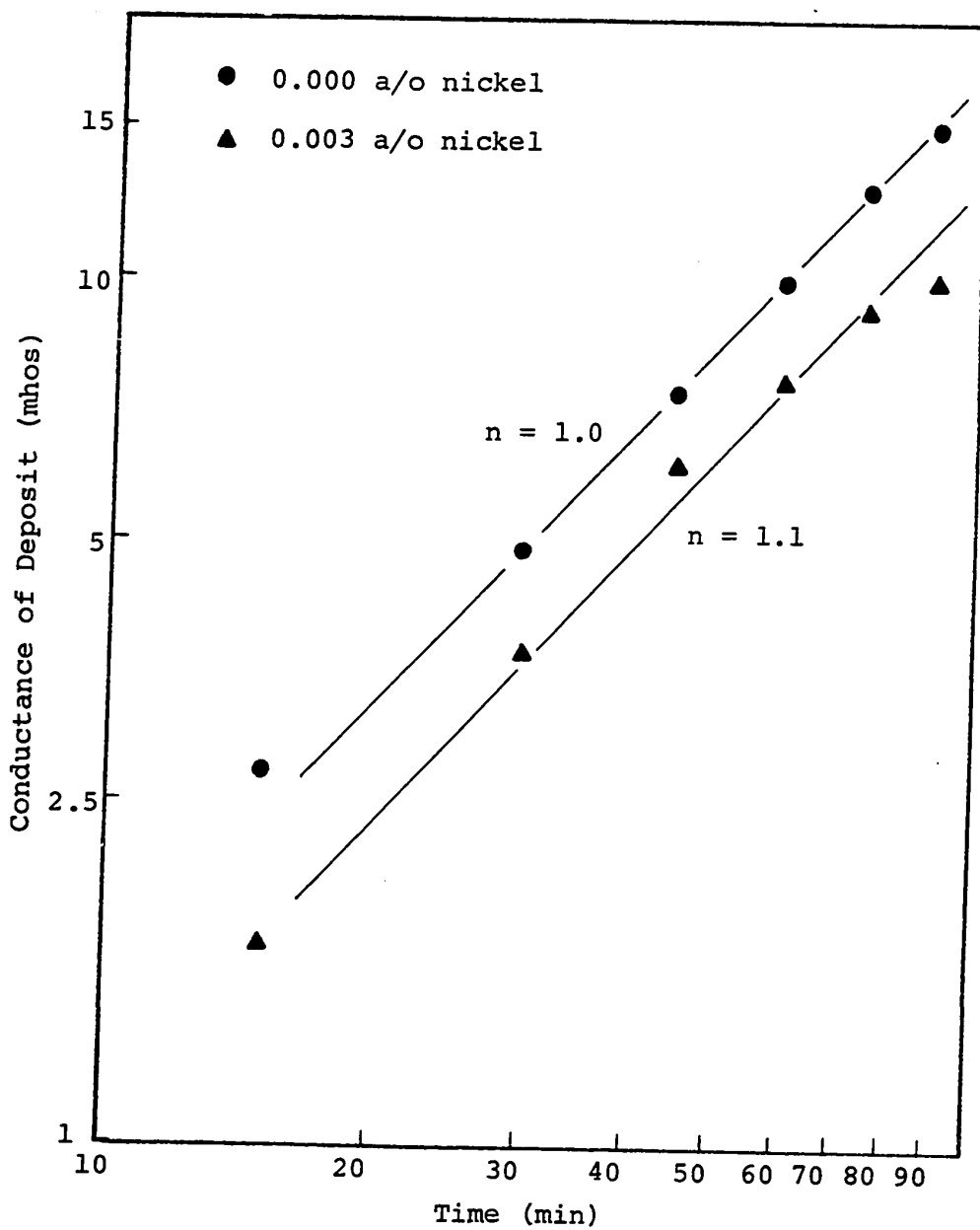


FIGURE 10. Conductance of graphite-nickel alloy deposits formed at  $1600 \pm 40^\circ\text{C}$  and  $6 \pm 0.5$  torr.



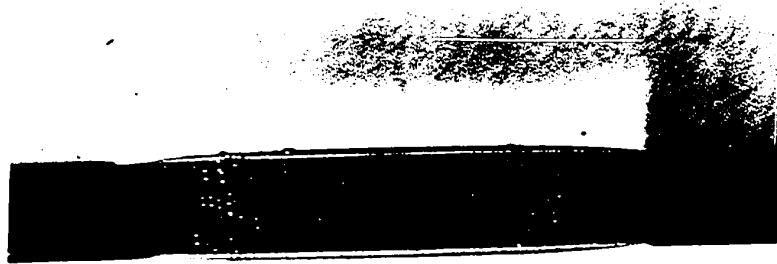


FIGURE 11. Substrate with top view of  
pyrolytic graphite deposit.  
1X

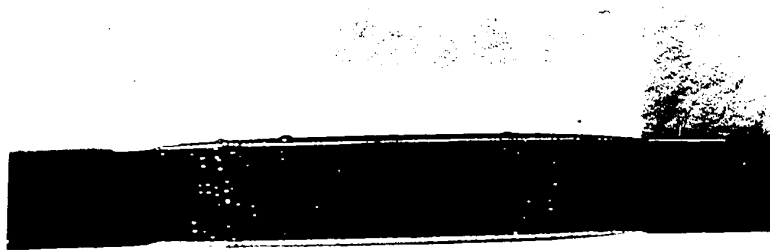


FIGURE 11. Substrate with top view of  
pyrolytic graphite deposit.  
1X

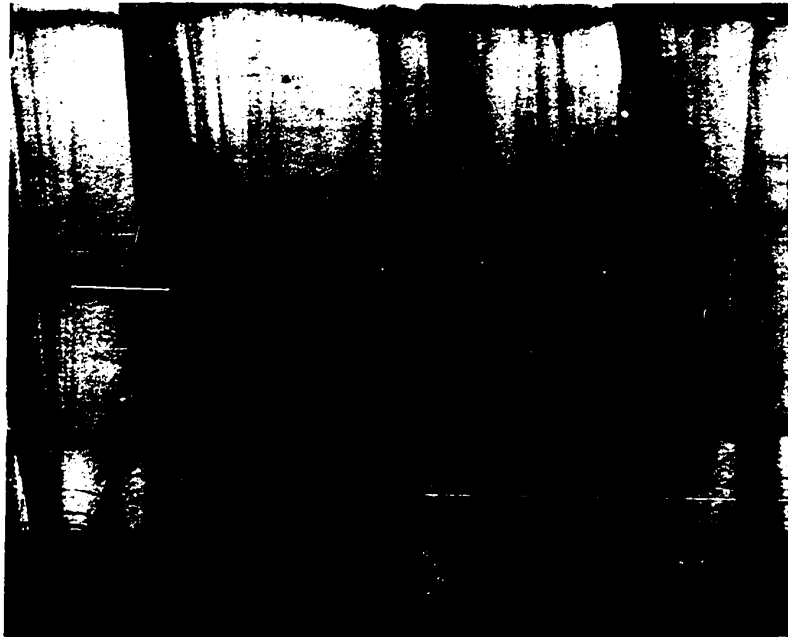


FIGURE 12. Singularly nucleated pyrolytic graphite.  
100X polarized light.

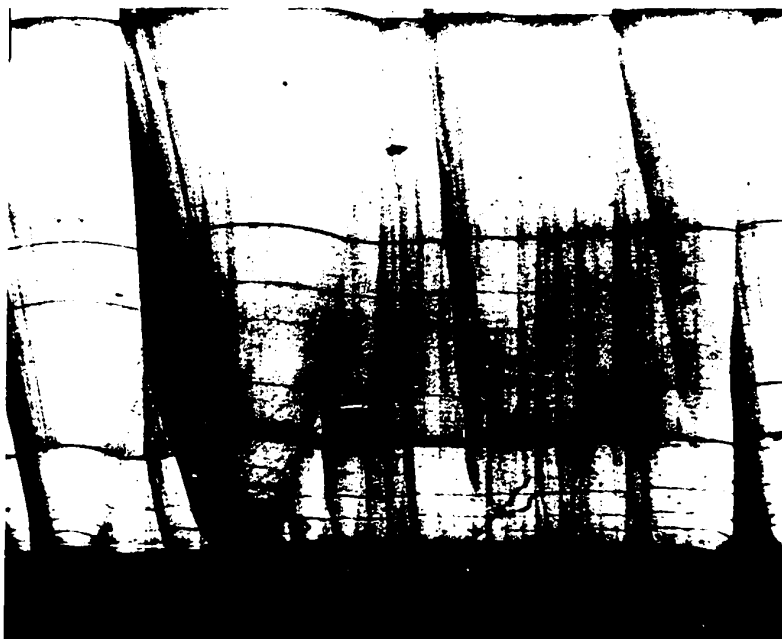


FIGURE 12. Singularly nucleated pyrolytic graphite.  
100X polarized light.

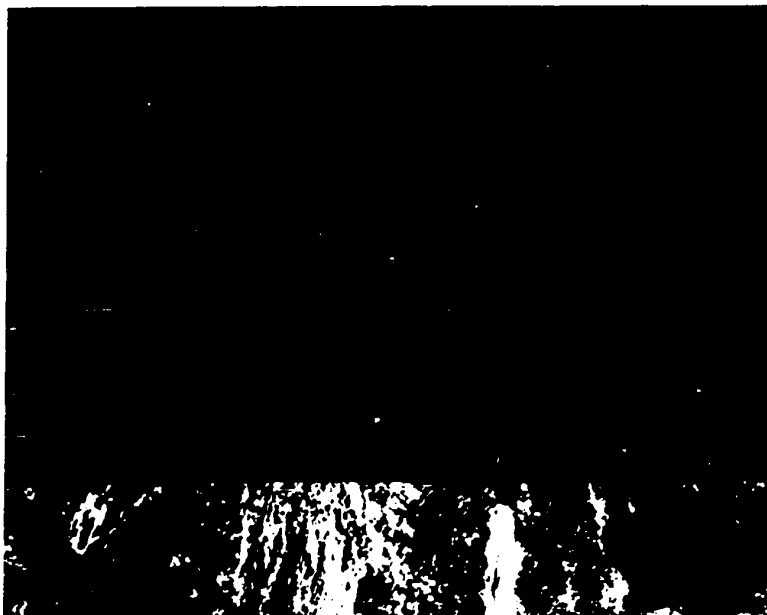


FIGURE 13. Polynucleated pyrolytic graphite.  
80X polarized light.

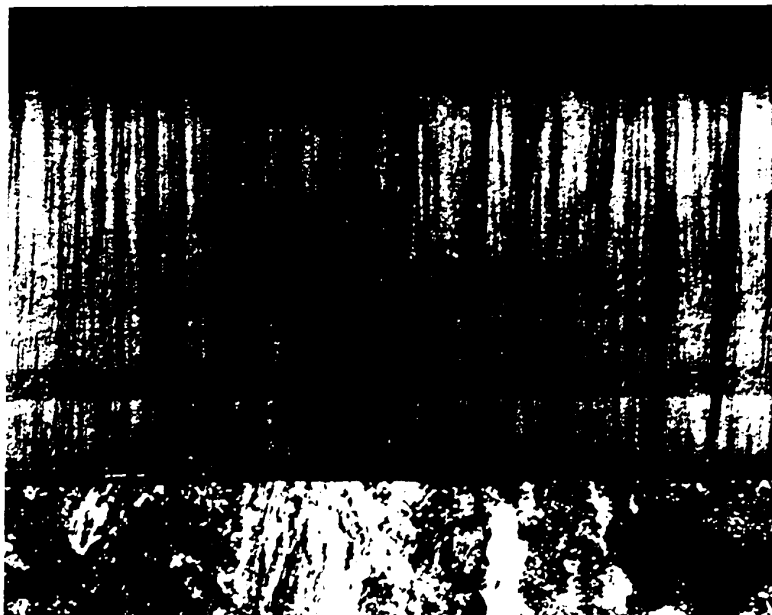


FIGURE 13. Polynucleated pyrolytic graphite.  
80X polarized light.

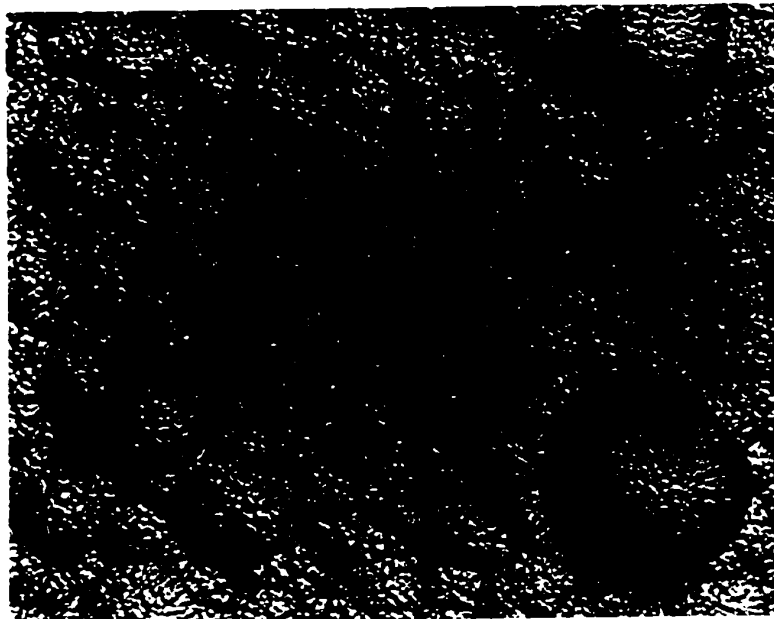


FIGURE 14. Deposition surface parallel  
to deposition substrate.  
Mechanically polished. 100X

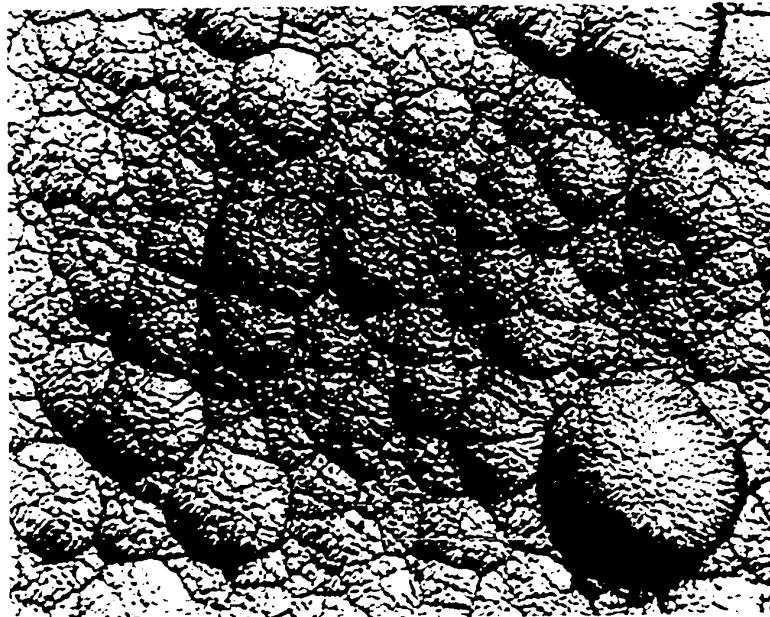


FIGURE 14. Deposition surface parallel  
to deposition substrate.  
Mechanically polished. 100X



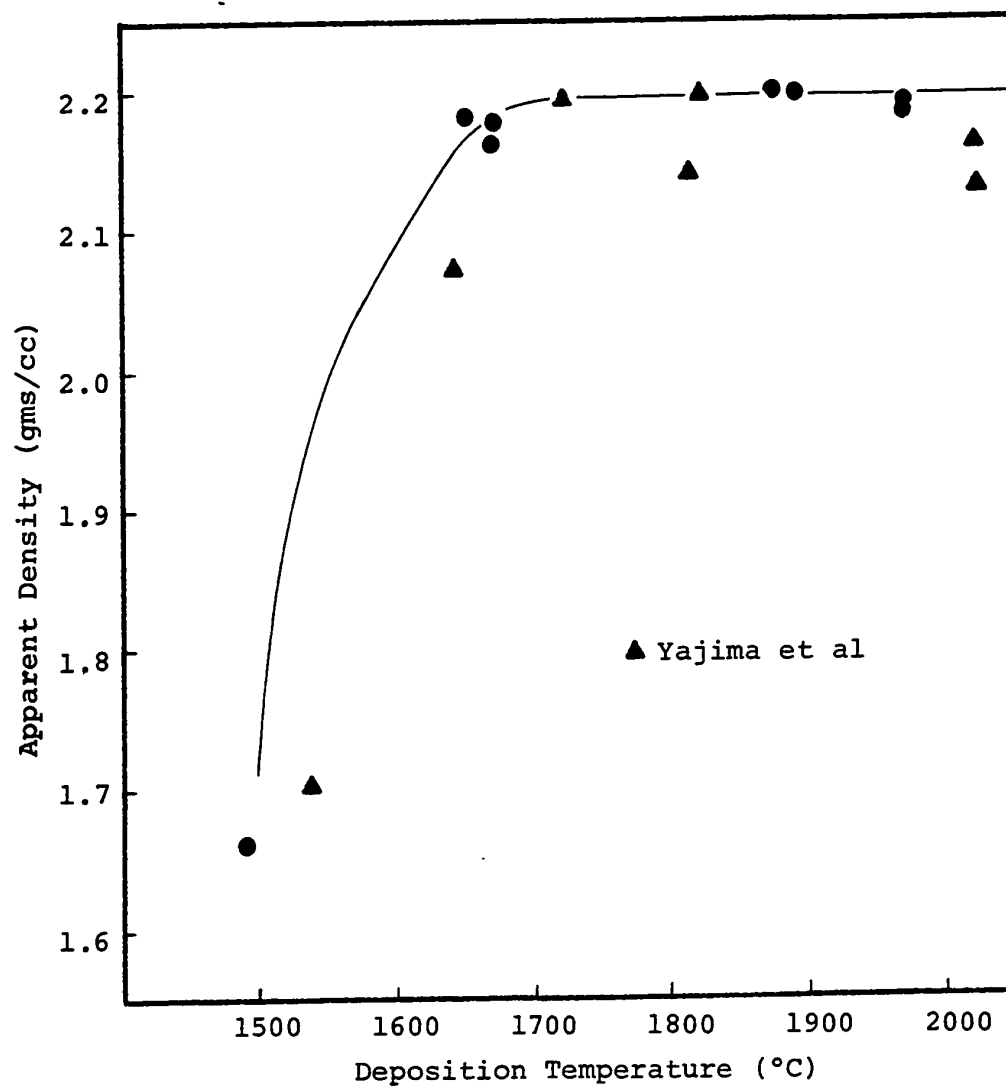


FIGURE 15. Apparent density of pyrolytic graphite as a function of deposition temperature. Deposition pressure constant at  $4.5 \pm 0.5$  torr.

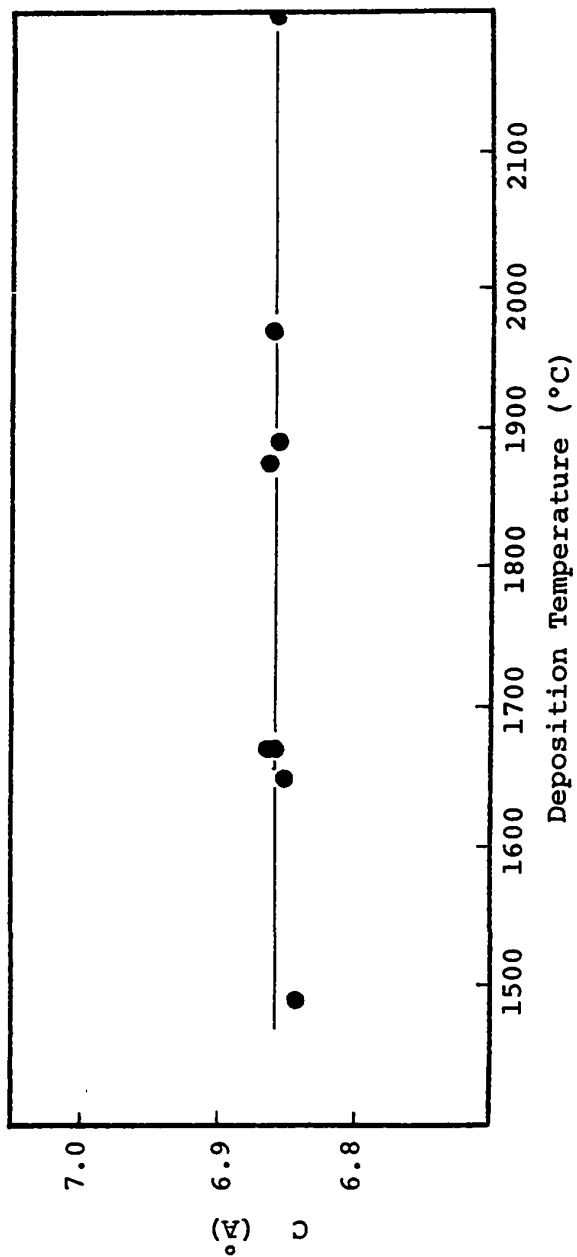


FIGURE 16. Lattice constant,  $C$ , as a function of deposition temperature for pyrolytic graphite formed at a pressure of  $4.5 \pm 0.5$  torr.

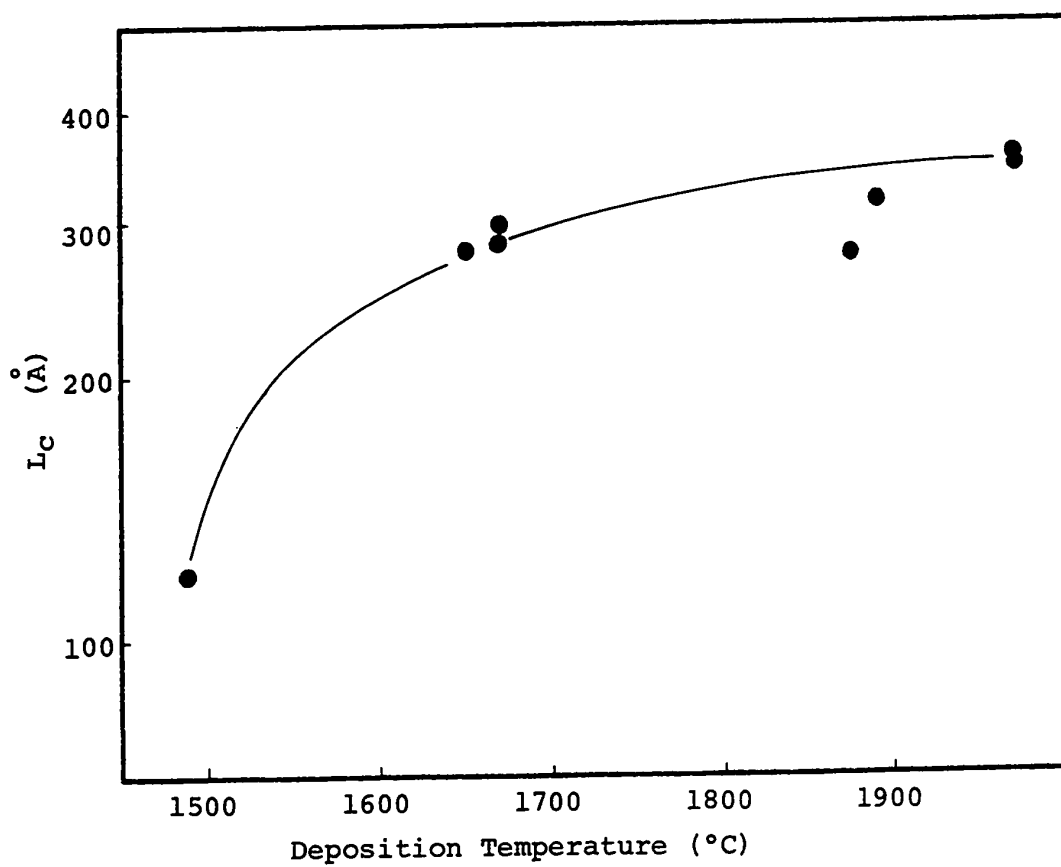


FIGURE 17. Crystallite size,  $L_c$ , as a function of deposition temperature of pyrolytic graphite formed at  $4.5 \pm 0.5$  torr.

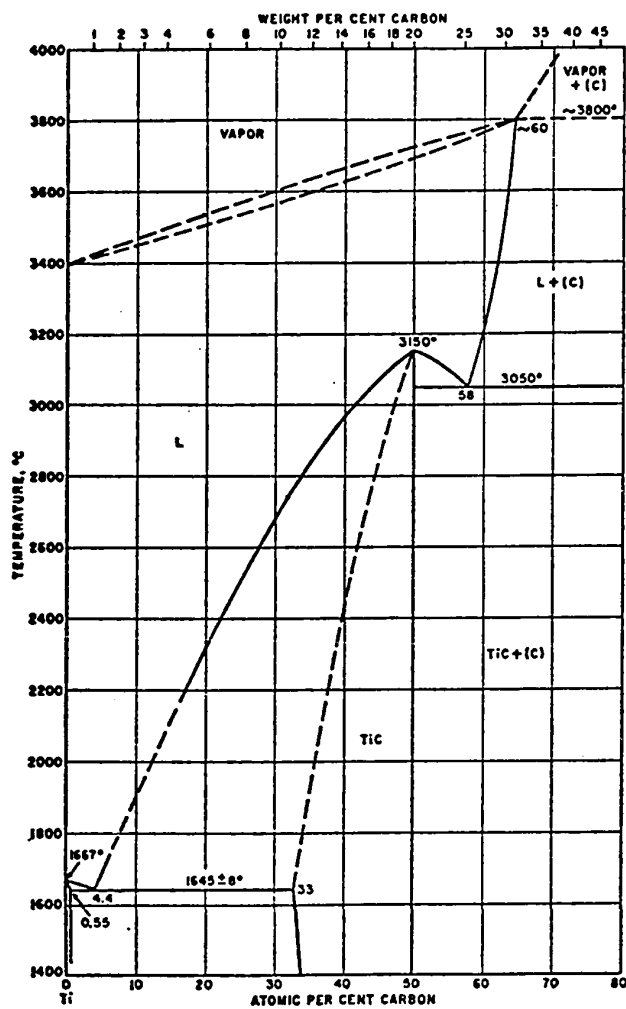


FIGURE 18. Carbon-titanium phase diagram.

Taken from R.P. Elliot, Constitution of Binary Alloys, First Supplement, McGraw Hill Co., New York, 1965.



FIGURE 19. Singularly nucleated alloy of pyrolytic graphite and 0.285 a/o titanium formed at  $1625 \pm 25^\circ\text{C}$  and 4 torr. 80X polarized light.

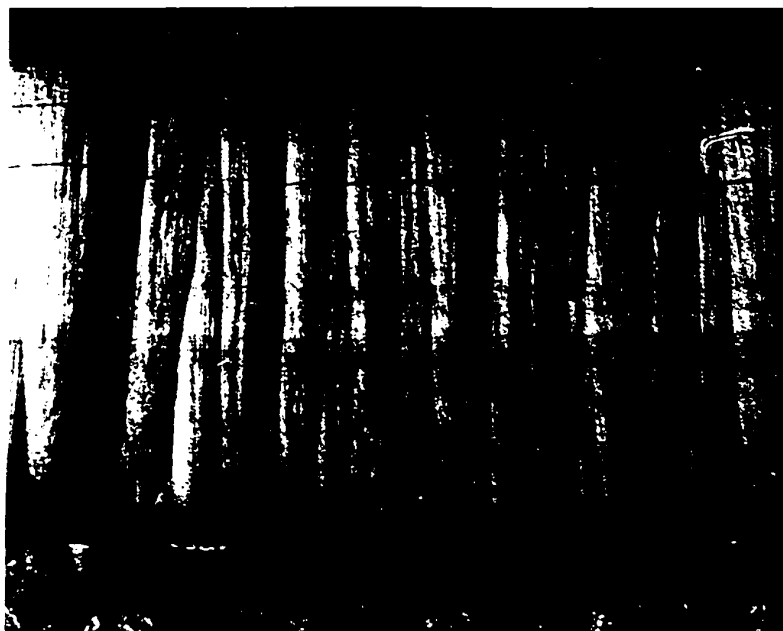


FIGURE 19. Singularly nucleated alloy of pyrolytic graphite and 0.285 a/o titanium formed at 1625 ± 25°C and 4 torr. 80X polarized light.



FIGURE 20. Singularly nucleated alloy of pyrolytic graphite and 0.002 a/o titanium formed at  $1980 \pm 30^\circ\text{C}$  and 4 torr. 80X polarized light.

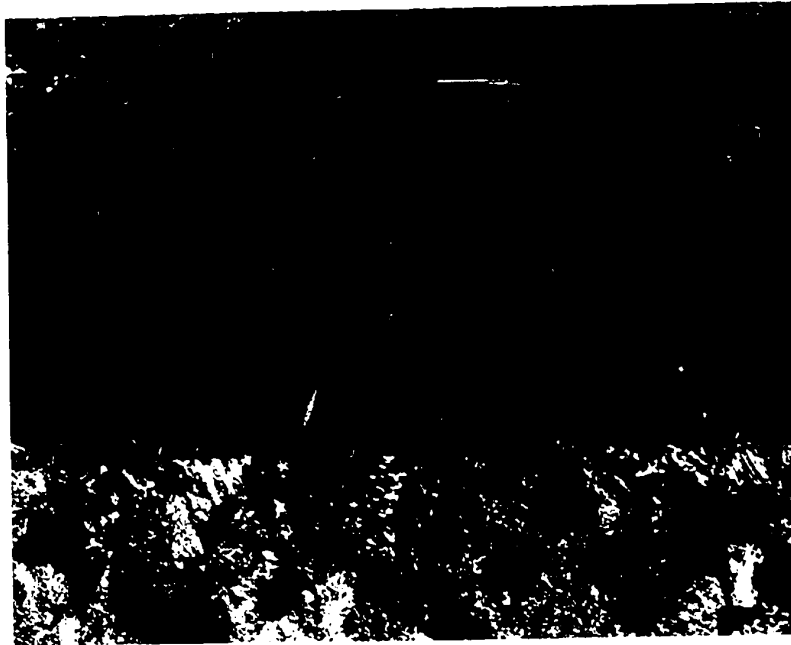


FIGURE 20. Singularly nucleated alloy of pyrolytic graphite and 0.002 a/o titanium formed at  $1980 \pm 30^\circ\text{C}$  and 4 torr. 80X polarized light.



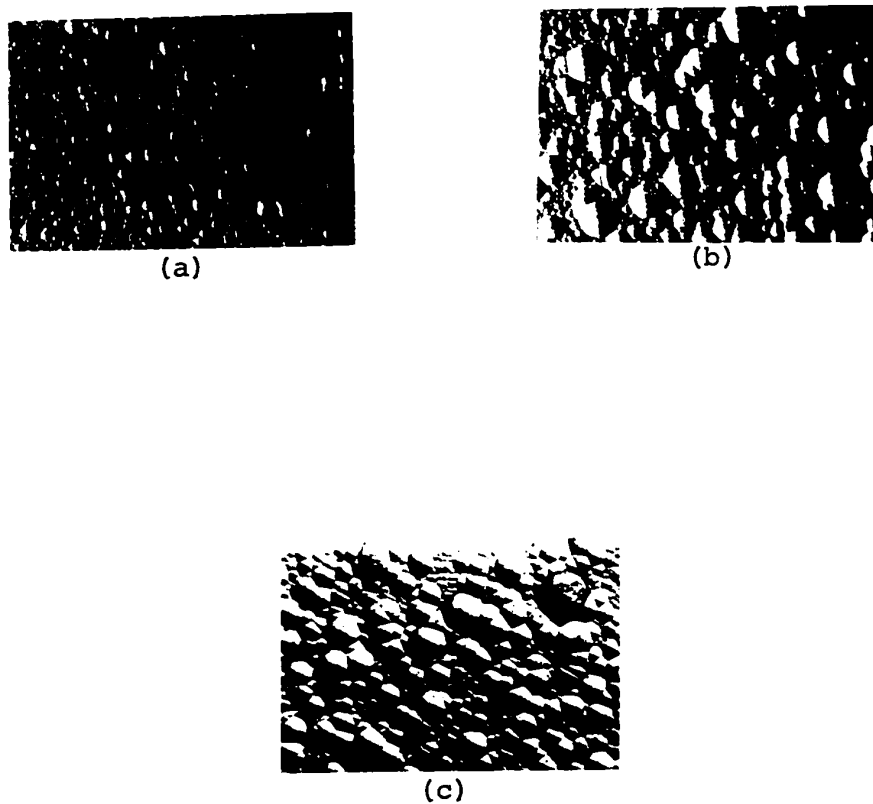


FIGURE 21. Top view of basal plane growth cones in pyrolytic graphite-titanium alloys deposited at  $1675 \pm 75^\circ\text{C}$  and  $5 \pm 1$  torr.

- (a) 0.012 a/o titanium
- (b) 0.078 a/o titanium
- (c) 0.187 a/o titanium

6X

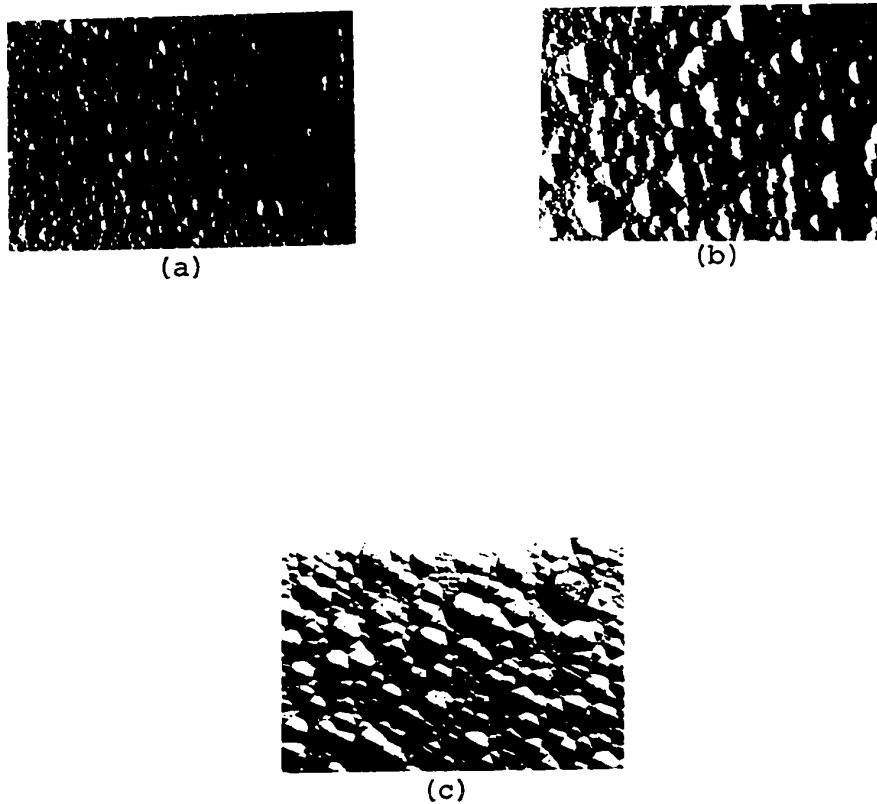


FIGURE 21. Top view of basal plane growth cones in pyrolytic graphite-titanium alloys deposited at  $1675 \pm 75^\circ\text{C}$  and  $5 \pm 1$  torr.

- (a) 0.012 a/o titanium
- (b) 0.078 a/o titanium
- (c) 0.187 a/o titanium

6X



FIGURE 22. Precipitate in pyrolytic graphite-0.012 a/o titanium alloy deposited at  $1660 \pm 20^\circ\text{C}$  and 5 torr.

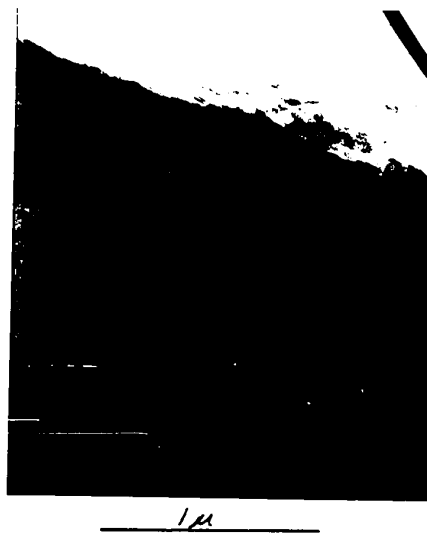


FIGURE 22. Precipitate in pyrolytic graphite-  
0.012 a/o titanium alloy deposited  
at  $1660 \pm 20^\circ\text{C}$  and 5 torr.

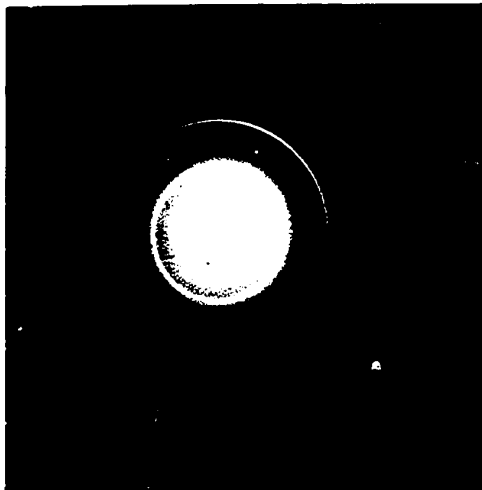


(a)

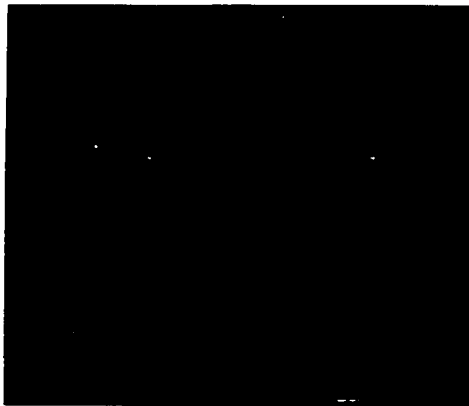


(b)

FIGURE 23. Pyrolytic graphite-0.285 a/o titanium alloy formed at  $1625 \pm 25^\circ\text{C}$  and 4 torr.  
(a) Diffraction pattern.  
(b) Area from which diffraction pattern obtained.



(a)



(b)

FIGURE 23. Pyrolytic graphite-0.235 a/o titanium alloy formed at  $1625 \pm 25^\circ\text{C}$  and 4 torr.  
(a) Diffraction pattern.  
(b) Area from which diffraction pattern obtained.

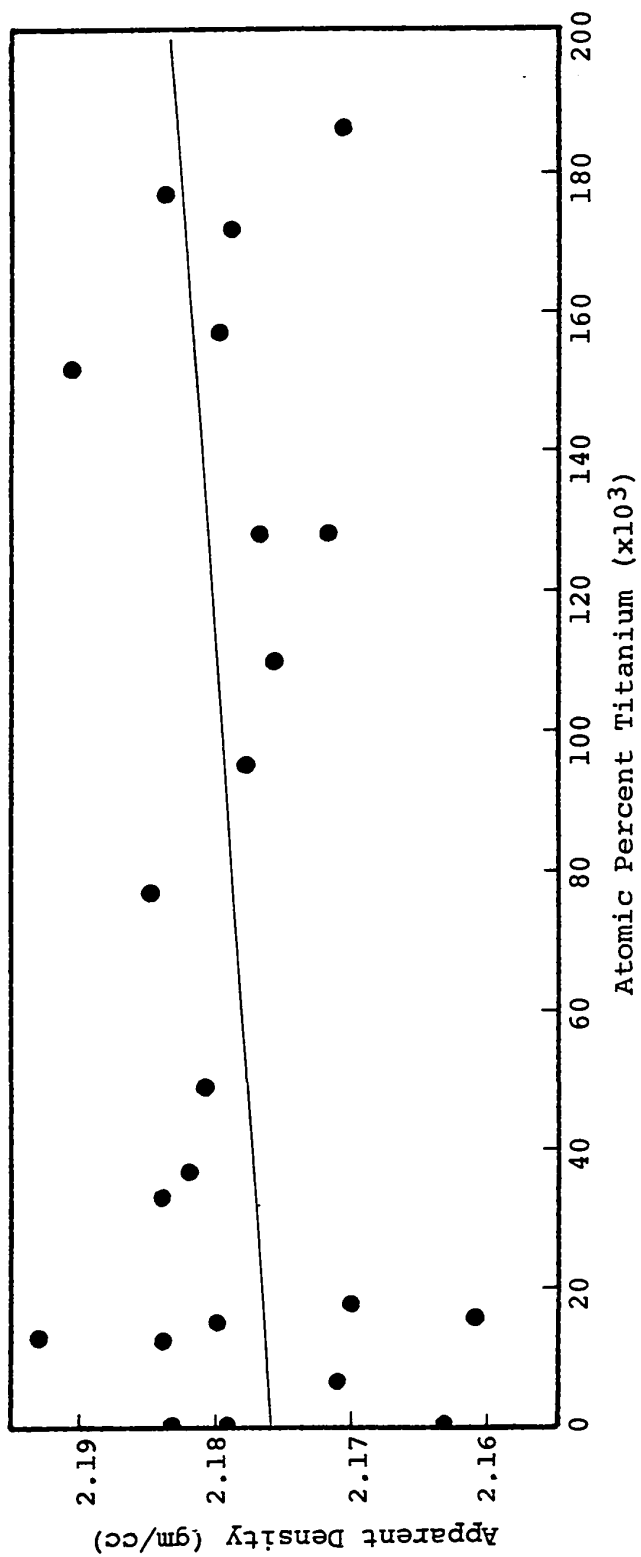


FIGURE 24. Apparent density of alloy deposits as a function of titanium concentration. Deposits formed at  $1675 \pm 75^\circ\text{C}$  and  $5 \pm 1$  torr.

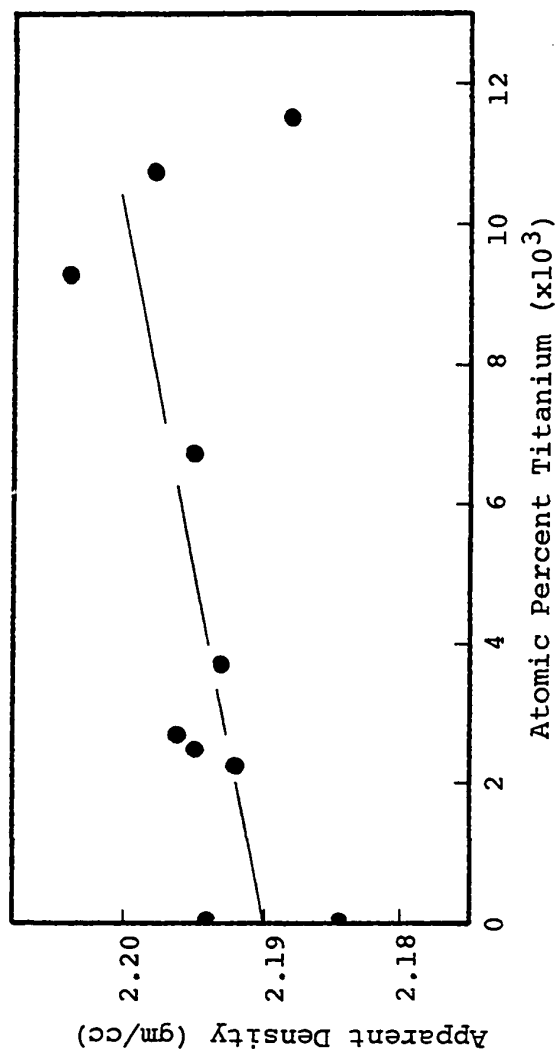


FIGURE 25. Apparent density of alloy deposits as a function of titanium concentration. Deposits formed at  $1975 \pm 35^\circ\text{C}$  and  $5.5 \pm 1.5$  torr.



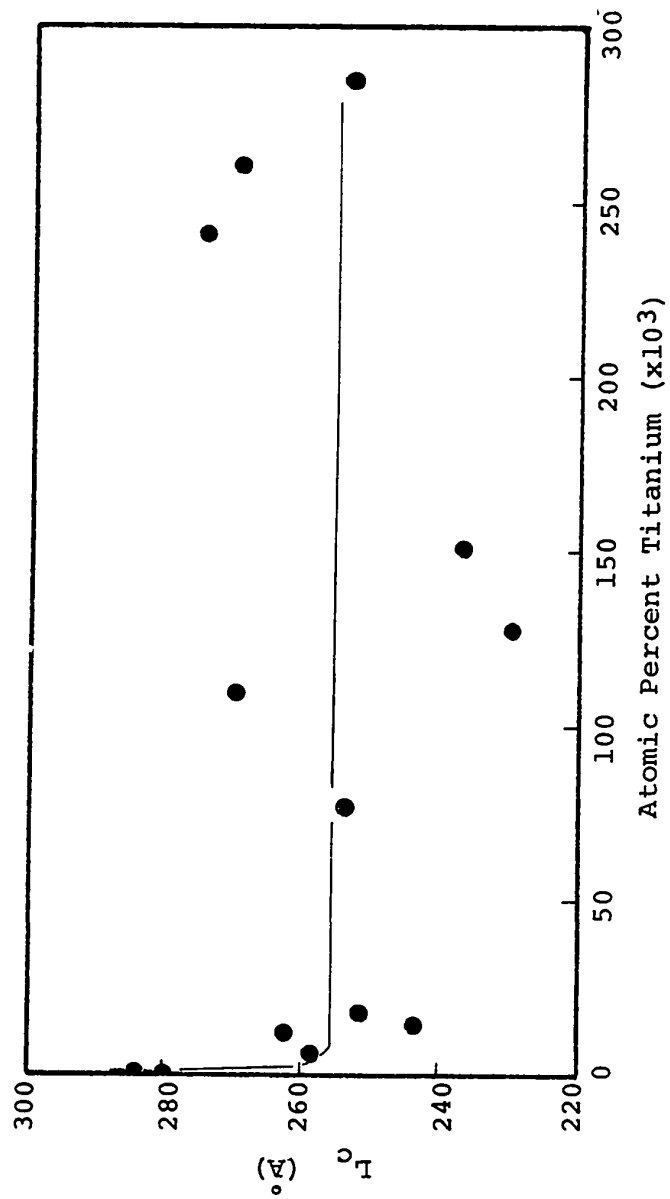


FIGURE 26. Crystallite height,  $L_c$ , as a function of composition. Alloys formed at  $1675 \pm 75^\circ\text{C}$  and  $5 \pm 1$  torr.

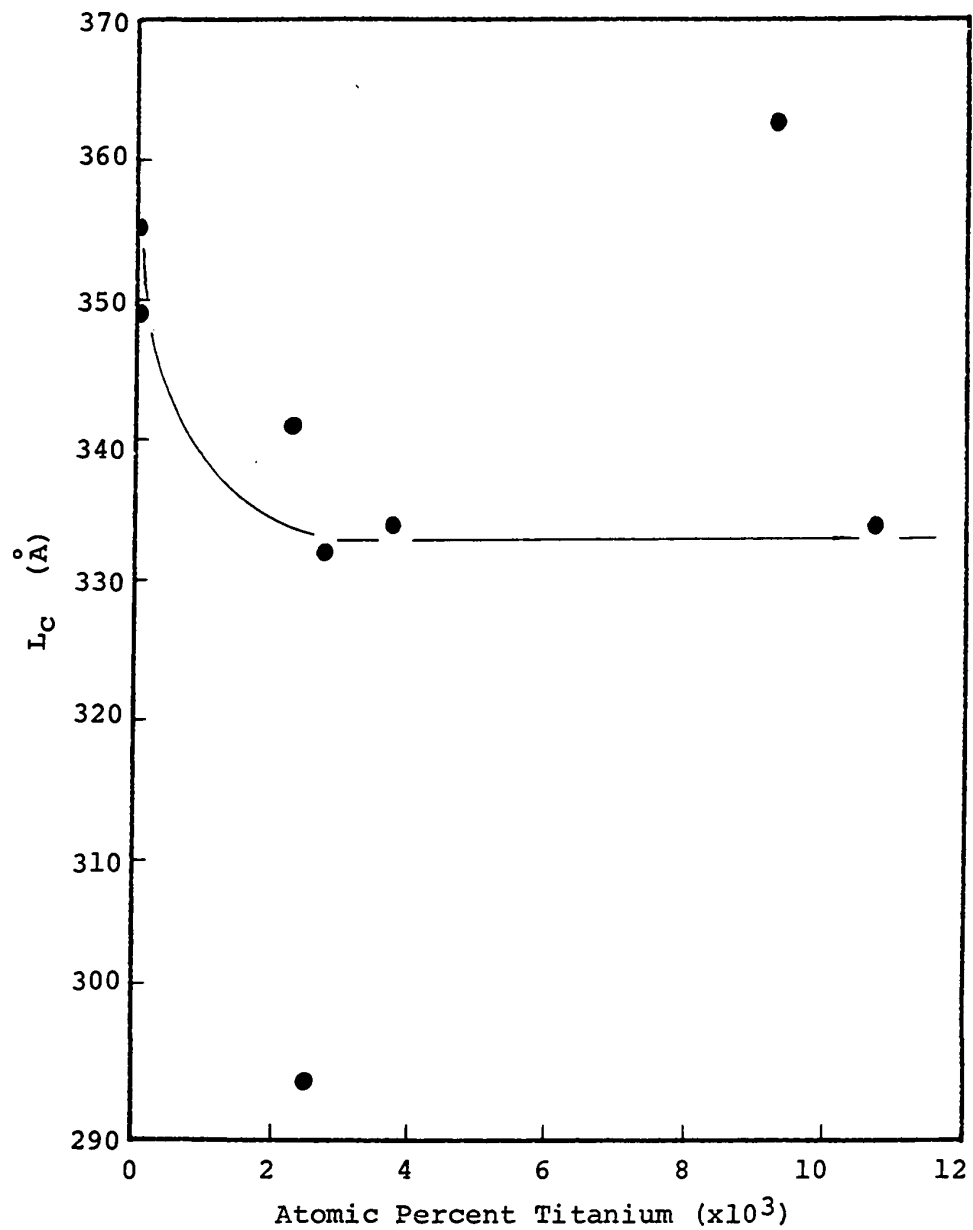


FIGURE 27. Crystallite height,  $L_c$ , as a function of titanium concentration. Alloys formed at  $1975 \pm 35^\circ\text{C}$  and  $5.5 \pm 1.5$  torr.

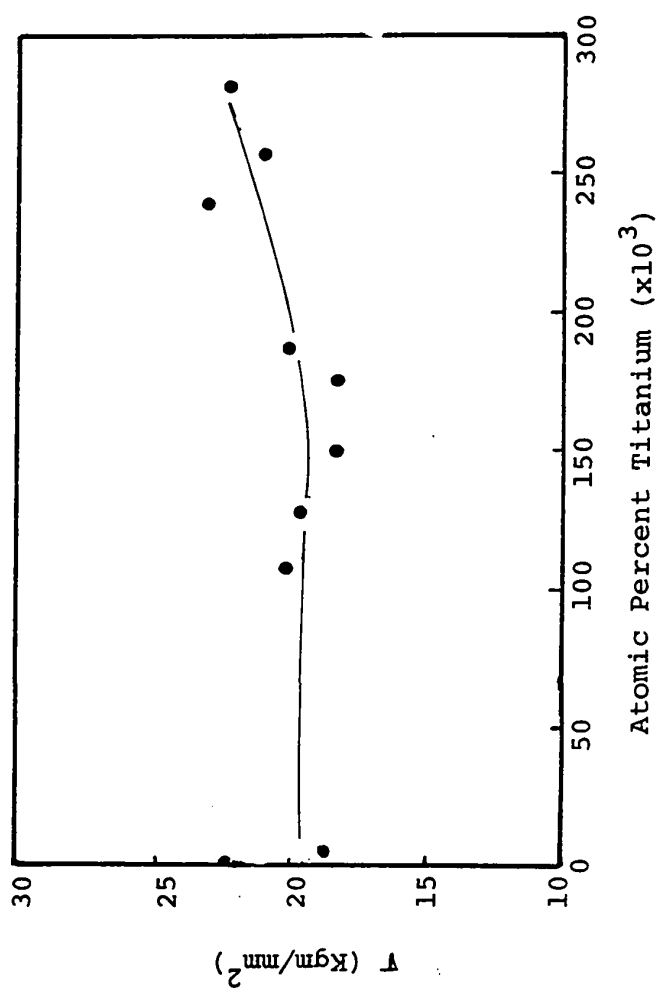


FIGURE 28. Bend Strength,  $\sigma$ , as a function of composition for alloys formed at  $1675 \pm 75^\circ\text{C}$  and  $5 \pm 1$  torr.

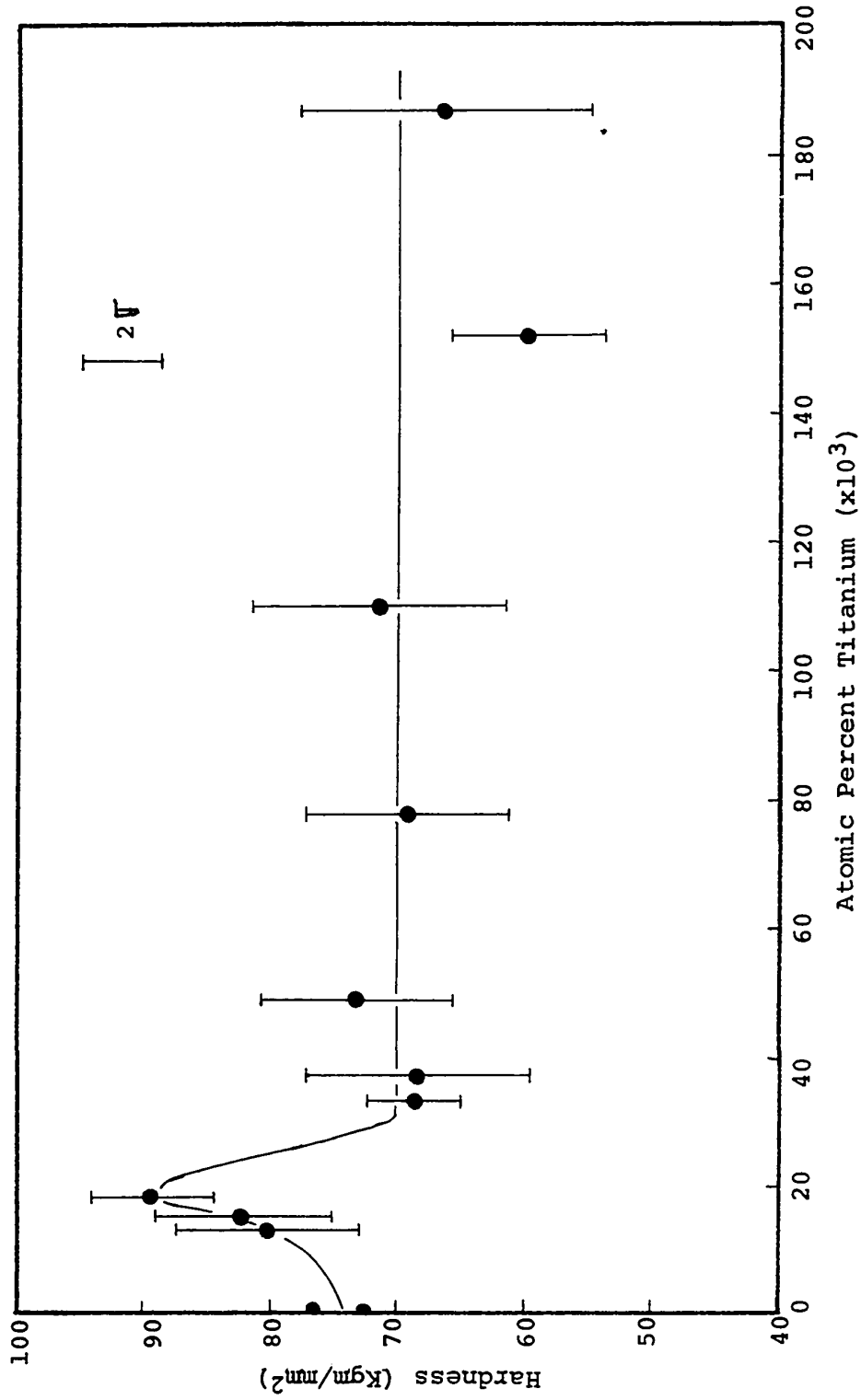


FIGURE 29. Microhardness on planes perpendicular to basal planes for alloys formed at  $1675 \pm 75^\circ\text{C}$  and  $5 \pm 1$  torr.

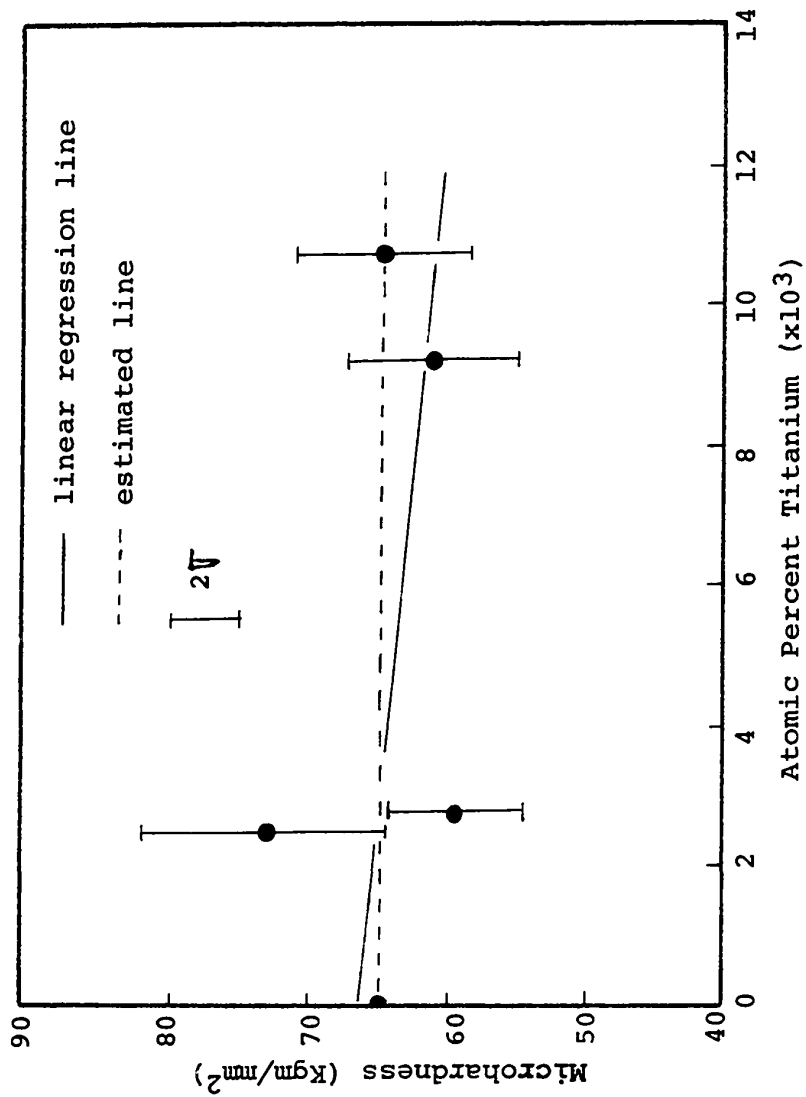


FIGURE 30. Microhardness on planes perpendicular to basal planes for alloys formed at  $1975 \pm 35^\circ\text{C}$  and  $5.5 \pm 1.5$  torr.

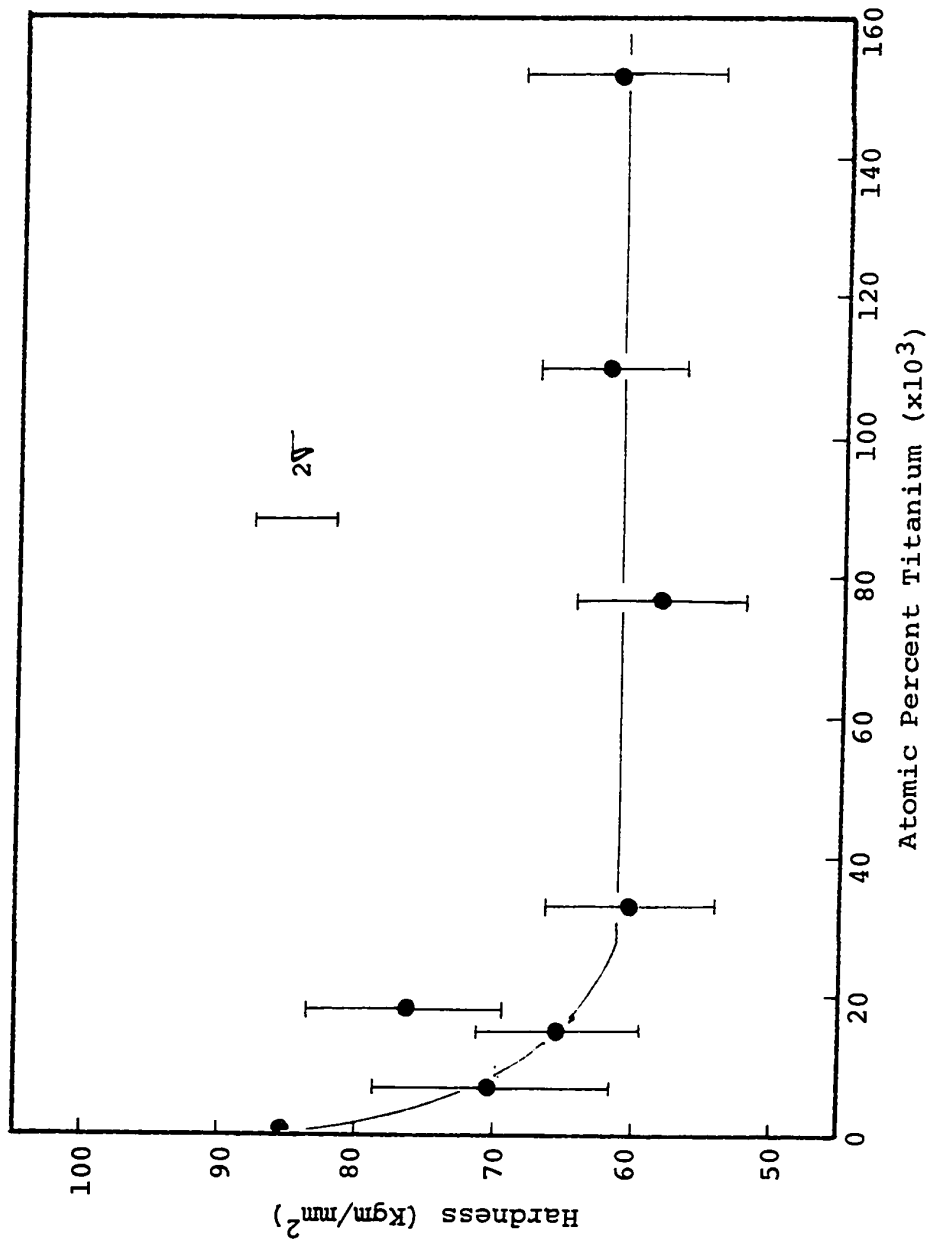


FIGURE 31. Microhardness on basal planes for alloys formed at  $1675 \pm 75^\circ\text{C}$  and  $5 \pm 1$  torr.

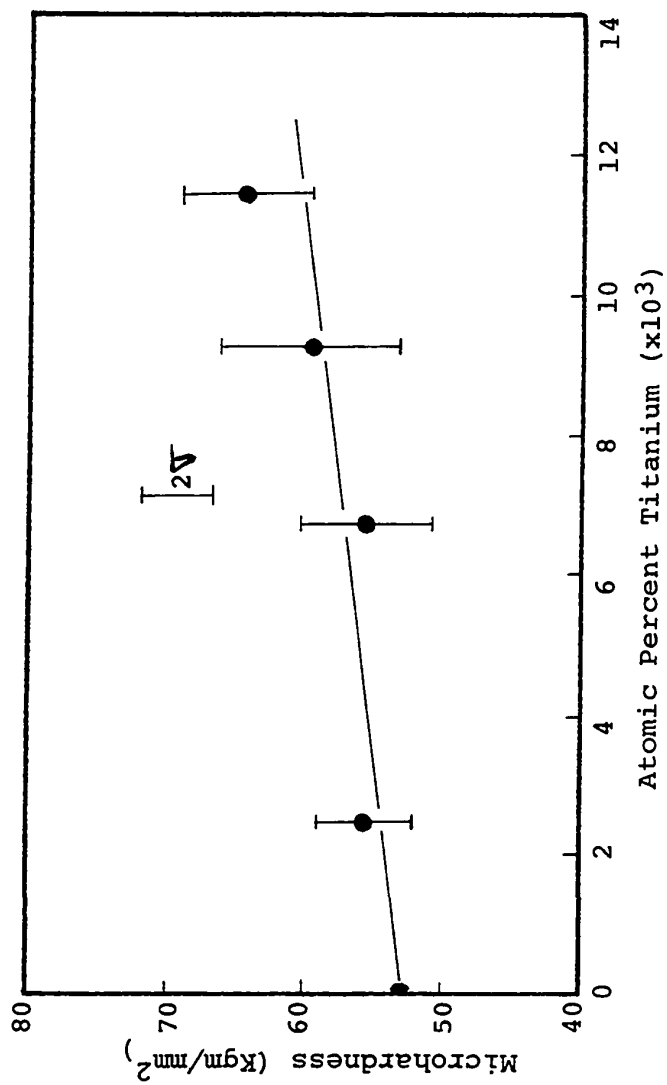


FIGURE 32. Microhardness on basal planes for alloys formed at  $1975 \pm 35^\circ\text{C}$  and  $5.5 \pm 1.5$  torr.



FIGURE 33. Electron microprobe scan on planes perpendicular to basal planes of a pyrolytic graphite-0.037 a/o titanium alloy deposited at  $1675 \pm 55^\circ\text{C}$  and 5 torr. Approximately 150X



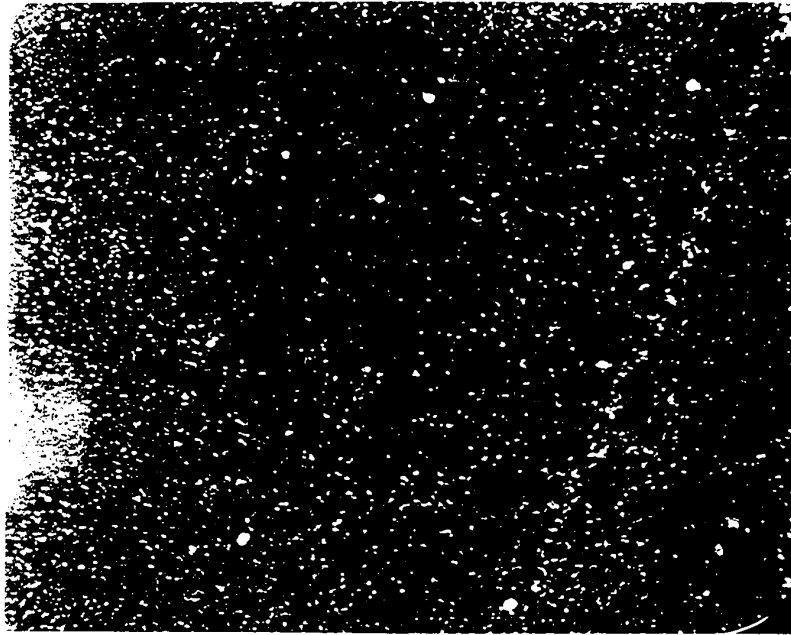


Figure 10. Electron micrograph of a polymer structure, showing a dense, granular morphology. The image displays numerous small, bright, irregularly shaped particles or clusters, characteristic of a highly textured or porous material.

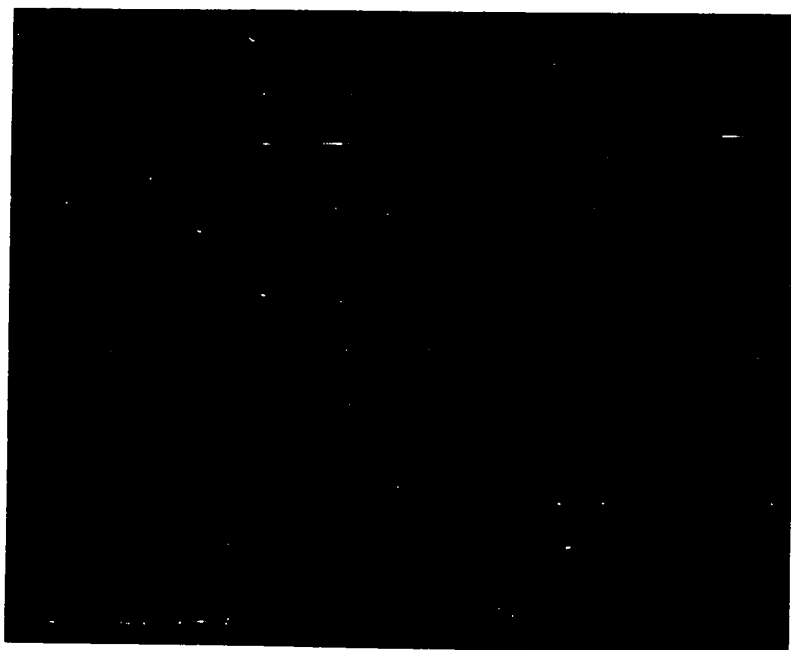


FIGURE 34. Electron microprobe scan on basal planes of a pyrolytic graphite-0.18 a/o titanium alloy deposited at  $1650 \pm 20^\circ\text{C}$  and 5 torr. Approximately 1,000X.

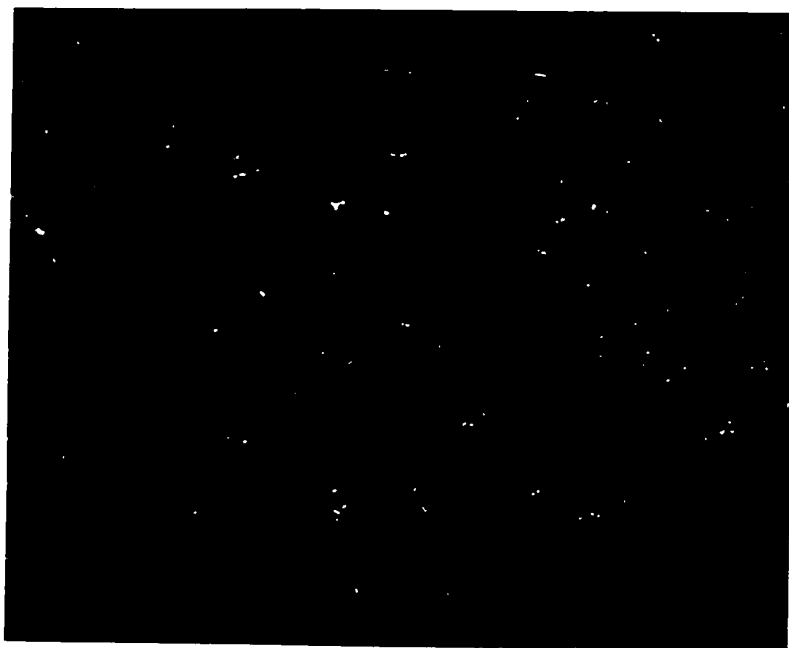


FIGURE 34. Electron microprobe scan on basal planes of a pyrolytic graphite-0.18 a/o titanium alloy deposited at  $1650 \pm 20^\circ\text{C}$  and 5 torr. Approximately 1,000X.

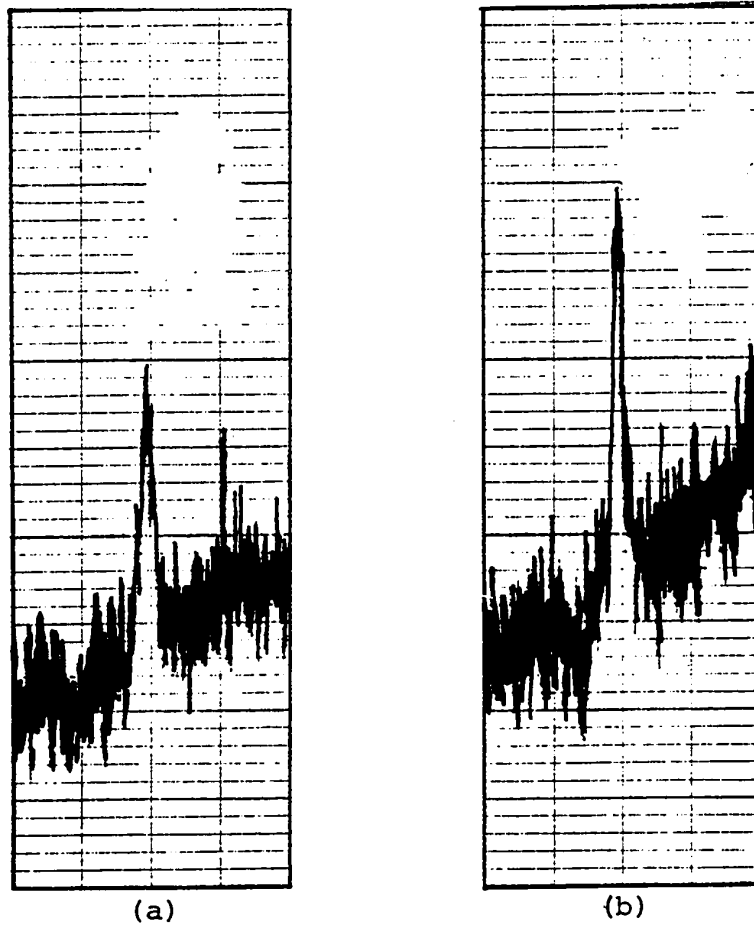


FIGURE 35. (111) diffraction peak of titanium carbide.  
(a) as deposited 0.018 a/o titanium alloy.  
(b) heat treated 0.013 a/o titanium alloy.

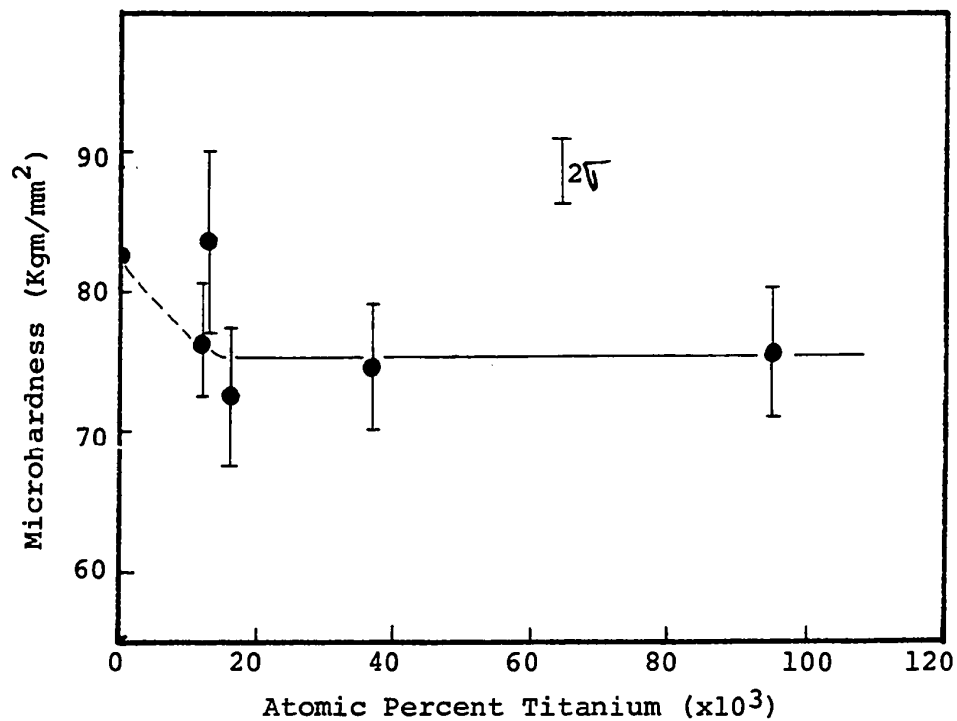


FIGURE 36. Microhardness on planes perpendicular to basal planes for alloys formed at  $1675 \pm 75^\circ\text{C}$  and heat treated at  $1600 \pm 100^\circ\text{C}$  for 20 hours.

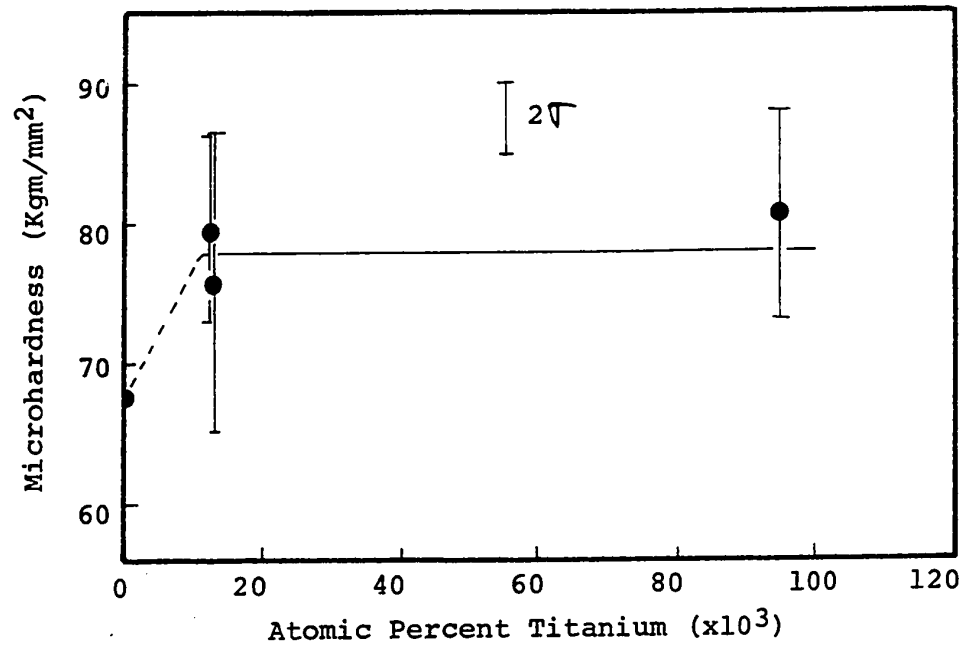


FIGURE 37. Microhardness on basal planes for alloys formed at  $1675 \pm 75^\circ\text{C}$  and heat treated at  $1600 \pm 100^\circ\text{C}$ .



FIGURE 38. Electron microprobe scan of titanium distribution. 0.037 a/o titanium alloy formed at  $1675 \pm 75^\circ\text{C}$  and heat treated at  $1600 \pm 100^\circ\text{C}$  for 20 hours. Scan is of planes perpendicular to basal planes. Approximately 150X.

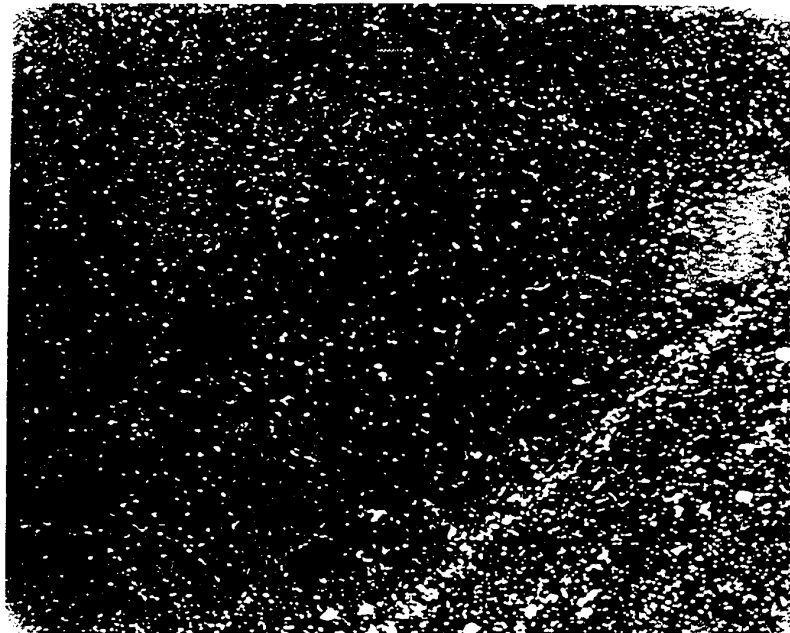


FIGURE 32. Electron microprobe scan of titanium distribution. 0.037 wt% titanium alloy formed at  $1675 \pm 75^\circ\text{C}$  and heat treated at  $1600 \pm 100^\circ\text{C}$  for 20 hours. Scan is of planes perpendicular to basal planes. Approximately  $15\times$ .





FIGURE 39. Electron microprobe scan of titanium distribution. Alloy contains 0.013 a/o titanium and was formed at  $1675 \pm 75^\circ\text{C}$  and subsequently heat treated for 20 hours at  $1600 \pm 100^\circ\text{C}$ . Scan is of basal planes. Approximately 150X.

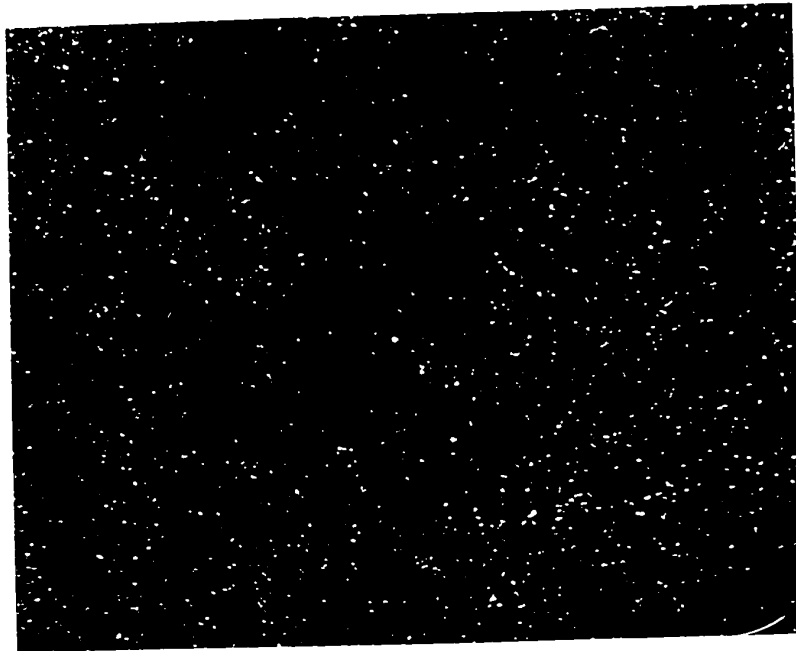


FIGURE 39. Electron microprobe scan of titanium distribution. Alloy contains 0.013 a/o titanium and was formed at 1675 ± 75°C and subsequently heat treated for 20 hours at 1600 ± 100°C. Scan is of basal planes. Approximately 150X.

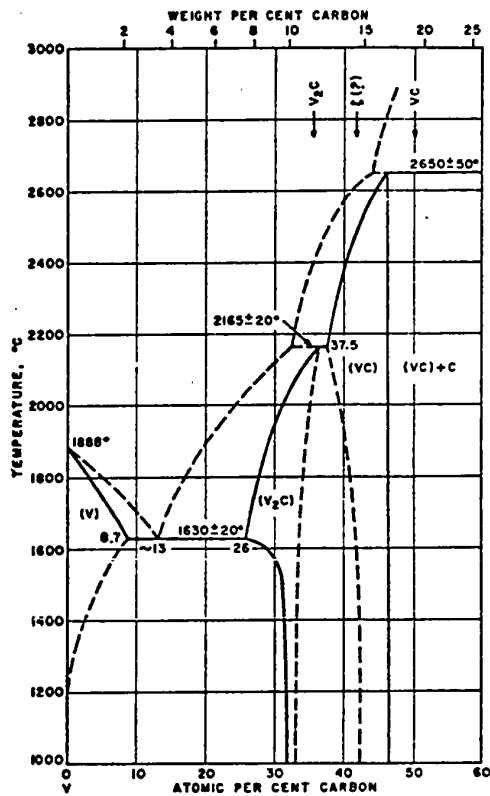


FIGURE 40. Carbon-vanadium phase diagram.

Taken from F. A. Shunk, Constitution of Binary Alloys, Second Supplement, McGraw Hill Co., New York, 1969.



FIGURE 41. Singularly nucleated pyrolytic graphite- $<0.001$  a/o vanadium alloy formed at  $1800 \pm 20^\circ\text{C}$  and 5 torr. 80X, polarized light.

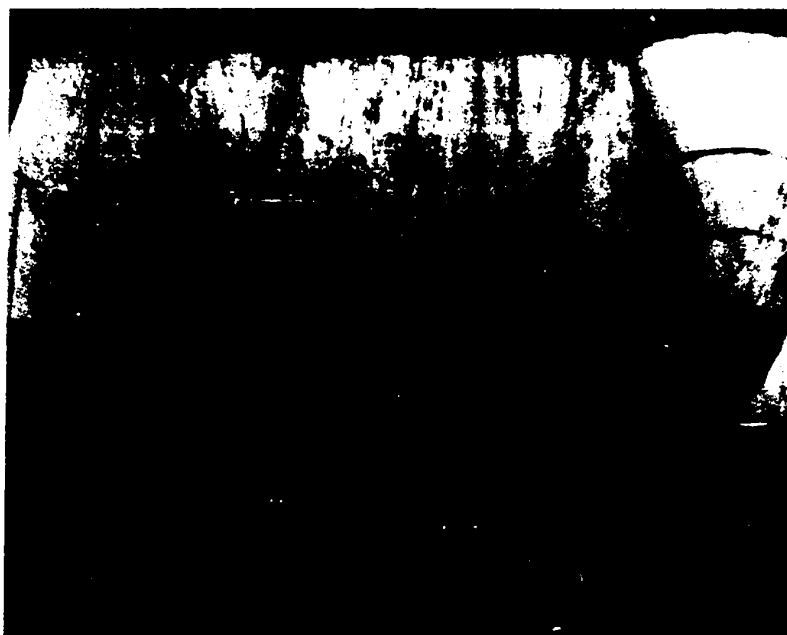


FIGURE 41. Singularly nucleated pyrolytic graphite-<0.001 a/o vanadium alloy formed at  $1800 \pm 20^{\circ}\text{C}$  and 5 torr. 80X, polarized light.

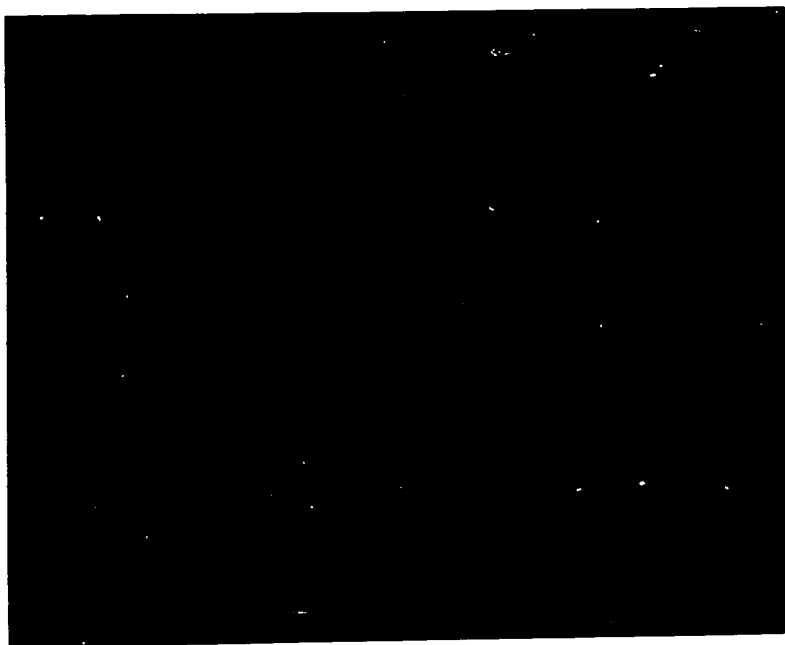


FIGURE 42. Non basal planes of a pyrolytic graphite- $<0.001$  a/o vanadium alloy formed at  $1700 \pm 30^\circ\text{C}$  and 8+ torr. 80X, polarized light.

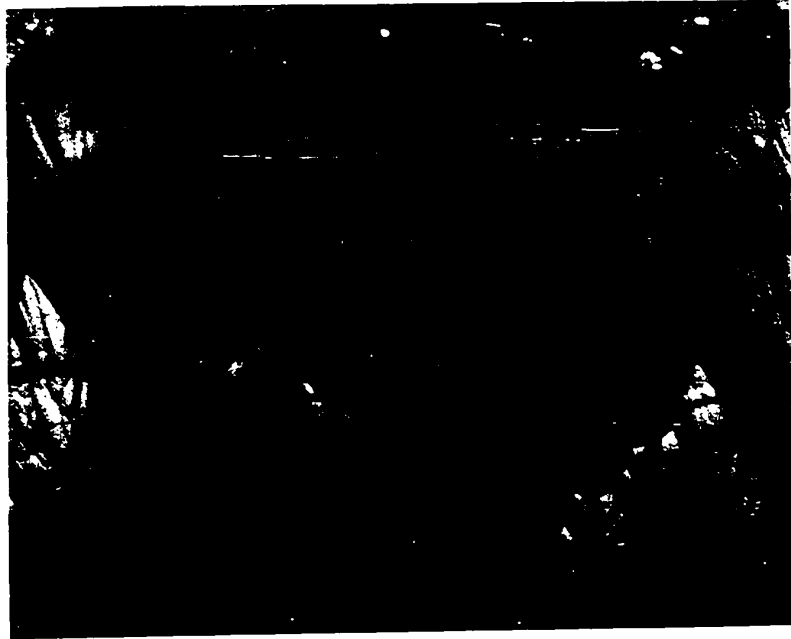


FIGURE 42. Non basal planes of a pyrolytic graphite- $<0.001$  a/o vanadium alloy formed at  $1700 \pm 30^\circ\text{C}$  and  $8+$  torr. 80X, polarized light.



FIGURE 43. Carbon plume growths on substrate formed at  $1700 \pm 30^\circ\text{C}$  and 8+ torr.



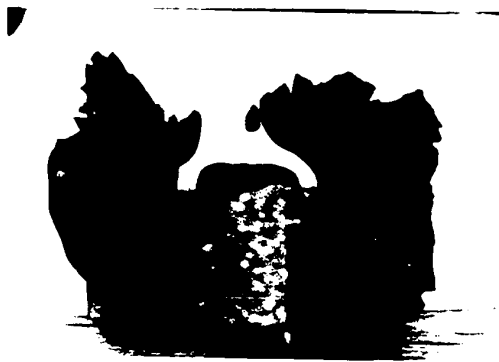


FIGURE 43. Carbon plume growths on substrate formed at  $1700 \pm 30^\circ\text{C}$  and 8+ torr.

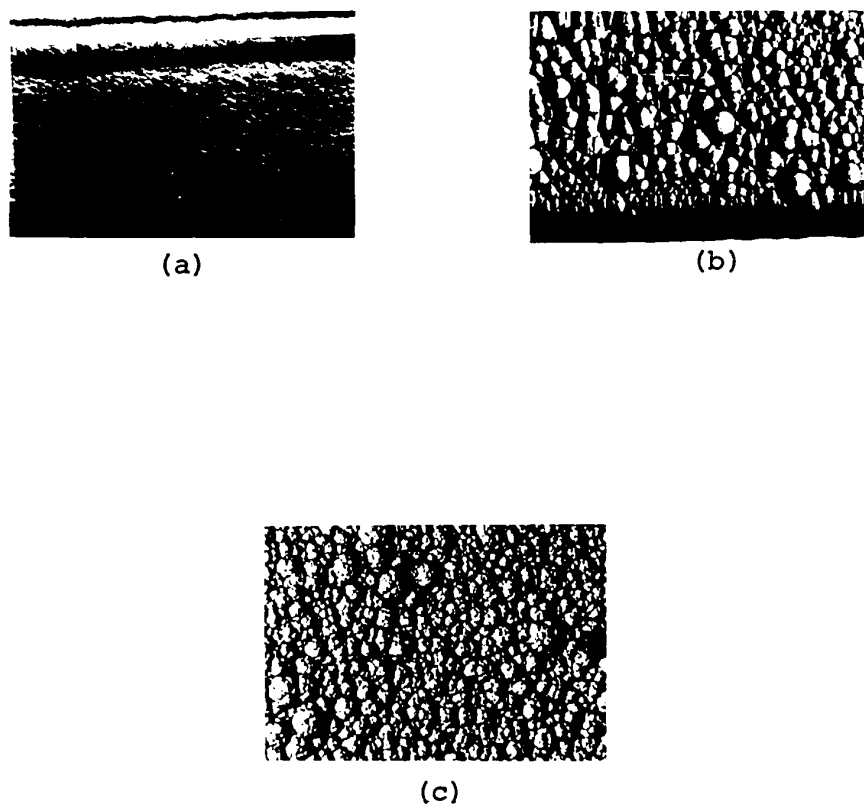


FIGURE 44. Top view of basal planes of graphite-vanadium alloys. 6X

- (a) Typical basal plane of pure pyrolytic graphite.
- (b) Basal plane of alloy formed at  $1790 \pm 50^\circ\text{C}$  and 5 torr.
- (c) Basal plane of alloy formed at  $1550 \pm 100^\circ\text{C}$  and 14 torr.

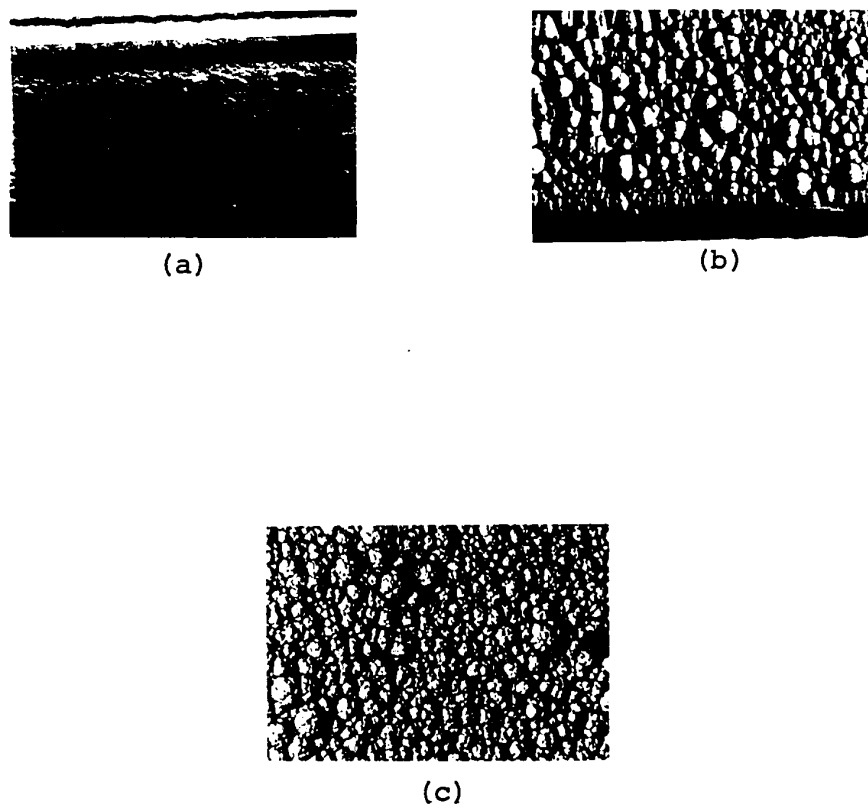


FIGURE 44. Top view of basal planes of graphite-vanadium alloys. 6X

- (a) Typical basal plane of pure pyrolytic graphite.
- (b) Basal plane of alloy formed at  $1790 \pm 50^\circ\text{C}$  and 5 torr.
- (c) Basal plane of alloy formed at  $1550 \pm 100^\circ\text{C}$  and 14 torr.

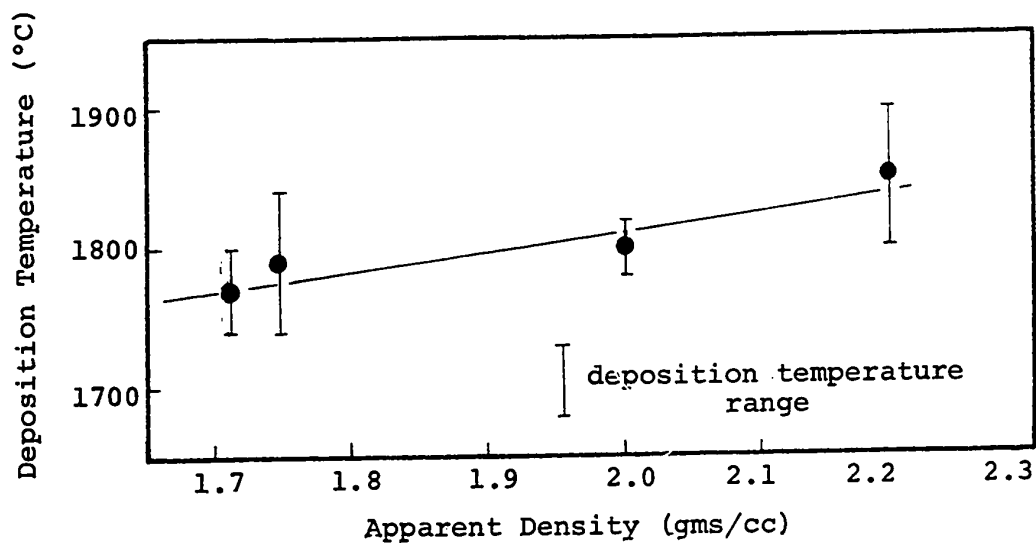


FIGURE 45. Apparent density as a function of deposition temperature for pyrolytic graphite alloys containing <0.001 a/o vanadium and formed at 5 torr.



FIGURE 46. Singularly nucleated pyrolytic graphite-0.003 a/o nickel alloy formed at  $1620 \pm 20^\circ\text{C}$  and 6.5 torr. 80X, polarized light.



FIGURE 46. Singularly nucleated pyrolytic graphite-0.003 a/o nickel alloy formed at  $1620 \pm 20^\circ\text{C}$  and 6.5 torr. 80X, polarized light.



FIGURE 47. Electron microprobe scan of nickel in a pyrolytic graphite alloy containing 0.003 a/o nickel.

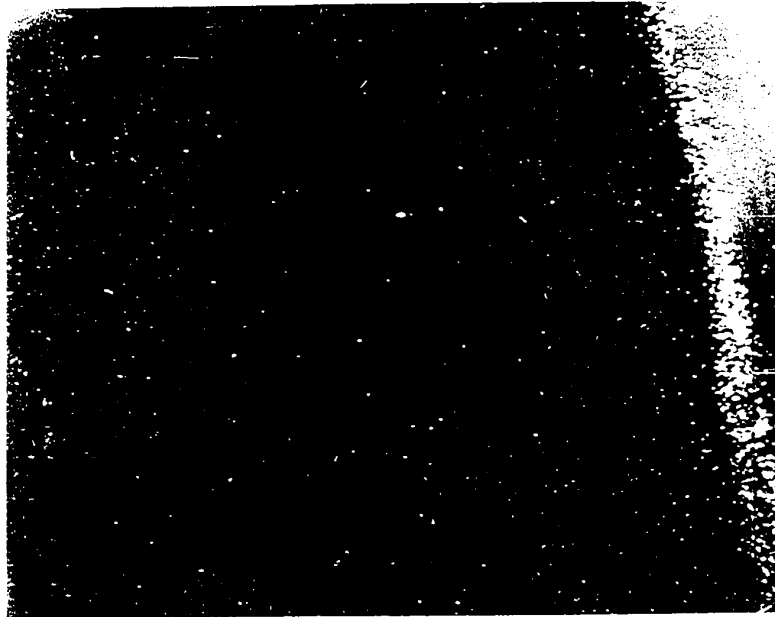
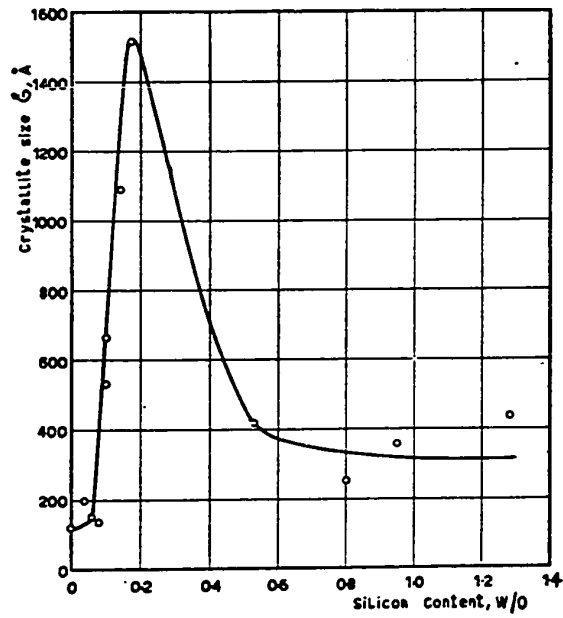
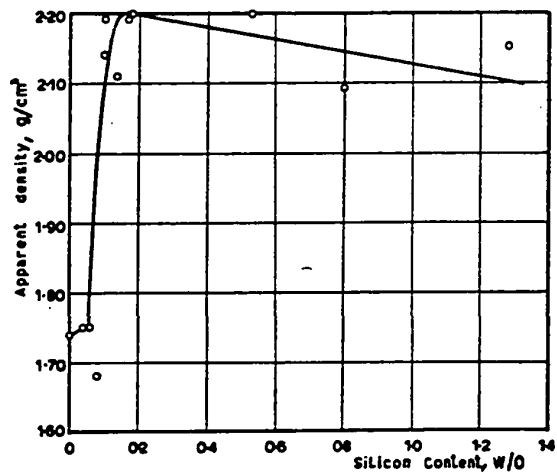


FIGURE 47. Electron microprobe scan of nickel in a pyrolytic graphite alloy containing 0.003 a/o nickel.





Dependence of the crystallite height on silicon content.



Density of silicon-containing pyrocarbon against silicon content.

FIGURE 48. Results taken from Marinkovic et al, Carbon 8, 1970, p. 283. Peak values are interpreted as the limit of solid solubility.

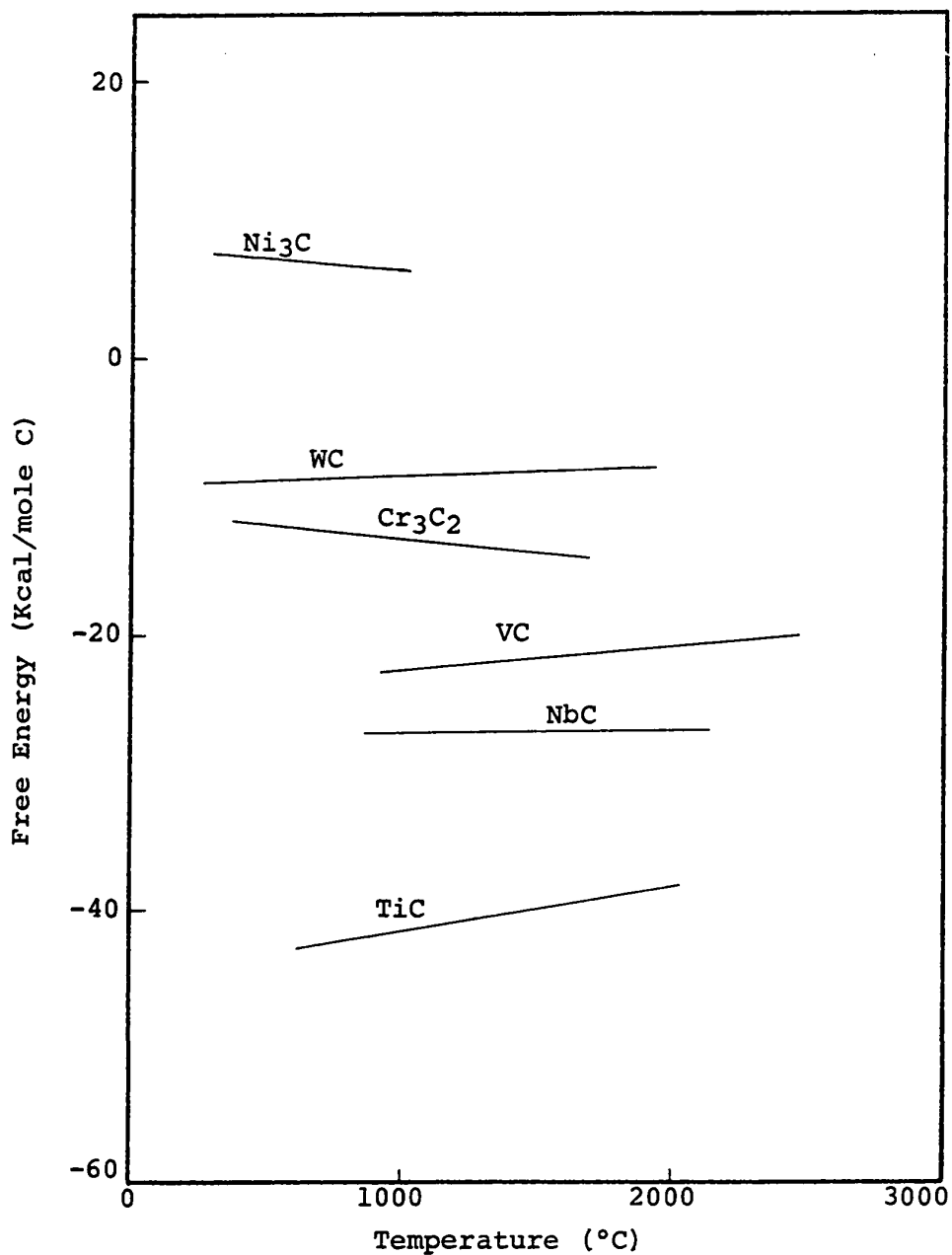


FIGURE 49. The standard free energies of formation of carbides per mole of graphite. Data taken from O. Kubaschewski, E. L. Evans and C. B. Alcock, Metallurgical Thermochemistry, Pergamon Press, 1967.

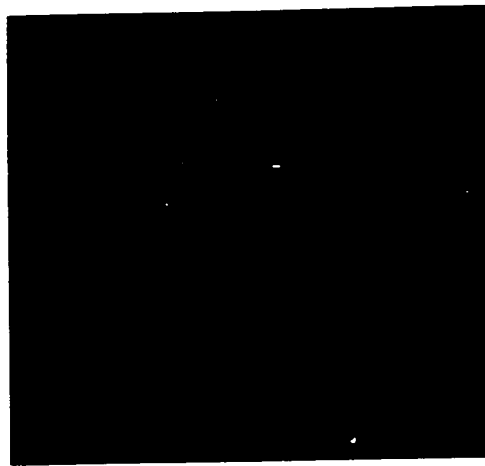


FIGURE 50. Precipitate in pyrolytic graphite-titanium alloy with [110] zone planes perpendicular to graphite basal planes.

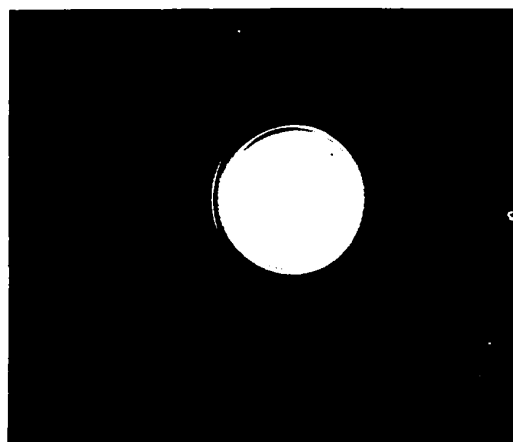
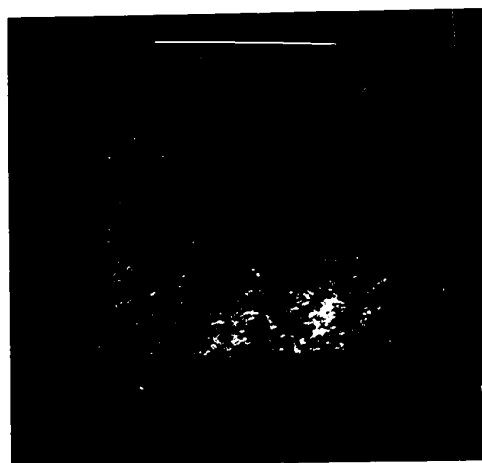


FIGURE 50. Precipitate in pyrolytic graphite-titanium alloy with  $[110]$  zone planes perpendicular to graphite basal planes.

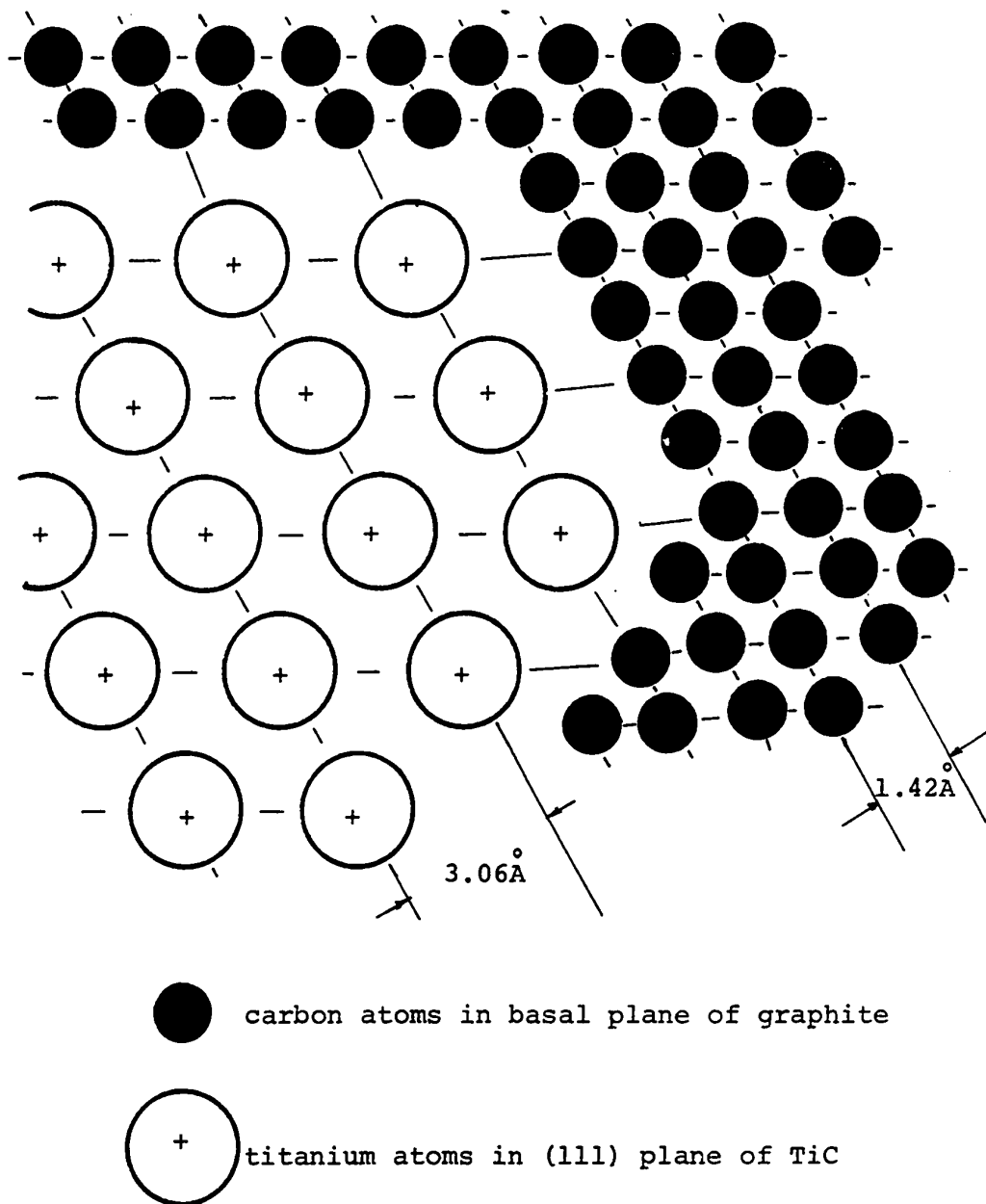


FIGURE 51. Semi-coherent interface between titanium carbide and graphite.

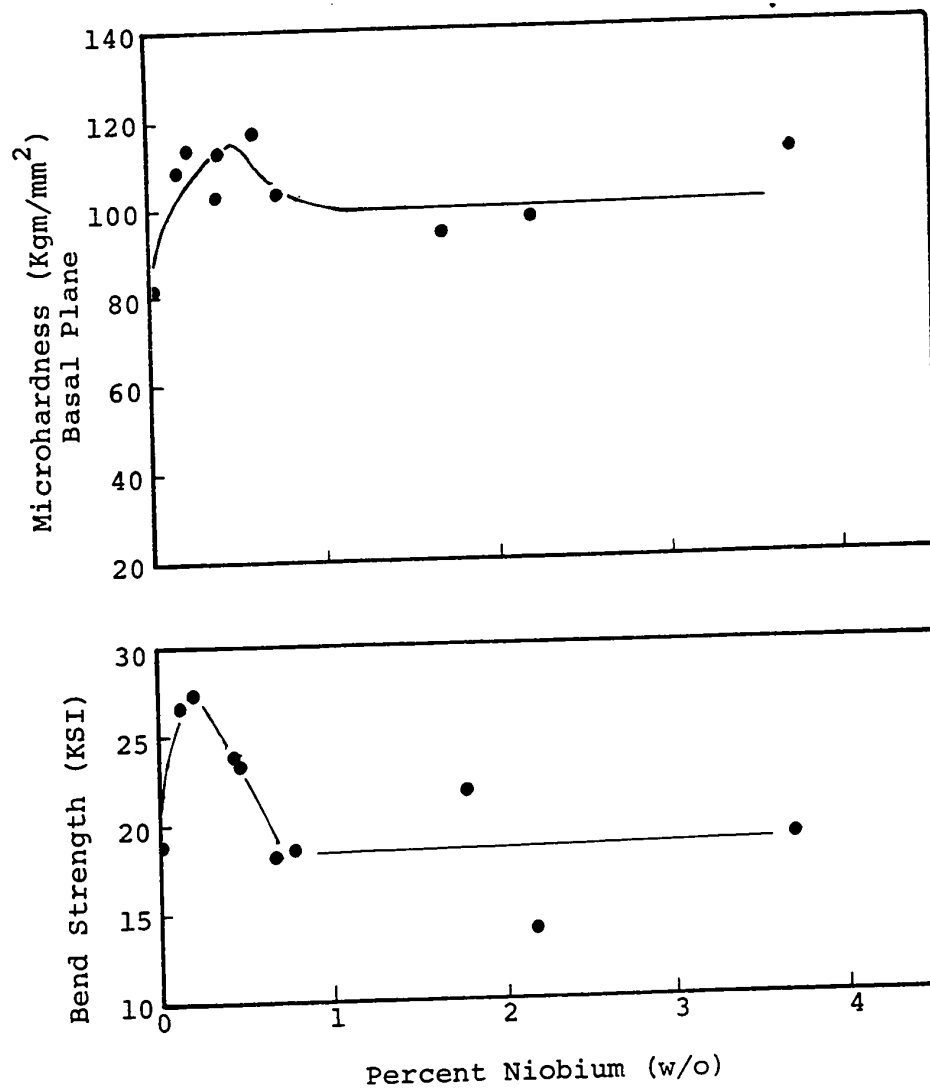


FIGURE 52. Properties of pyrolytic carbon-niobium alloys. Data taken from U.S. Patent 3,464,843.

APPENDIX AExperimental Error Analysis1. Deposition Temperature

Deposition temperature was monitored by a Latronics Infrared pyrometer and a chromel-alumel thermocouple. The pyrometer is sensitive to radiation between 1.8 and 2.7 microns and thus atmosphere, water vapor, and quartz glass absorption bands are avoided. The emissivity of the substrate and deposit was found to be very dependent on temperature and an emissivity calibration of the pyrometer had to be carried out.

The pyrometer calibration was done by first depositing pyrolytic graphite on a substrate. With the emissivity of the pyrometer set at 0.5, the substrate was heated to a desired temperature and allowed to equilibrate. The emissivity was then varied and the corresponding temperature noted. Another temperature at emissivity 0.5 was then selected and the process repeated until the series of curves given in Figure A1 was obtained. Next, metallic materials were suspended one at a time over the substrate and their melting point determined with the pyrometer emissivity set at 0.4. The metals used were:

nickel	mp - 1453°C
zircalloy #2	mp - 1800-1830°C
niobium	mp - 2468°C

Figure A2 represents the curve obtained for melting temperature versus observed pyrometer temperature. Now, taking the observed temperature from Figure A2 and locating that temperature on Figure A1 at an emissivity of 0.4, a curve could be drawn parallel to existing curves, the actual temperature was found on this curve, and thus the emissivity setting required to give the actual temperature could be determined. It is estimated that with care, temperature inaccuracies would be no more than 2 or 3 percent. Pyrometer accuracy is given as  $\pm 1\%$ .

Difficulties, however, occurred with excessive sooting in the deposition chamber. Some soot settled out on the quartz sight glass and prevented use of the pyrometer. This occurred even though the glass was protected by a shutter. A sheathed thermocouple in the vicinity of the deposition substrate could then be employed to monitor deposition temperature. Quite often, the fogging over of the sight glass occurred late in the deposition run. It was then possible to monitor temperature by keeping the rate of change of temperature, as indicated by the thermocouple, constant with what it had been previously. In instances where the sight glass became useless almost immediately, previous experience



was used to keep the temperature indicated by the thermocouple in line with the deposition rate. Such instances probably resulted in a temperature error of  $\pm 10\%$ .

Rough controls on the power source resulted in temperature fluctuations. Reported temperatures are thus given over a range, and any errors due to the pyrometer being out of calibration are thereby less important.

## 2. Chemical Analysis

With care, errors in spectroscopy determinations should be low, especially where there are no interfering ions or compounds. However, to check on the reliability of the chemical analysis of graphite-metal alloys, several alloys were analyzed by a commercial firm.\* A comparison of the results is given in Table A1 and it can be seen that with the exception of vanadium all the results between the two analyses are approximately the same and even vanadium results differ only at low concentrations where inhomogeneity in the alloy deposit could be more of a factor than the actual analysis.

---

\* Commercial analysis done by Chicago Spectro Service Laboratory, Inc., Chicago, Illinois.

### 3. Density Measurements

Densities were determined to five place figures with four place figure significance. Density checks were performed on several alloy deposits and agreement within  $\pm 0.003$  gm/cc was found for samples selected from the same region of the deposit. Density of the deposit was found to vary from top to bottom in the deposit--the bottom of the deposit being most dense. For this reason, only an apparent density could be cited.

### 4. X-ray Measurements

X-ray diffractometer measurements were recorded to the nearest thousandth of a degree but calculations were done only on two decimal place accuracy. The root mean square lattice strain values are somewhat questionable for this reason. Lattice c parameter determination was done by averaging results from four sets of fore and back scans. Weighted peak radiation length was used in the calculations.

### 5. Microhardness Measurements

Reported experimental microhardness values were obtained by taking eight or more values from a single sample and subjecting the results to statistical analysis. A large number of results were rejected in this manner and it was thought

that perhaps microhardness might vary with load in the 100 gm load range. Figure A3 shows that above a load of 40 grams, microhardness values are constant with increasing load. Variations in microhardness values must therefore be related to local microstructural differences in the deposits. Figure A3 shows this could be the case as all reported values, except the 100 gm load value, are from single hardness readings.

TABLE A1Comparison of Chemical Analyses

	w/o Alloy Element	
<u>Sample Number</u>	<u>Analysis by Author</u>	<u>Commercial Analysis</u>
37PCTi	0.050	0.0520
2PCV	0.008	<0.005
2PCNi	0.014	0.0150

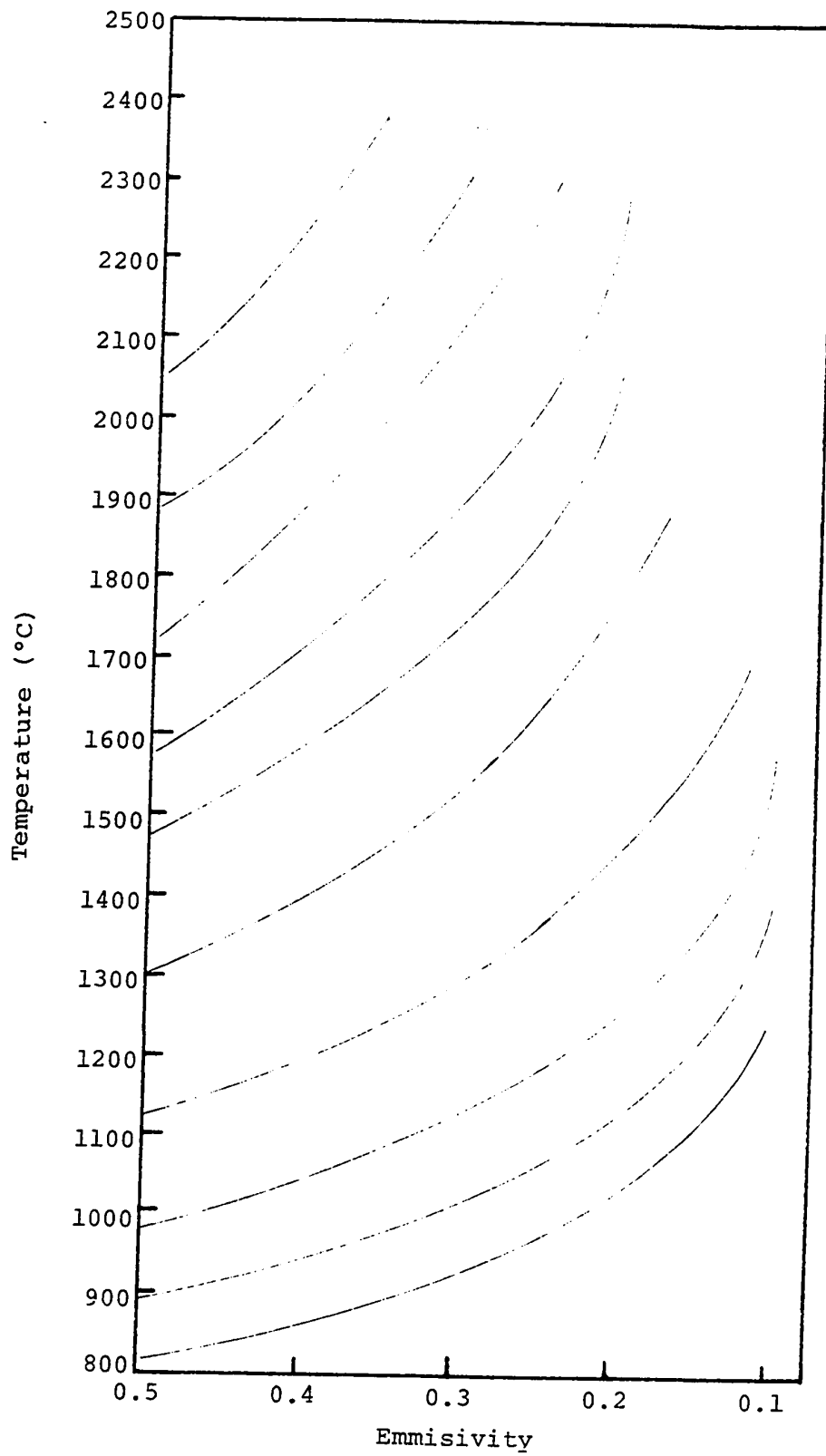


FIGURE A1. Pyrometer temperature reading as a function of emmissivity setting.

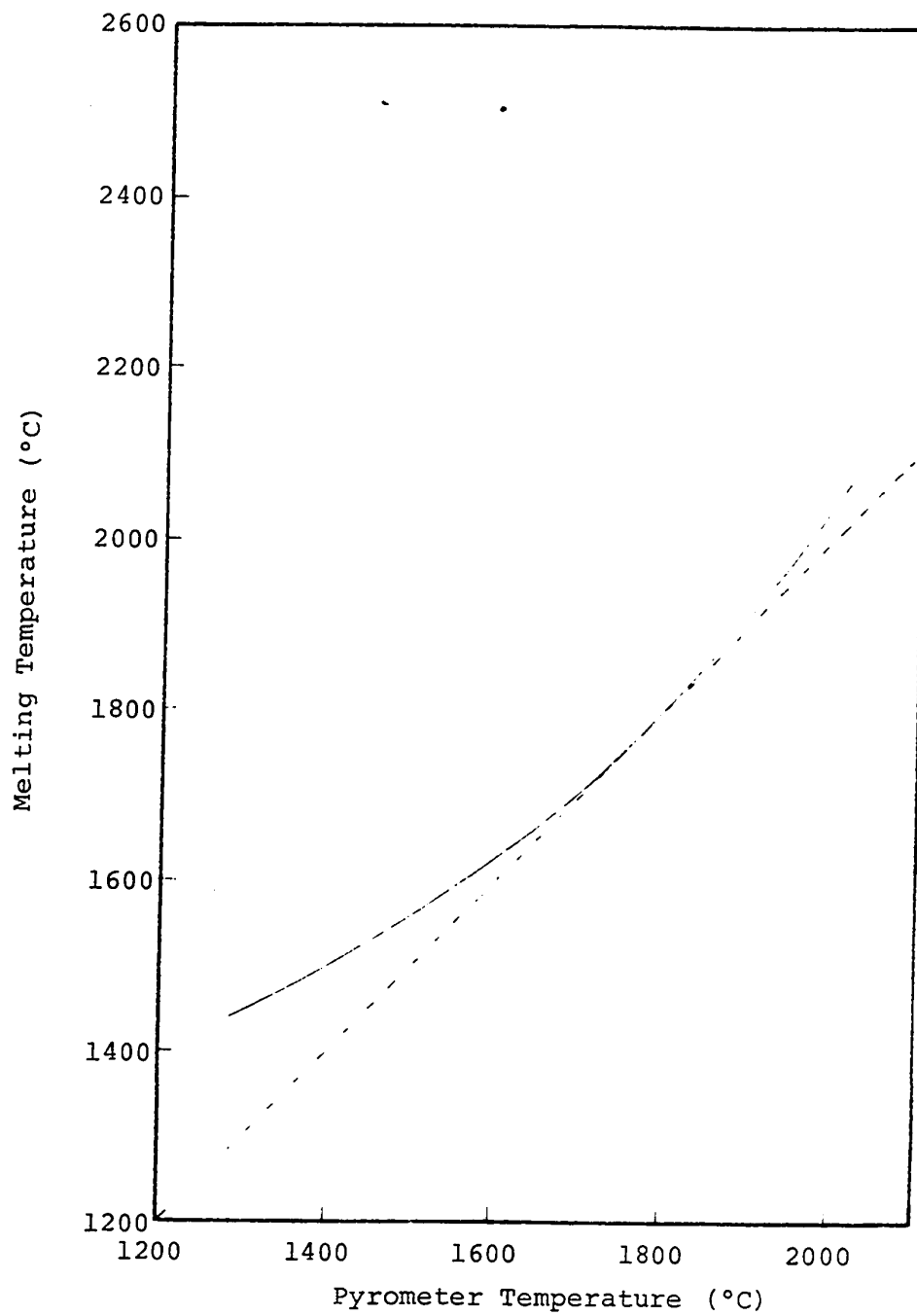


FIGURE A2. True temperature as a function of observed pyrometer temperature for an emissivity setting of 0.4.

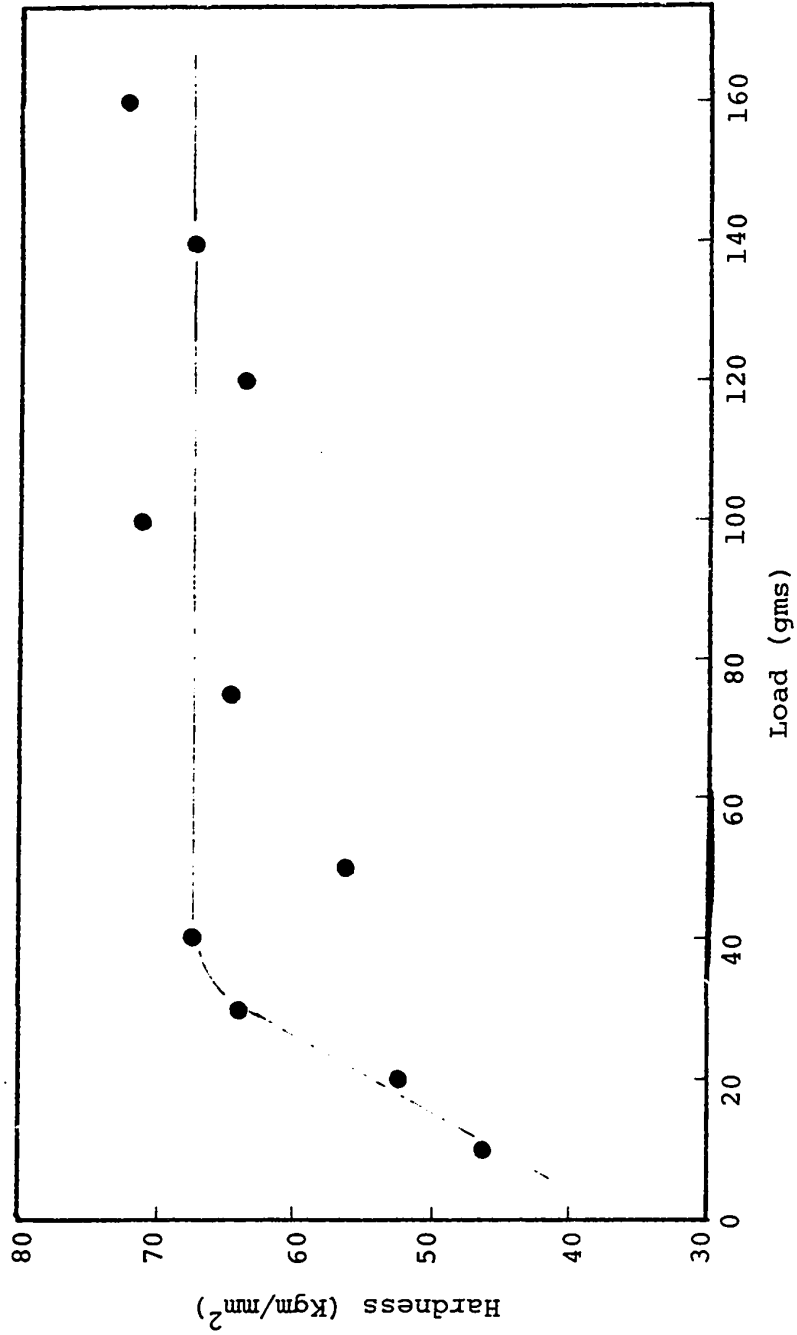


FIGURE A3. Microhardness on planes perpendicular to basal planes as a function of applied load for sample #8PC.

APPENDIX BEvaluation of Reported Solubilities

The solubility limit of 0.3 a/o nickel in graphite reported in the literature<sup>1</sup> was determined by examining graphite grown in a liquid nickel bath. The graphite was subsequently analyzed in situ by an electron probe. Extraction of graphite crystals from the nickel matrix followed by conventional chemical analysis on the graphite was not found to be practical or reliable. The graphite crystals were, however, examined by electron microscopy and found to be uniform to a resolution of 100 Å. It is unfortunate that no X-ray structure determination was done on the graphite to determine its degree of graphitization. In a study<sup>2</sup> of graphite grown in an iron-silicon melt, it was found that the graphite had a lattice parameter,  $c$ , smaller than that of ideal graphite. This graphite contained both iron and silicon but, after etching, only silicon remained. Also, after etching, the graphite gave an ideal lattice spacing of 3.3538 Å. This led to the conclusion that iron creates an internal pressure of approximately 100 Kg/cm<sup>2</sup> to give a lower  $c$  value. Such may also be the case with graphite grown in nickel melts so that standard conditions do not exist for any reported solubility. The determination in



situ using an electron microprobe can also give an erroneously high nickel concentration as the probe excites fluorescence from a volume rather than a surface.

The solubility of vanadium in well crystallized graphite has been reported as 0.088 a/o vanadium.<sup>3</sup> This was obtained by examining, with an electron microprobe, a glassy carbon on which vanadium carbide had been melted. The vanadium rapidly diffused into the carbon. As vanadium is known to catalyze graphitization, a measurement of vanadium concentration in an area of the carbon which had been graphitized by molten vanadium carbide was taken as the solubility limit. These findings on solubility are not really convincing as the authors produce a fluorescent X-ray image of the area in which solubility was determined. This photo shows clustering of vanadium. A photomicrograph of the area shows a mixture of vanadium carbide and graphite. Furthermore, this work was done on glassy carbon which is not graphite. Experiments with pyrolytic graphite showed very little penetration of the graphite by vanadium or vanadium carbide and experiments with natural graphite showed no reaction at all. It would appear then that the reported solubility is too high and may not be generalized to other conditions. The authors also state, "the solubility of vanadium in disordered carbon ought to be smaller [than in crystalline graphite] but there seems to be no experimental way of

-confirming this." This statement appears to be in direct opposition to their experimental findings and also to the findings of other investigators.<sup>4,5</sup>

Thus it appears that the two reportings of solid solubility for transition metals in graphite are perhaps orders of magnitude too large.

References

1. H. M. Strong and R. E. Hanneman, "Crystallization of Diamond and Graphite", J. Chem. Phys. 46, 1967, p. 3668.
2. P. L. Walker and G. Imperial, "Structure of Graphite", Nature 180, 1957, p. 1184.
3. E. Fitzer and B. Kegel, "Reaktionen Von Kohlenstoff-gesattigter Vanadiumcarbidschmelze mit Ungeordnetem Kohlenstoff", Carbon 6, 1968, p. 433.
4. R. L. Courtney and S. F. Duliere, "The Catalytic Graphitization of Naphthalenediol and a Urethane Foam--A Feasibility Study", Carbon 10, 1972, p. 65.
5. S. D. Robertson, "Carbon Formation from Methane Pyrolysis Over Some Transition Metal Surfaces", Carbon 8, 1970, p. 365.

**END OF  
REEL**